Imperial College London

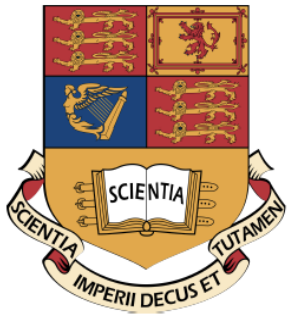

p-type metal oxides as interfacial layers in organic photovoltaics

Ahmed Ismail

A thesis submitted in fulfilment of the degree of

Doctor of Philosophy

Department of Materials

Imperial College London

March, 2020

Declaration of Originality and Copyright

This thesis describes the work carried out during the period of October 2015 to October 2019 within the Department of Materials, Imperial College London. The material presented herein is the product of my own work, except where explicit references have been made, and has not been previously submitted in whole or in part for an award of a degree at this or any other institutions.

Research Supervisors:

Dr Martyn A. McLachlan from the Department of Materials, Imperial College London, UK.

Professor Thomas D. Anthopoulos from Department of Physics, Imperial College London, UK and Division of Physical Sciences and Engineering, King Abdullah University of Science and Technology, Saudi Arabia.

External examiner: Professor Demosthenes Koutsogeorgis from the Department of Physics & Mathematics, School of Science and Technology, Nottingham Trent University, UK.

Internal examiner: Professor Martin Heeney from the Department of Chemistry, Imperial College London, UK.

Ahmed Ismail

March 2020

Acknowledgement

First and foremost, I would like to express my deepest gratitude towards my brilliant supervisor, Dr Martyn McLachlan, for his excellent guidance, continuous support, and resourceful inspiration throughout my PhD journey. He helped me with each task in this journey to move forward. He kept me on track and his advice helped me achieve my goals. A 'thank you' is simply not enough for him. I am also grateful to my second supervisor, Prof. Thomas Anthopoulos, for his insightful suggestions, useful advices, and giving me this precious opportunity to come to this wonderful place.

Next, I would like to thank all the past and present members of the McLachlan's group for all the good times we have shared in and out of the labs. Discussion with them and the advice they provided were always very useful. I will be eternally grateful to Dr Hendrik Faber for training, useful advice and offering his help on everything in my initial stage. I would like to give thanks to Dr Flurin Eisner, Dr Maurizio Morbidoni and Dr Anna Regoutz for their help with device fabrication and XPS measurements. Furthermore, I would like to express my gratitude to Dr Shengda Xu (Bob) for his help on XPS analysis, as well as his help and support in the last stage of my work.

I deeply acknowledge the Egyptian government and the department of Materials, Imperial College London for the financial support, without which I would not have been here at all.

I thank my parents, and siblings, for their warm-hearted support and unconditional love, without which I would not be where I am. They are always believing in me and for being there for me whenever I needed them. They have done so much to help me and my small family throughout our journey.

Finally, a special thanks go to my lovely wife, Mai, and my lovely kids, Asser, Aseel, and Aysel. The life in London and my PhD study, would not be possible without the endless support and their unconditional love. They are simply the best thing that ever happened to me. The past four years might well be the darkest moment to our family, but it has been the most fruitful learning experience to us.

Abstract

Organic photovoltaics (OPVs) have attracted a considerable research interest over the past few decades as a low-cost and nontoxic source of renewable energy. Although a power conversion efficiency (PCE) of up to 17.4% has been achieved for single junction, this is still lower than that of inorganic solar cell, so more work is needed to realize the full commercial potential of OPVs. One way to improve the performance and stability of OPVs is the inclusion of interfacial layers, which facilitate the transport of both electrons and holes to both electrodes. Zinc oxide is widely used electron transport layer (ETL) that has the advantage of good electrical properties and chemical stability. The most commonly used hole transporting material (HTL) is PEDOT:PSS, which has better electrical properties than the most of the alternatives, but its acidic and hydroscopic nature limits the durability of the OPV, so a replacement is needed.

This thesis focuses on the development of high-performance OPVs based on p-type metal oxides as potential alternatives to PEDOT:PSS. Firstly, in chapter 3, we have successfully demonstrated the thermal evaporation of controlled thickness, high optical quality NiOx thin films. It was anticipated that the films would be hole selective transport layers, however those prepared were surprisingly shown electron transport behaviour. This was attributed to the alloying between the Ni and tungsten boat during evaporation. After identifying the optimum thickness and tungsten content in evaporated films, we have demonstrated those films as efficient universal electron transport layers in a wide variety of organic photovoltaic devices. Next, chapter 4 presents the fabrication of CuO_x films by solution process and their potential as HTLs in OPVs comparing with commonly used HTL, PEDOT:PSS. The characterisation of the CuO_x films allowed a fully understanding of the structure and optoelectronic properties to identify an optimum annealing temperature and film's thickness. The impact of processing solvent on device performance is further studied. Finally, chapter 5 demonstrates the preparation of CuO_x via novel synthetic route at low temperature. The influence of annealing temperature on device performance compared to PEDOT:PSS is further investigated. This work shows the potential of CuO_x as efficient HTLs for OPV.

List of Abbreviations

AFM	Atomic force microscopy
APS	Air Photoemission Spectroscopy
BHJ	Bulk heterojunction
C8-ITIC	{(2Z)-2-[(8-{(E)-[1-(Dicyanomethylidene)-3-oxo-1,3-dihydro-2H-inden-2-ylidene]methyl}-6,6,12,12-tetraoctyl-6,12-dihydrothieno[3,2-b]thieno[2″,3″:4′,5′]thieno[2′,3′:5,6]-s-indaceno[2,1-d]thiophen-2-yl)methylidene]-3-oxo-2,3-dihydro-1H-inden-1-ylidene}propanedinitrile
E_F	Fermi level Energy
E_g	bandgap Energy
ETL	Electron transport layer
FF	Fill Factor
HOMO	Highest occupied molecular orbital
HTL	Hole transport layer
ICBA	Indene-C60-bisadduct
ITIC	3,9-bis(2-methylene-(3-(1,1-dicyanomethylene)-indanone))-5,5,11,11 tetrakis(4-hexylphenyl)-dithieno[2,3-d:2’,3’-d’]-s-indaceno[1,2-b:5,6-b’] dithiophene
ITO	Indium tin oxide
IPA	Isopropanol
J_{SC}	Short circuit current density
KP	Kelvin Probe
LUMO	Lowest unoccupied molecular orbital
MEA	monoethanolamine
P3HT	Poly(3-hexylthiophene-2,5-diyl)
PBDB-T	Poly[(2,6-(4,8-bis(5-(2-ethylhexyl)thiophen-2-yl)-benzo[1,2-b:4,5-b’] dithio-phene))-alt-(5,5-(1’,3’-di-2-thienyl-5’,7’-bis(2-ethylhexyl)benzo [1’,2’-c:4’,5’-c’]dithiophene-4,8-dione)]
PCE	Power conversion efficiency
$PC_{71}BM$	[6,6]-Phenyl-C71-butyric acid methyl ester

PEDOT:PSS	Poly(3,4-ethylenedioxythiophene) polystyrene sulfonate
PFBDB-T	Poly{4,8-bis[5-(2-ethylhexyl)thiophen-2-yl]benzo[1,2-b:4,5-b'] bisthiophene-alt-1,3-bis(2-ethylhexyl)-5-(4-fluorothiophen-2-yl)-7-{5-[tri(propan-2-yl)silyl]thiophen-2-yl}-4H,8Hbenzo[1,2-c:4,5c']bisthiophene-4,8-dione }
PTB7	Poly[[4,8-bis[(2-ethylhexyl)oxy]benzo[1,2-b:4,5-b']dithiophene-2,6-diyl][3-fluoro-2-[(2-ethylhexyl)carbonyl]thieno[3,4-b]thiophenediyl]]
RMS	Root mean square
R_s	Series resistance
R_{sh}	Shunt resistance
TMO	Transition metal oxide Transient
VBM	Valence band maximum
V_{OC}	Open circuit voltage
XPS	X-ray photoelectron spectroscopy
XRD	X-ray diffraction

Contents

List of figures

List of Tables

1 Introduction and literature review

1.1 Introduction

1.1.1 Background

The global demand for low carbon cost-effective renewable energies as an alternative to fossil fuels is escalating. With greenhouse effects causing global warming, cleaner energy sources such as wind, tide, and solar are required. According to the international Energy Agency (IEA), the sun could be the largest source of such energy by 2060 [1].

The sun emits energy at a rate of 3.8×10^{26} W, while only 1.08×10^{17} W reaches the surface of the Earth [2]. Nevertheless, the solar energy received in 90 min is more than the world's total annual energy consumption in 2018 ($\approx 5.86 \times 10^{20}$ Joules) [3]. Although the annual global installations of PVs reached 178 GW in 2014, the contribution of PVs to electricity supply still remains less than 0.1%. The IEA predicts growth in global PVs capacity to 7200 TWh by 2040 [1]. Therefore, extensive efforts have been focused on developing photovoltaic (PVs) technologies [4].

The photovoltaic effect, the operating principle of a solar cell, was discovered by Becquerel in 1839 [5], who observed the photocurrents produced on illuminating platinum electrodes coated with silver chloride immersed in aqueous solution. In 1905, Albert Einstein described light as composed of discrete quanta, called photons, rather than continuous waves. This was a key step in the discovery of the law of the photoelectric effect [6]. In 1954 Chapin et al. introduced the first PV at Bell Laboratories [7], based on a single-crystal silicon p–n junction, with a power conversion efficiency of 6% and has since been used in many applications.

Primarily, PVs were employed as a sustainable power source for communication satellites, while the past decade has seen a significant progress in deployment of photovoltaics technologies. They find many applications in the consumer market because the increasing efficiencies (17.4% for single junction and 14.2% for tandem solar cells) [8], and the sharp reduction in manufacturing costs [9].

1.1.2 Generations of Photovoltaics

In order to deliver a low-cost, high efficiency, and long lifetime Photovoltaics, many research on new materials and device structure has drawn a great interest to achieve these goals [9]. Photovoltaics are classified into three generations according to their development stages, as shown in **Figure 1.1**.

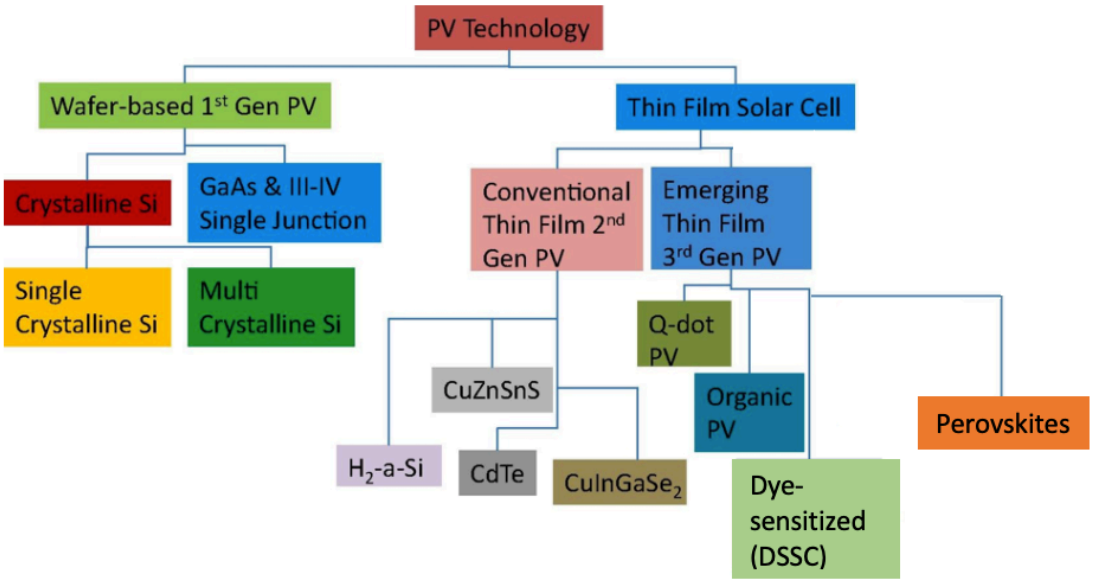

Figure 1.1 Schematic diagram describes the generations of photovoltaics, adapted from [10].

First-generation PVs are mainly based on crystalline silicon; are still in use and the current market leader where polycrystalline and monocrystalline Si represent 65% and 35% respectively [11]. These PVs yield efficiencies over 26.7% and lifetime ~ 25 years [7], which is close to the theoretical Shockley-Queisser limit of 33% [12]. The relatively low absorption coefficient of monocrystalline Si which originates from its indirect bandgap (1.12 eV) requires thick layers of 100 – 200 µm to absorb sufficient light. The high carrier mobility of monocrystalline Si (electron and hole mobilities are 1200 and 400 $cm^2V^{-1}S^{-1}$ respectively) overcomes this thickness requirement and prevents the bulk recombination [13]. Polycrystalline Si has also been employed in solar cells due to its low processing costs. However, its efficiency is lower than that of monocrystalline Si because of the grain boundaries which increase the charge recombination. The high optical absorption of amorphous Si (E_g ~ 1.70 – 1.80 eV), makes it an interesting material for PVs applications but its morphology and poor charge carrier mobility limit the efficiency to ~ 10.5% [8].

Despite of the high PCE and long lifetime of crystalline silicon PVs, the high manufacturing cost makes them unable to compete with the inexpensive fossil fuel-based electricity, leading to an interest in low cost PV alternatives [7].

Second-generation cells are based on thin-film inorganic semiconductor materials such as cadmium sulfide (CdS), cadmium telluride (CdTe), and copper indium gallium selenide (CIGS). These PVs are lower in cost than crystalline Si PVs and have been rapidly growing in the past decade [14]. In addition, their efficiency level has caught up with first generation PVs with CdTe and CIGS solar cells now exceeding 23% efficiency due to its direct bandgap of 1.14 - 1.82 eV as shown in **Figure 1.2** [7, 15]. However, these cells are based on rare and toxic materials and their manufacture processes remain a challenge. These factors limit the commercial widespread use of second-generation cells [14].

Figure 1.2 shows power conversion efficiency for various materials of different energy Bandgap. The solid line represents Shockley-Queisser limit (SQ limit) which is the maximum theoretical efficiency of 33.7% for a solar cell with a bandgap of 1.34 eV. While the dashed line represents the global standard spectrum at the earth's surface (AM1.5G = 1000 W/m^2).

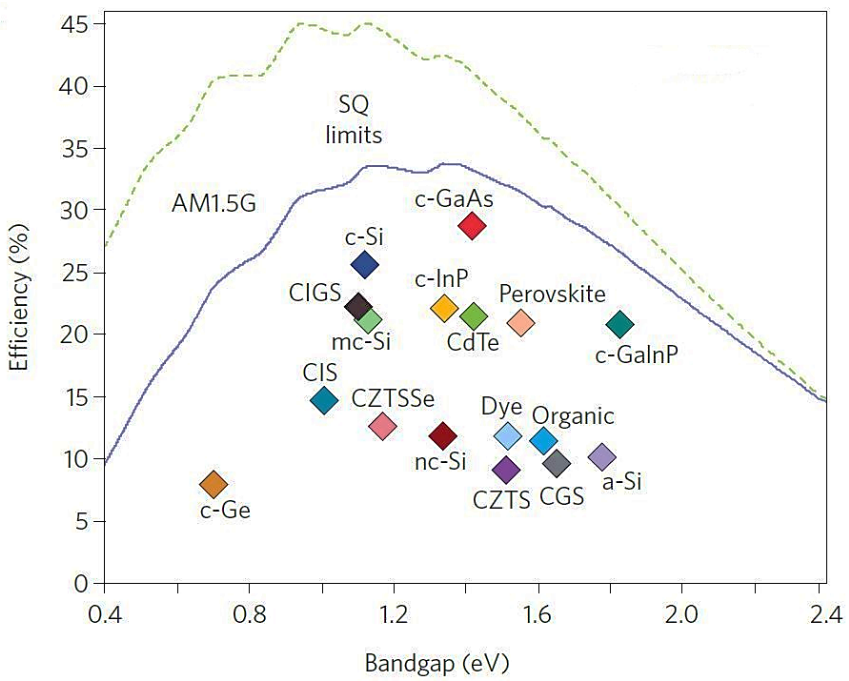

Figure 1.2 Energy-conversion efficiency versus energy Bandgap for various materials (highest experimental values) under global sunlight (AM1.5G), adapted from [14].

Third generation PVs are in development, including: dye-sensitized solar cells [16, 17], quantum dots solar cells [18, 19], perovskite solar cells [20], and organic photovoltaics [21].

Dye sensitized solar cell (DSSC) which can be assumed as a mesoscopic heterojunction solar cell was first obtained in 90's by O'Regan and Grätzel [22]. A single layer of light absorbing dye is coated on nanostructured porous semiconducting oxide layer e.g. TiO_2, deposited on ITO or FTO glass substrate as working electrode. This electrode is placed parallel to glass substrate coated with a thin layer of platinum as counter electrode. The space between two electrodes filled with an electrolyte as a conducting media [22, 23]. DSSCs have advantages over other PVs such as low production cost, enhanced performance under diffuse light, and long life-time stability. However, their lower efficiencies compared with Si PVs due to its corrosive nature, and evaporation of the electrolyte limit its scaling up to large modules. Thus, further development of efficiency and stability of DSSCs is needed.

Quantum Dots-based solar cells, first reported in 1998, have attracted tremendous research interest due to the unique and versatile advantages of QDs, such as wide tunability of band gaps by changing their size, easy solution processability, and impressive capability of generating multiple excitons. Although its efficiency has considerably increased from ~ 1% to over 16%, it still needs further improvement in order to compete with other existing solar cells [18, 19].

A low cost and solution processable solar cell based on a highly crystalline perovskite absorber was first reported by Snaith et al. achieving PCE of 10.9% [20]. Perovskite crystal structure can be described by an ABX_3 unit cell, where A is an organic cation, B is metal cation, and X is a halide ion. B is attached to X in an octahedral configuration, while A is positioned between the adjacent BX_6 octahedron. One of the most applied perovskite materials is methyl ammonium lead iodide ($MAPbI_3$, or MAPI), which has organic cation methyl ammonia $CH3NH^{3+}$ at A, metal ion lead Pb^{2+} at B and halogen anion iodine I^- at X. Despite having potential to replace Si-based solar cell, with low cost fabrication and high efficiency, material toxicity, device hysteresis and stability are major challenges which need to be overcome for a wide scale commercialization [20].

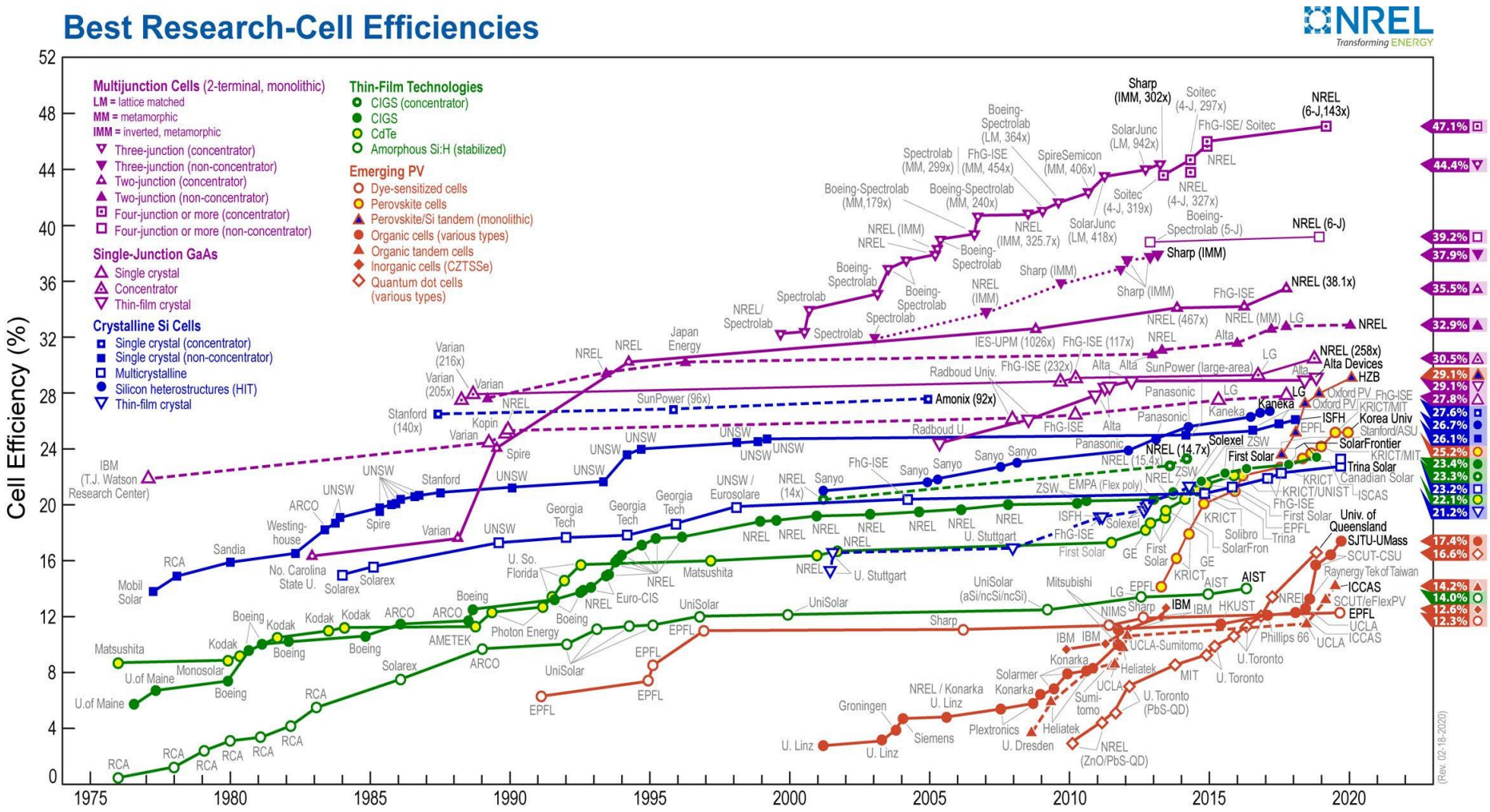

Figure 1.3. The current best research-cell efficiency chart, downloaded from [24].

Emerging OPVs are the lowest in cost, and while their efficiency level has not caught up with first and second generations, they are currently the fastest growing as can be seen in Figure 1.3. They also provide many other advantages, discussed below, and are the main focus of this research.

1.2 Organic Photovoltaics (OPVs)

In recent years, Organic photovoltaics (OPVs) have gained a growing interest as a promising candidate to displace the traditional silicon PVs. This is mainly due to their materials' abundance, solution processability with lightweight, flexible substrates at low temperature, and compatibility with roll-to-roll manufacturing. These advantages can achieve low cost production rates of > 10,000 m^2/hour at fabrication costs as low as £/m^2 and for modules less than 1 £/W_p (Watts peak) [25, 26]. Furthermore, tunable colour and transparency of organic materials are attractive attributes for the integration of PV into building components or other purposes [25].

1.2.1 Active layer development

A decade after the discovery of electrically conductive polymers [27], Tang developed the first successful single bilayer heterojunction organic photovoltaic cells in 1986 using copper phthalocyanine (CuPc) as electron-donor and Perylene tetracarboxylic derivatives as electron-acceptors achieving a PCE reaching 1% [28]. This result represented a major milestone and a significant improvement in the field of PV technology. Later, in 1992, Heeger, Sariciftci et al. first discovered ultrafast photo-induced electron transfer (∼ 50 fs) from conjugated polymer (MEH-PPV) to a fullerene (C60), which opened the possibility of using conjugated polymers as the donor and fullerenes as the acceptor in OPV devices [21]. Afterwards, Sariciftci and Heeger invented the bulk heterojunction (BHJ) structure from a solution of donor and acceptor in order to overcome the thickness and recombination issues [29], This invention was followed by a comprehensive characterization by Heeger et al. and Friend et al. [30, 31]. In the same year, the device performance was further improved by the introduction of new soluble fullerene derivatives [32].

Subsequently, the structure of OPV was further developed with different approaches as follows. Firstly, a single layer OPVs were prepared by thermal evaporation of conjugated polymer between two electrodes of different work functions as shown in Figure 1.4. A very low efficiency of 1% was achieved by using this structure as J_{SC} was quite low due to reduced light absorption [33, 34].

Afterwards, OPVs were fabricated in a bilayer structure in which the donor or acceptor is deposited on top of each other. These devices provide a continuous path of charges towards the corresponding electrodes due to the presence of donor-acceptor interface. However, the excitons may recombine in the bulk of the active layer because the exciton diffusion length of conjugated polymers is limited to less than 20 nm [35, 36]. Therefore, to overcome this recombination issue, an improved fabrication approach was obtained depending on mixing of donor and acceptor materials with different ratios which introduce many interfaces at which excitons can dissociate within its diffusion length. However, tunable morphology is required to overcome the formation of isolated regions and phase separation which trap charges and enhance the bimolecular recombination [37].

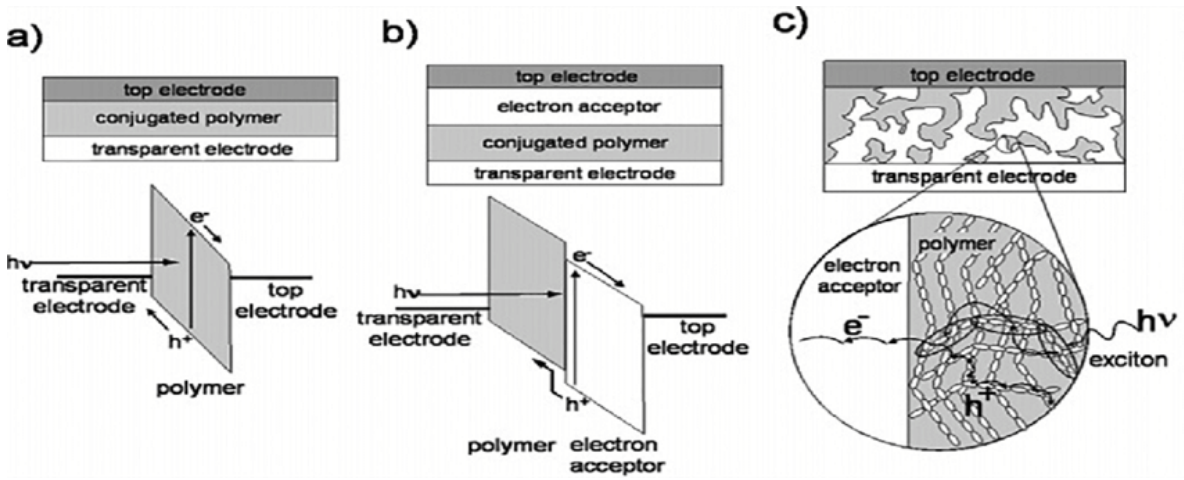

Figure 1.4. The device architectures of conjugated polymer based Organic photovoltaic cells: (a) single-layer, (b) bilayer, (c) bulk heterojunction, adapted from [33].

As a result of extensive research in the last decade, OPVs have been developed and a rapid increase in their power conversion efficiencies (PCEs) exceeding 17.4% [38] for single heterojunction OPVs, and higher than 14.2% [39] for tandem OPVs have been achieved. This significant progress has been realized by comprehensive development and synthesis

of a great variety of novel photoactive donor and acceptor materials [40, 41, 42, 43], optimization of device fabrication conditions [44, 45] developing new device architectures, controlling the film morphology of active layer, and interfacial engineering [46, 47].

1.2.2 Device architectures

There are two types of device structures, conventional and inverted, which is controlled by the position of the charge selective layers (electron transport and hole transport layers ETL, HTL). For the conventional architecture of OPVs, consists of bulk heterojunction (BHJ) of a conjugated polymer i.e. Poly(3-hexylthiophene-2,5-diyl) (P3HT) and a fullerene acceptor, i.e. [6,6]-Phenyl C61 butyric acid methyl ester (PCBM). This BHJ sandwiched between an anode; a conductive transparent substrate typically indium tin oxide (ITO), coated with interlayer such as PEDOT:PSS, and a thin metal cathode, for instance, Ca or LiF/Al, which is usually deposited by thermal evaporation [48, 49] as shown in Figure 1.5.

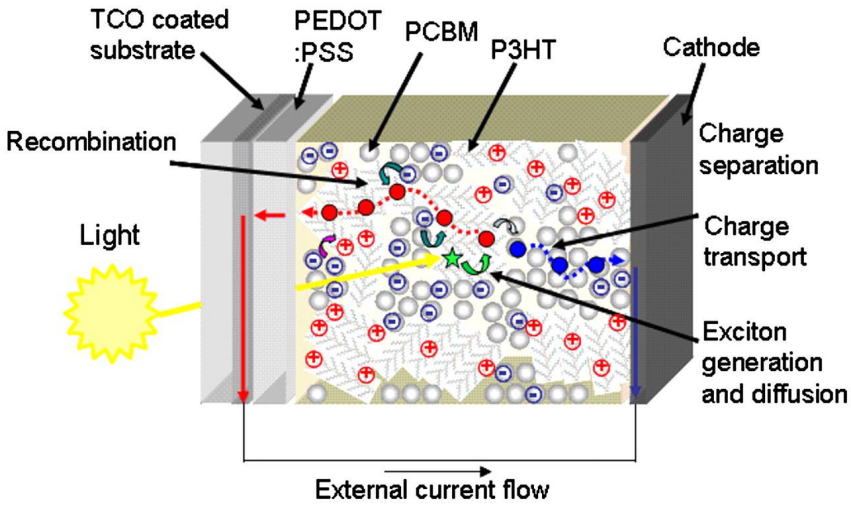

Figure 1.5. The conventional architecture of Bulk heterojunction OPVs taken from [25].

However, the cathode is typically a low work function metal such as Ca or Al which can be easily oxidized upon air exposure. Therefore, an inverted OPV structure, illustrated in Figure 1.6, which not only can provide more stability because the high work function metal, such as Au, Ag, will be at the top as an anode but also delivers better compatibly to roll- to- roll manufacturing since metal anode can be processed from colloidal solution, for example, Ag-NPs [50, 51].

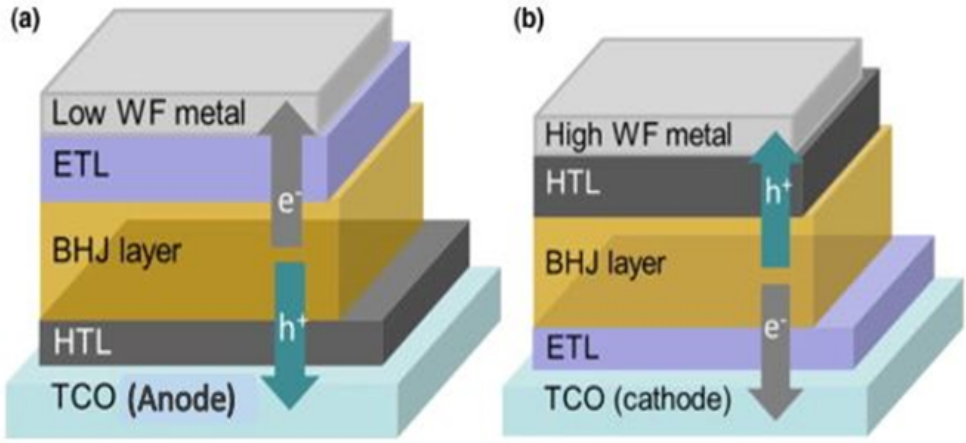

Figure 1.6. Schematic diagram shows (a) conventional and (b) inverted architectures of BHJ OPVs, taken from [52].

1.2.3 The working mechanism of OPV

Upon light illumination on the active layer through the transparent electrode, photogenerated bound electrons-holes (excitons) diffuse towards and dissociate at the donor– acceptor interface, due to the energy levels difference between two semiconductors, into holes in the highest occupied molecular orbital (HOMO) of the donor material and electrons in the lowest unoccupied molecular orbital (LUMO) of the acceptor material. Consequently, the dissociated charges will then drift under the intrinsic electric field created by the difference in work function values of the asymmetric electrodes and eventually, will be collected by the corresponding electrodes [53, 54].

The principal processes occurring in OPV can be summarised as: 1) Light harvesting, 2) exciton (bound electrons-holes) generation, 3) exciton diffusion, 4) exciton dissociation at donor/acceptor interface into holes in the highest occupied molecular orbital (HOMO), and electrons in the lowest unoccupied molecular orbital (LUMO), 5) Charge carrier transport to the electrodes, and 6) Charge carrier extraction and collection at the respective electrode [55, 56]. The optimization of each process will lead to a total improvement in device performance as can be seen in Figure 1.7.

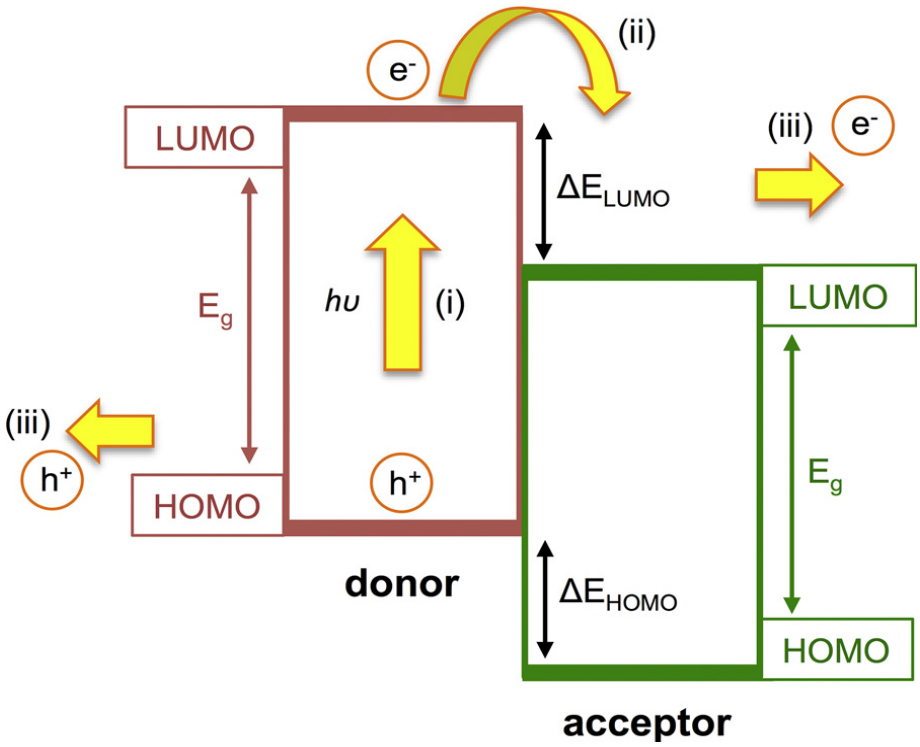

Figure 1.7. Energy level diagram for donor-acceptor heterojunction showing the working mechanism of OPV, with basic processes indicated as follows: (i) light absorption causing an exciton formation; (ii) excitation of the electron to acceptor's LUMO; (iii) electron and hole transfer towards electrodes, taken from [53].

The power conversion efficiency of the solar cell depends on three essential parameters: short-circuit current density (J_{SC}), open-circuit voltage (V_{OC}), fill factor (FF) as illustrated in Figure 1.8. The power conversion efficiency of the solar cell can be determined from the following equation,

$$PCE = \frac{P_m}{P_{in}} = \frac{J_m V_m}{P_{in}} = \frac{J_{SC} V_{OC} \mathrm{FF}}{P_{in}}$$

Where, P_{in} is the power intensity of the incident light, J_{SC} is correlated with the efficiencies of the principal processes occurring in OPV (light absorption, exciton generation and dissociation, charge transport and charge collection at the electrodes), which depend on the charge carrier mobility of the used materials and formation of an Ohmic contact at the interfaces. It can be maximized by utilizing low-band gap polymers that can absorb light at longer wavelengths [43, 57].

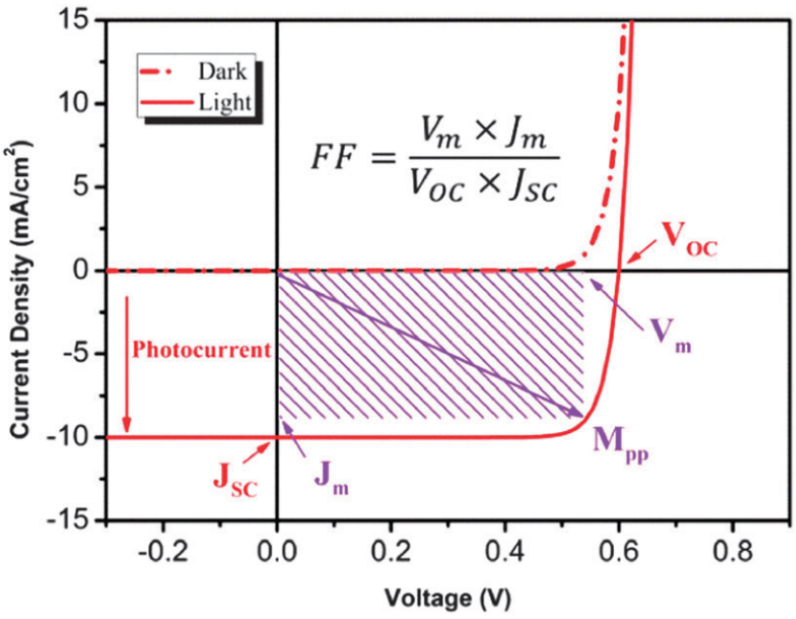

Figure 1.8. The typical J – V characteristics of OPV under dark and light illumination with key parameters identified such as open-circuit voltage (V_{OC}), short-circuit current density (J_{SC}), the maximum current density and voltage (J_m and V_m) at the maximum power point (M_{pp}), and the fill factor (FF), taken from [57].

V_{OC} is determined by the energy difference between HOMO of the donor and LUMO of the acceptor and it can be enhanced by either pinning the Fermi levels/work functions of anode and cathode to the HOMO of donor and LUMO of acceptor respectively or employing a donor with lower HOMO (shifted away from the vacuum level) or an acceptor with higher LUMO (shifted closer to the vacuum level) or both in order to minimize the energy loss during charge dissociation [58].

FF represents the diode quality and it is dependent on series (R_s) and shunt (R_{sh}) resistances of device [57, 58, 59]. In addition, FF relies on the conductivity of electrodes material, the presence of trap states, and the contact at the interfaces between the active layer and electrodes. R_s arises from the overall conductivity of all layers in OPV such as electrodes, electron and hole transport interfacial layers, and active layer and the contact resistance between them. R_{sh} is governed by thin films' quality and the interfaces, for instance, the presence of pinholes will lead to the loss of charge carriers during their transport through the layers of OPV through leakage paths and traps as well as recombination and trapping, which decrease the device performance [60].

1.2.4 Future challenges

Although OPVs have several advantages, including cost-effective production by solution processing techniques, lightweight and flexible structures, and semi-transparency, the OPVs still have lower power conversion efficiency and shorter lifetime than silicon based solar cells. Therefore, to achieve 20% solar cells efficiency, higher module efficiencies (7- 10%), and longer lifetimes (7-10 years) as demonstrated in **Figure 1.9**, progress in a number of main areas should be pursued. These include, the design of new light- harvesting polymers, with a band gap of approx. 1000–1100 nm, more efficient and cost-effective device processing, and stable device architectures [61, 62].

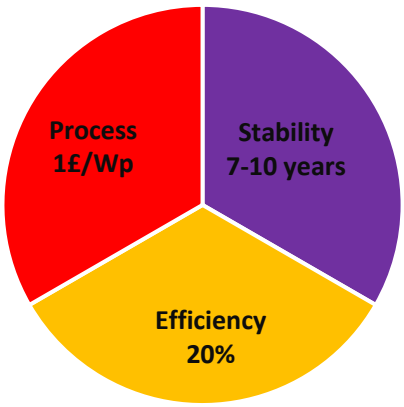

Figure 1.9. A schematic diagram summarizing the challenges of OPVs, taken from [63].

In addition, the above advances need to be combined with the development of new interfacial materials with favourable charge selectivity and solution processability. The appropriate integration of these interlayers with the new photoactive polymers are important for further improve of the efficiency and stability of OPVs.

1.3 Interfacial layers

The performance of OPVs strongly depends on the charge extraction and collection at the corresponding electrodes. Therefore, the insertion of a charge transport layer between the active layer and electrodes, which enhance the collection efficiency, is required to achieve efficient device performance. Interfacial materials are critical components used to improve the electrical and electronic properties between the photoactive layer and the electrodes, furthermore, to tune the work functions of anode and cathode which is the basic requirement for efficient charge collection [64, 65].

Efficient interfacial materials should 1) form an Ohmic contact at BHJ/electrode interfaces; 2) possess suitable valence and conduction bands to improve charge selectivity at corresponding electrodes; 3) have wide bandgap to minimize the light absorption losses; 4) possess high conductivity to decrease resistive losses; 5) have environmental stability to prevent any chemical reactions at interfaces; 6) have solution processability at low temperatures; 7) be produced at low cost [60, 66].

1.3.1 Interlayer Materials

To date, several classes of charge-transport materials for OPVs have been developed such as: conductive conjugated polymers, self-assembled functional materials (SAMs), cross-linkable materials, inorganic transition metal oxides (TMOs), graphene oxides (GO), and other alternatives [67]. The most widely used transparent electrode for optoelectronic devices is Indium Tin oxide (ITO) of WF = - 4.70 eV which cannot form an Ohmic contact with HOMO or LUMO levels of most donor and acceptor materials of the active layer. However, its WF can be modified by using interfacial layers of high or low WF which allow ITO to act as anode or cathode respectively [68].

The charge-transporting layers can be classified, according to the type of extracted charges, into electron transport layers (ETLs), which modify the charge collection efficiency at the cathode, and hole transport layers (HTLs) at the anode in order to enhance the extraction of the holes as shown in Figure 1.10 [66].

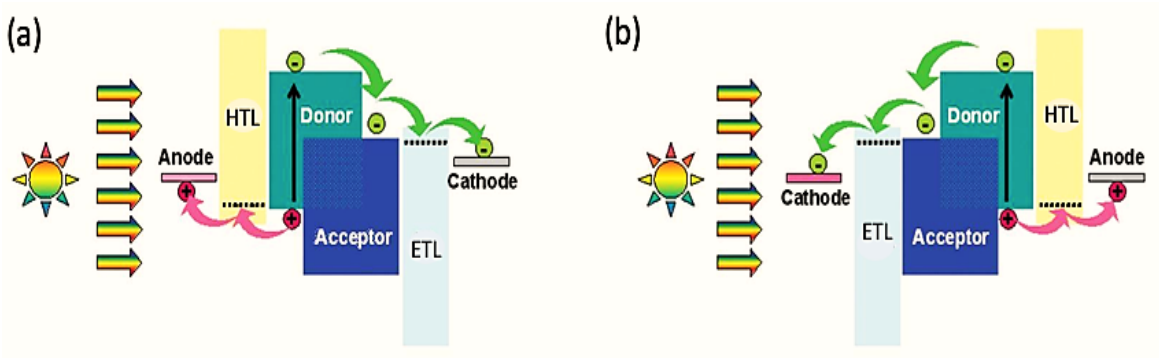

Figure 1.10 Schematic band diagram of OPV device describes the exciton creation and transport processes in (a) Conventential, (b) Inverted architectures, adapted from [66].

ETLs are low work function materials such as ZnO, TiO_2, and Cs_2CO_3 with a Fermi level close to the conduction band. The Fermi level is pinned to the LUMO of the acceptor to enhance the electron transport from the latter to the cathode. Moreover, the ETL's band gap is larger than the organic's HOMO–LUMO gap, then this energy difference will serve as a barrier to block the movement of holes from the HOMO level to the cathode as illustrated in Figure 1.11 [69]. Currently, these materials have been exhibiting high efficiency and stability levels.

While HTLs (high work function) materials should have an appropriate valence band to match the HOMO of the donor, and a large band gap with a conduction band higher than the LUMO of acceptor, for efficiently electron blocking at the anode as shown in Figure 1.11 [70]. PEDOT:PSS is the most common material used as a HTL, but with certain limitations that this research aims to overcome through developing an alternative HTL.

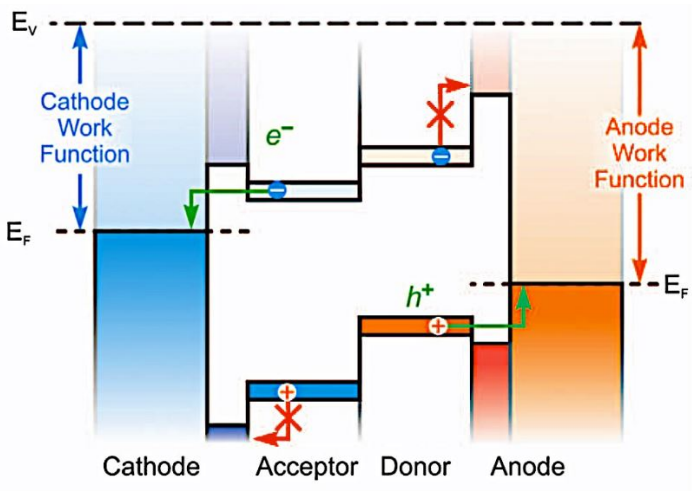

Figure 1.11 A schematic band diagram illustrating the charge selectivity and collection at ETL/acceptor and HTL/donor interfaces, taken from [70].

1.4 PEDOT as a HTL

A conductive polymer, poly(3,4-ethylenedioxythiophene) (PEDOT: PSS), is extensively used solution-processed hole transport interlayer material in optoelectronic devices. PEDOT:PSS is obtained by p-doping of (PEDOT) by poly(styrene sulfonic acid) (PSSH) [71] as shown in **Figure 1.12**. It has a high electrical conductivity of 2.7×10^{-3} S.cm^{-1} which results from the formation of PEDOT^{+}: PSS^{-} [72]. Its electrical conductivity can range from 10^{-6} to 10^{+3} S.cm^{-1} by controlling the compositional ratios of PEDOT^{+} and PSS^{-} or by modifying the microstructure by processing with additives [73].

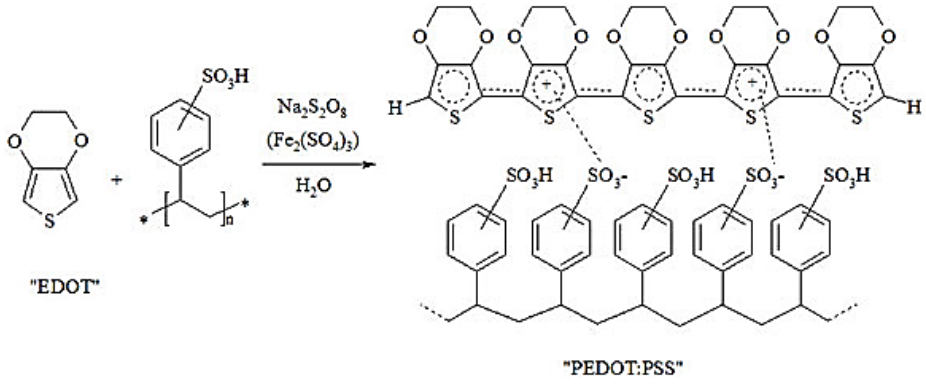

Figure 1.12 the preparation of PEDOT:PSS by polymerization reaction of EDOT monomer and polystyrene sulfonic acid, taken from [71].

PEDOT:PSS is optically transparent over 80% of the Vis-NIR range which minimizes the light absorption losses [74], and its high work function (-5.10 eV) is well-matched with the HOMOs of the commonly used donor polymers forming a good Ohmic contact at BHJ/Anode interface [73]. In addition, the facile solution-processability of PEDOT:PSS enables the throughput fabrication of efficient conventional and inverted OPV devices. For the conventional OPV architecture, PEDOT:PSS planarises the ITO electrode by decreasing its surface roughness and it, moreover, increases its work function for effective hole collection [75, 76].

On the other hand, the acidic (pH: 1–2) and hygroscopic nature of PEDOT:PSS etches ITO and allows the diffusion of In ions into PEDOT:PSS and the active layer, which causes degradation of both materials and instability at the ITO/PEDOT:PSS interface [72]. Its electrical and structural inhomogeneity, which stems from the insulating PSS layer limits the charge collection [77]. Furthermore, the deficient electron-blocking capability for some acceptors and poor adhesion properties of hydrophilic PEDOT:PSS onto the hydrophilic organic active layer result in lower device performance due to bad electrical properties and film morphology [78].

In addition to these issues caused by PEDOT:PSS, the conventional structure of OPV also suffers from other drawbacks such as 1) the low work function metal electrodes (Ca, LiF) are easily oxidized in the air increasing the series resistance at BHJ/metal interface and cause device degradation [63], 2) the vertical phase separation of P3HT/PCBM blend during the film formation in which PCBM-rich layer is mainly concentrated at the bottom (anode), while P3HT-rich is formed at the cathode as shown in Figure 1.13 [79].

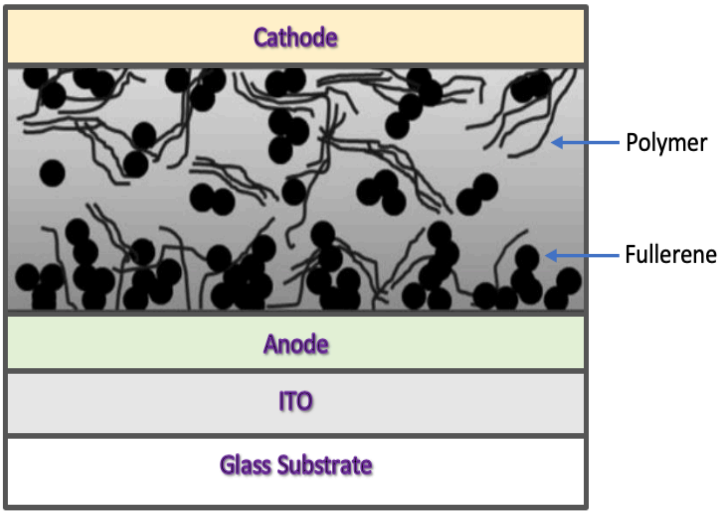

Figure 1.13 A schematic diagram shows the vertical phase separation of polymer and fullerene, adapted from [79].

These issues can be tackled by using the inverted OPV structure, which not only can provide more stability because the high work function metal, such as Au, Ag, will be at the top as an anode but also delivers better compatibly to roll-to-roll manufacturing since metal anode can be processed from colloidal solution, for example, Ag-NPs. However, in the inverted cells, Ag ions can diffuse into PEDOT:PSS layer and form electrical short paths [80, 81]. Furthermore, PEDOT:PSS can easily absorb the moisture and oxygen which change its structure and reduce its electrical conductivity [82]. Hence, there is an essential demand to develop alternative interfacial materials with high stability and appropriate charge selectivity to replace PEDOT:PSS. There are several alternatives for PEDOT:PSS such as, CuI, [83, 84], CuSCN [85, 86], graphene oxide (GO) and the most promising material are the TMOs.

1.5 Graphene oxide (GO)

Graphene oxide (GO) is an oxidized derivative of graphene, which can be synthetized by the treatment of the naturally abundant inexpensive graphite powder with strong oxidizers [87,88] as shown in **Figure 1.14** and can be produced as stable dispersions in different solvents [89]. GO has unique optoelectronic properties, 2-dimensional honeycomb structure, and low cost solution process, which make it a promising candidate for wide range of electronic devices such as an efficient hole-transport material in OPVs [90, 91].

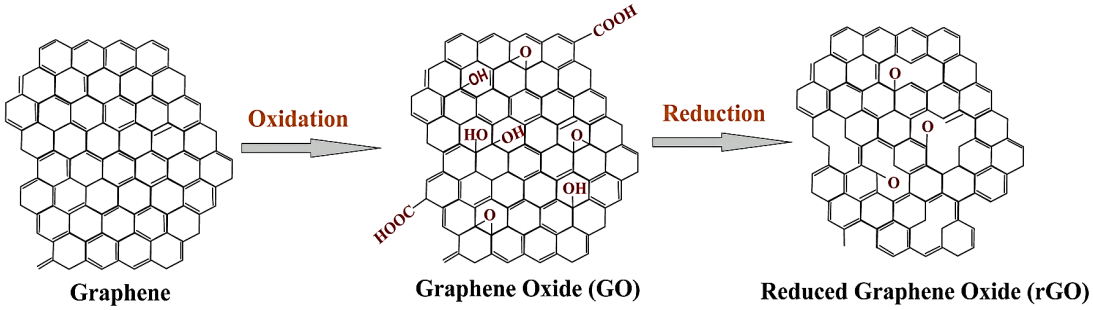

Figure 1.14 The preparation of graphene oxide and reduced graphene oxide via oxidation and reduction reactions, taken from [92].

The bandgap, HOMO, LUMO of GO are 3.60 eV, -5.20 eV and -1.60 eV, respectively and the work function of GO ≈ - 4.70 eV [88], which can match well with many HOMOs of organic donors and thus significantly enhances the Ohmic contact at the active layer/anode interface. All these characteristics make GO a potential hole selective and transport material for OPVs [87].

GO was first reported by Li et al. as an efficient HTL in P3HT:PCBM-based OPV and exhibited PCE of 3.5% [87]. Later, Gao et al. utilized GO as HTL in inverted OPV structure and 3.6 % PCE was achieved suggesting that GO decreases the charge recombination rate and suppress the leakage current through efficient electrons-blocking and holes-transporting to ITO [93]. However, the insulating nature of GO which arises from the covalent bonds of C–O of the hexagonal graphene lattice, limits its thickness to 2 nm for application in devices which increases the series resistance, thus decreasing the device performance, this significantly hampers the use of GO as HTL in OPVs [87, 94,95].

In this regard, reduced graphene oxide (rGO) was introduced by removing the oxygen containing groups as shown in Figure 1.14, during annealing at ~ 250 °C and this process can be performed by several chemical [96], thermal [97], or photochemical methods [98] in order to improve the GO's conductivity [99]. Nevertheless, the poor solubility of rGO in common solvents, which produces poor film morphology and surface coverage on substrates, hinders its applications as solution-processed HTL in OPVs [100, 101].

The work function (WF) of GO can be tuned to -5.20 eV by O_2 plasma post-treatment, which is higher than that of GO (-5.0 eV). This higher WF results from surface C=O dipoles created by removing electrons from graphene [102]. The chemically modified GO HTL enhanced the device performance 30% higher than using GO as HTL [103]. The WF of GO can also be tuned to 5.21 eV by Photochemical chlorination process. The chlorinated graphene oxide (Cl-GO) films showed good optical transparency and hole-transport property as HTLs [104]. In addition, GO was also blended with transition metal oxides such as NiO_X [105] and VO_X [106] in order to improve the electron-blocking capability and energy levels alignment between ITO and the active layer, which results in improved FF, PCE and stability of PVs [107, 108].

1.6 Transition metal oxides (TMOs)

Transition metal oxides (TMOs) were first introduced by Tokito in 1996 as anode buffer layers in OLEDs [109]. These oxides have been comprehensively investigated in OPVs owing to the tunable electronic structures which form Ohmic contact with HOMOs and LUMOs of active layer, large bandgap that provide decent optical transmission in Vis-NIR regions, environmental stability, and their compatibility with low cost roll-to-roll processing techniques at low temperatures. These unique properties make them attractive candidates as hole transport layers (HTLs) and electron transport layers (ETLs) in both conventional and inverted architecture of OPVs by tuning work function to the desired level [110, 111].

TMOs can be employed as HTLs or ETLs owing to the wide range of work functions (WF), which span from 3.5 eV for defective ZrO_2 to high WF value of 7.0 eV for stoichiometric V_2O_5 [70,112]. The work function values for a given transition metal oxide can span over 1.0 eV. For example, the reported work function values for MoO_3 range from 5.3 to 6.90 eV

[113, 114, 115]. Furthermore, the WF of TMOs is strongly influenced by oxidation states, surface treatments, concentration of defects, and deposition methods as shown in **Figure 1.15** [116, 117].

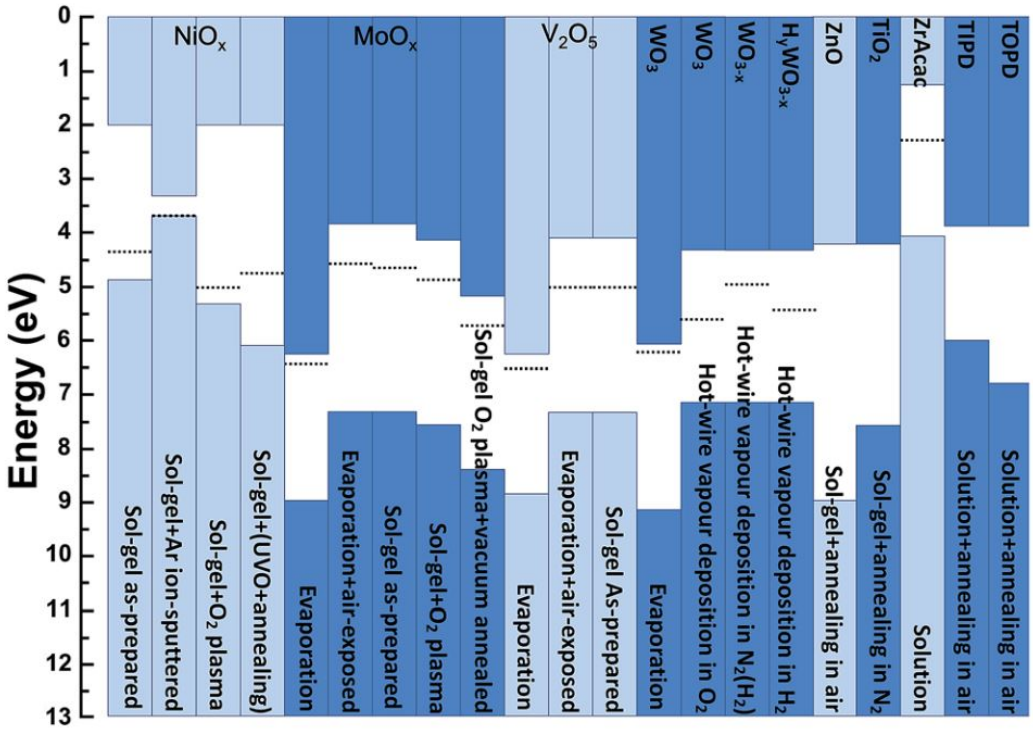

Figure 1.15 A schematic diagram of energy levels of metal oxides prepared using different methods, taken from [117].

1.6.1 Dependence of TMOs work function on oxidation states and defects

Theoretically, the Fermi level of a stoichiometric semiconducting metal oxide would be midway between the valence band maximum and the conduction band minimum. However, a stoichiometric oxide (an oxide without any defects) cannot realistically exist, as there will always be some certain concentration of defects [70].

TMOs behave as either a p-or n-type semiconductor due to the intrinsic defects (such as oxygen or metal vacancies) which affect both semi-conductivity nature and work function of TMOs. These defects result in new occupied or unoccupied states near the conduction band or valence band edges and consequently shift the fermi level within the band gap [70, 118]. For example, an oxygen vacancy would create excess of metal cations with extra

electrons. These electrons occupy states close to the conduction band minimum, and thus make an oxide act as n-type such as MoO_3 [119], in which the oxygen vacancy is most stable defect. Whereas metal deficiency (or excess oxygen) would result in unoccupied states close to the valence-band maximum and makes an oxide behave as p-type such as Cu_2O in which Cu vacancy is the most stable defect [120].

If the oxidation state of a given TMO is decreased by removal of oxygen forming oxygen vacancies and an excess of metal cations, this shifts the Fermi level closer to the conduction band minimum, which likely tends to decrease work function and identifying the oxide as n-type. Conversely, if the oxidation state is increased, metal vacancies are formed which result in an excess of oxygen and Fermi level moved closer to valance band maximum Thus adding oxygen makes an oxide behaves more as p-type and increases the work function as shown in **Figure 1.16** [70, 121]. As a consequence, oxide's interfacial properties and work function can be tuned by inducing oxygen vacancies (decrease in the oxide's work function) such as ZrO_2 whereas, increasing an oxide's work function by inducing metal vacancies, such as NiO [122, 123].

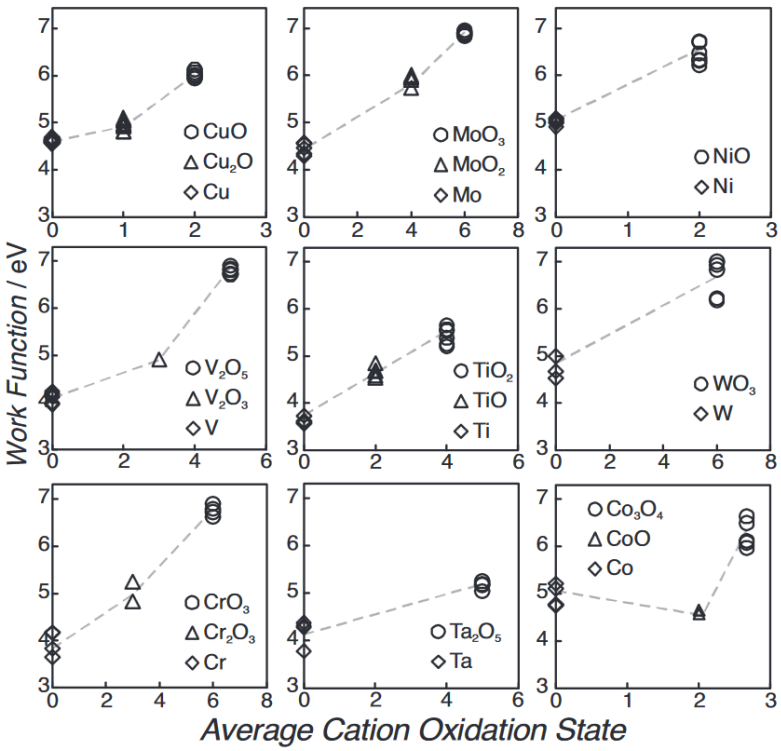

Figure 1.16 The dependence of work function on oxidation state of transition metal oxides, taken from [70].

As many oxides, due to intrinsic defects, are p- or n-type semiconductors and have tunable work function, it is possible to be used as selective charge transport layers which decreases the energy barrier for only one type of charge carrier. This property is particularly important for OPVs because it decreases the leakage currents and increases the device performance [46].

The Fermi level of a low work-function n-type cathode interlayer is pinned to the LUMO of acceptor in the BHJ layer. Then, the excited electrons move from LUMO level to the electrode via its conduction band. However, if the oxide's band gap is larger than the organic's HOMO–LUMO gap, then holes will have an energy barrier for blocking hopping from the HOMO level to the electrode such as MoO_3, WO_3, ZnO, and TiO_2 [124, 125, 126, 127, 128]. For p-type anode interlayer (high work function oxide), the fermi level is pinned to the HOMO level of the donor material in photoactive layer. Therefore, the holes can easily be transported through the oxide's valence band. While the oxide's conduction band is sufficiently higher than the LUMO of both organic donor and acceptor materials, which effectively blocks electron leakage through the anode such as NiO and CuO_x [129, 130].

Consequently, a low-work function, n-type semiconductor with a large band gap would be the optimal interfacial layer for the cathode of an OPV, and the optimal anode layer would be a high-work-function, p-type semiconductor with a large band gap as shown in **Figure 1.17** [46,131].

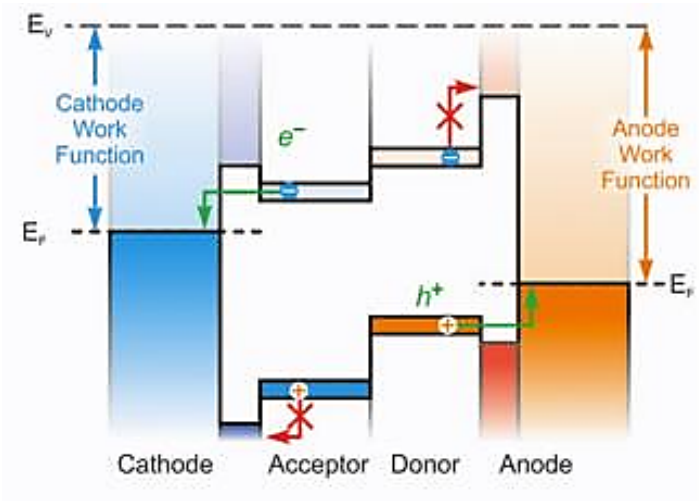

Figure 1.17 Schematic energy-level diagram of charge-selective buffer layers at OPV interfaces, taken from [70].

1.6.2 Composition of TMOs

There are many factors that influence metal oxide's electronic properties, for example, crystal symmetry, metal-oxygen bond length, valence electron population, degree of ionic or covalent bond character and electron correlation effects. Consequently, their diverse set of electronic structures affects their conductivity properties [132].

Transition metals are elements whose atoms or their cations have an incomplete d sub-shell as shown in Table 1.1. The valence band of TMOs derives from the occupied O 2p orbital, which originates from oxygen anion and are completely filled while the conduction band derives from the unoccupied d orbital of transition metal [132].

Table 1.1 The electronic configuration, bandgap, and work function of n-type TMOs reviewed in this chapter and p-type TMOs studied in this research.

Metal Oxide	Electronic configuration of the corresponding metal	Band gap (eV)	Work Function (eV)	Ref
MoO_3	[Ar] $3d^3\,4s^2$	2.70	4.90 – 5.10	133
V_2O_5	[Kr] $4d^5\,5s^1$	2.80	5.60	134
WO_3	[Xe] $4f^{14}\,5d^4\,6s^2$	3.20–3.40	4.80	135
NiO	[Ar] $3d^8\,4s^2$	3.60 - 3.70	5.00	130
Cu_2O	[Ar] $3d^{10}\,4s^1$	2.10 – 2.60	5.30	136

1.6.3 Classes of TMOs

Transition metal oxides can be categorized according to their d level's occupancy into 4 categories as shown in **Figure 1.18**. Class 1 is totally empty d bands (d^0) oxides which are n-type materials because they have a natural affinity to form oxygen vacancy defects. However, they are considered to be insulators when they are completely stoichiometric [70, 137]. Their conduction band minima is consisted mainly of empty metal d states, while valence-band maxima are composed predominantly of O 2p states. Class 2 are partially occupied d bands oxides with a low number of electrons (for example, d^1, d^2 and d^3). These oxides are often metallic formed by chemical reduction of d^0 oxides. Class 3 should be metallic conductors as they have a partially filled d band with a high number of electrons (for example, d^7, d^8 and d^9). However, these oxides are electrical insulators. Class 4 oxides are of totally filled d bands (d^{10}). They are semiconductors due to the gap between the d band and the next-highest energy band (metal s orbitals). These oxides behave as intrinsic p-type semiconductors, where the Fermi level lies closer to the valence band than the conduction band and due to the presence of cation vacancy defects [138, 139].

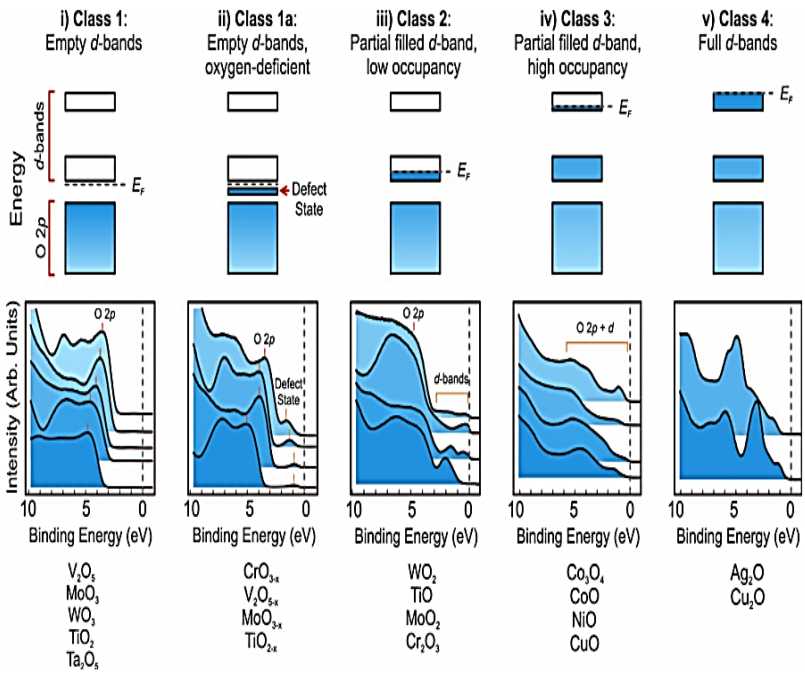

Figure 1.18 (top) A schematic diagrams of energy band and (bottom) photoemission spectra of valance band of various transition metal oxide classes, taken from [70].

1.6.4 Synthetic routes of TMOs

In earlier reports, most of metal oxides buffer layers were mainly prepared through thermal vacuum deposition processes. Although these methods deposit smooth films with controlled thickness on wide range of substrates, they require high temperature processing, and expensive vacuum equipment. These drawbacks limit the compatibility with the high throughput and the low-cost device fabrication [117]. Therefore, transition metal oxides prepared from solution processes at low temperatures are needed. The different synthetic routes and processing procedures including precursors, chemical reactions, deposition techniques, and post-treatment are illustrated in Figure 1.19.

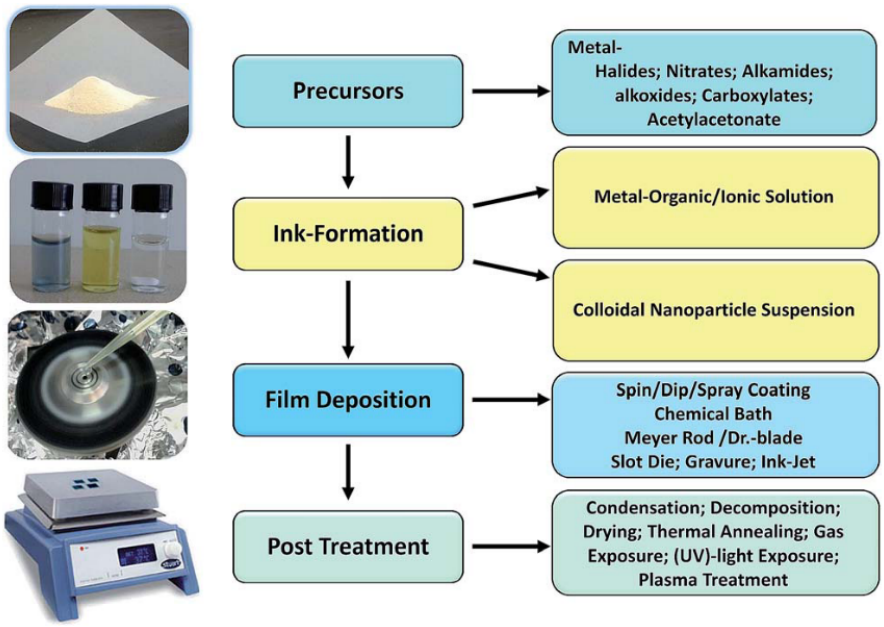

Figure 1.19 Flow chart of typical synthetic routes for solution processing of TMOs, taken from [117].

Metal oxides can be synthesized at low temperatures by dispersion of nanoparticles (NPs) using appropriate stabilizing agents to avoid NPs' accumulation and to increase the solubility in various solvents [140]. These capping agents must be removed by post-treatment such as UV-ozone, O_2-Plasma, and thermal annealing in order to improve the charge carrier mobility in the resultant film [141]. Although NPs approach decreases the required annealing temperatures, NPs tend to form rough films due to their aggregations in larger parts with large size of 100 nm, which are undesirable for the deposition of an

upper photoactive layer and these aggregations may act as electrical shorts causing decrease in the device performance especially for large-scale devices [142].

Alternatively, sol–gel process can be considered. This process is based on converting the sol into gel by hydrolysis of the organic or inorganic precursor of the metal compound by using an appropriate solvent. Then the gel is annealed at a certain temperature to form the oxide [143]. There are several precursors, solvents, and additives have been used in sol-gel method to produce solution processed metal oxides for optoelectronic applications. Among these precursors, inorganic salts, such as halides and nitrates. However, the difficult removal of their anionic species residues limits the device performance and stability [144]. On the other hand, organic precursors such as acetylacetonates, alkoxides and carboxylates have been commonly used to prepare solution processed metal oxide as the organic groups decompose into volatile products during the post treatment as well as its cost-effective and commercial availability of these precursors [145].

The acetate ion (CH_3COO^-) is the most widely used carboxylates for preparation of metal oxides due to their solution processability with aqueous and alcoholic solutions. Most of metal Alkoxides have excellent solubility in their corresponding alcohols as the metal is bonded with alkyl groups through an intermediate oxygen atom. In addition, Acetylacetonates can be formed from most metals such as molybdenum and vanadium [146]. With the proper choice of precursor, the solvent must have several requirements, for example, 1) appropriate viscosity, volatility, surface tension, thus the solution can spread out easily on the substrate and form pinhole-free layer; 2) low boiling point, so it can be removed easily during post treatment [147].

In spite of the several advantages of sol–gel method, such as, the low cost, simplicity, and film thickness adjustability, such sol–gel-deposited TMOs usually require post-annealing at high temperature (250–500 °C) in order to achieve high crystallinity and remove the organic residues. This high temperature treatment approach is incompatible with the high- throughput fabrication of OPVs. [116] Therefore, a novel ‘combustion’ approach has been introduced by Kim *et al.* for solution processing of TMOs at much lower annealing temperatures (< 200 °C) [148]. The exothermic combustion reaction supplies an internal energy, reducing the high post-annealing temperature. The combustion precursor consists

of three main components, including 1) metal, 2) oxidizer, such as nitrates, and 3) fuel, for example, urea or acetylacetone as shown in **Figure 1.20** [149].

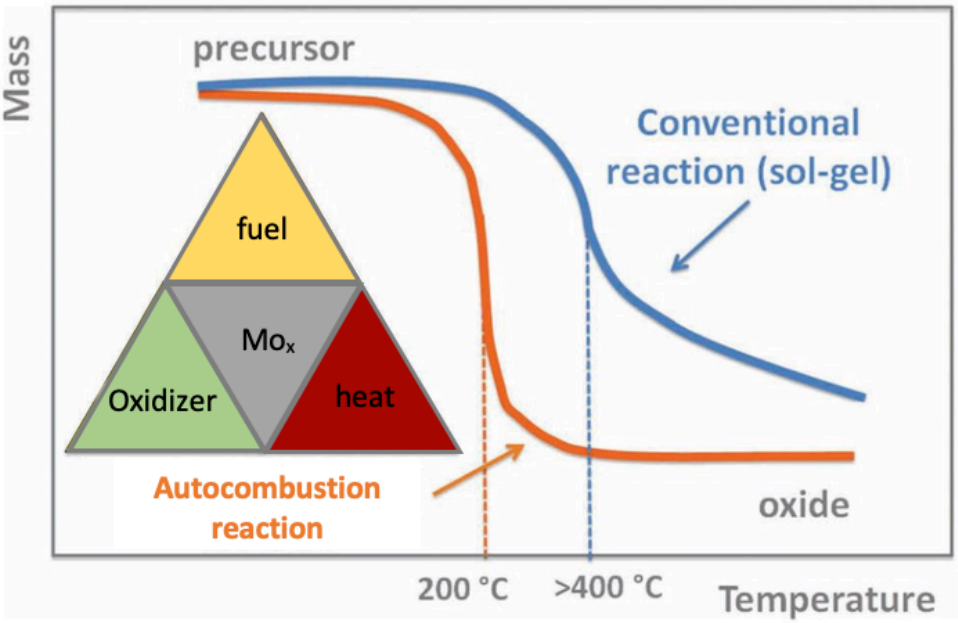

Figure 1.20 The decomposition profile of a combustion and conventional sol-gel reactions, adapted from [149].

Metal oxides can be employed in OPVs as ETLs (such as ZnO, TiO_2) and HTLs (such as MoO_3, V_2O_5, WO_3). In the following, various metal oxides as HTLs were reviewed in order to explore a novel synthetic route for NiO and Cu_2O, which are the main focus of this thesis. An overview of NiO and Cu_2O will be discussed in more details in chapters 3 & 4 respectively.

1.7 Review on TMOs as charge transport layers

1.7.1 Molybdenum trioxide (MoO_3)

MoO_3, n-type semiconductor, was first used as an efficient hole injection material in OLEDs [109] and then it has been comprehensively researched as HTL in OPVs owing to the decent optical transparency, better environmental stability compared to PEDOT:PSS, which prevents the diffusion of metal ions and oxygen inside the active layer, thus preventing the fast degradation of OPV device [150]. The unoccupied 4d orbital of molybdenum and occupied oxygen 2p orbital determines the conduction band and valence band of the oxide

respectively. Furthermore, the electronic structure of MoO_3 depends on the oxidation state of molybdenum cation [112].

The n-type nature stems from the compensation of negative charge at defect sites of oxygen vacancies or cation interstitials which gives rise to the defect band that lifts the Fermi level closer to the conduction band [112]. In addition, MoO_3 has high work function (4.90 – 5.10 eV) [133], which is higher than HOMO levels of most donor materials widely used in OPVs, and in turn it facilitates the hole extraction efficiently at the BHJ/anode interface and forms an Ohmic contact. However, the work function of MoO_3 depends strongly on the stoichiometry and surface contamination [133].

The electronic structure of MoO_3 consists of deep-lying valence band, and conduction band (CB) significantly deeper than most HOMO levels of common polymers, thus the holes are not transported through the VB of MoO_3, the hole transport is occurred through electron extraction from HOMO level of organic semiconductor material to CB of MoO_3. The energy difference (HOMO offset) between the HOMO levels and Fermi level will reach a minimum value, leading to Fermi level pinning at the oxide interface to establish thermodynamic equilibrium [150].

MoO_3 acts as an efficient p-type dopant (hole extraction layer) more accurately than (hole transport layer) due to the interfacial p-doping through is thermodynamically electron transfer from the HOMO level of organic semiconductor to the low-lying conduction band of MoO_3. In other words, the electrons are transported from anode to the MoO_3/BHJ interface through the CB of MoO_3, and subsequently recombine with holes in the HOMO level of the donor [112].

Molybdenum oxide (MoO_3) was first deposited by thermal evaporation, because of its low melting temperature (795 °C), which allows accurate thickness control at a nanometer scale (3 nm) [151]. Thermally evaporated MoO_3 acts as a barrier to the diffusion of oxygen and metal ions inside the active layer, thus preventing fast device degradation. Thus, a thin layer of MoO_3 could be the best HTL for inverted BHJs.

After MoO_3 was introduced by thermal evaporation method to act as HTLs in OPVs [115], more attention has been attracted to developing solution processed MoO_3 to simplify large

scale device fabrication and to reduce the processing costs. Therefore, an exploration of better precursors and processing conditions is needed.

Liu et al. first introduced solution-processed MoO_3 as HTL in OPVs, achieving PCE of 3.14% in P3HT:PC_{60}BM-based conventional OPV which was higher than that of PEDOT:PSS HTL device [152]. This oxide was prepared via wet chemical deposition from an aqueous solution of ammonium molybdate ($(NH_4)_6Mo_7O_{24}$) in addition of hydrochloric acid, followed by thermal annealing at 160 °C for 10 min in nitrogen atmosphere. However, the poor film uniformity limits its application for large scale manufacturing.

Afterwards, Murase et al. utilized the same precursor (ammonium molybdate) and obtained a smooth MoO_3 thin film with a low surface roughness of 2.7 nm at lower annealing condition 100 °C in air. OPVs using this solution-processed MoO_x showed a comparable PCE to PEDOT:PSS based devices and high fill factor of 69.3% [153].

In the meantime, Yang et al. and Girotto et al. both obtained higher PCE of 5.86% when MoO_3 was employed as an anode buffer layer in PBDT-DTNT:PC_{70}BM based OPV of conventional architecture compared to 5.89% of PEDOT:PSS standard device [154, 155]. This MoO_3 was synthetized by dissolving Mo powder in methanol or MoO_3 powder in 2- methoxyethanol with addition of H_2O_2 (30%) at 80 °C for 2 hours. Then the hydrolysis process was carried out during an annealing treatment at 250 °C or 275 °C for 30 min in air. A pinholes-free surface morphology was obtained with low surface roughness of 0.46 nm. The OPVs employing the solution processed MoO3 as HTL exhibited a similar performance as PEDOT:PSS-based devices[154].

Meyer et al. first prepared solution processed MoO_3 by using nanoparticles (NPs) approach in which 15 nm of crystalline MoO_3 NPs were dispersed in xylene by adding 1%wt of copolymer as dispersing agent, that was finally removed with O_2-plasma treatment [156]. The work function of the MoO3 NPs film can be increased to 6 eV by thermal annealing in Nitrogen atmosphere at 100 – 200 °C. In addition, some electrical properties were improved such as low leakage-current and low interface barrier energy compared to that of PEDOT:PSS films. However, some large particle clusters up to 100 nm in size were found in the resulting films which led to lower PCE of 2.5% than that of standard cells [156].

A novel precursor, bis(2,4-pentanedionate) molybdenum dioxide ($MoO_2(acac)_2$), was reported by Jasieniak et al. to obtain s-MoO_x by either an anhydrous or an ambient synthetic route [157]. The precursor was heated in either anhydrous methanol under nitrogen atmosphere or in methanol in air for anhydrous and ambient routes respectively. The deposited MoO_x films were very smooth with low surface roughness (RMS = 0.35 nm). In spite of the significant difference in surface compositions of MoO_x films prepared via two different methods, the performances of the devices were similar at various annealing temperatures. However, this method needs high temperature annealing in order to remove the organic residues [157].

Zilberberg et al. obtained MoO_x of high work function (5.30 eV) from the same precursor ($MoO_2(acac)_2$) but used isopropanol as a solvent instead of Methanol [158]. The hydrolysis process was carried out by maintaining the solution in ambient air for 1 hour. The deposited MoO_x films was then thermally annealed for 20 min at 150 °C in a nitrogen atmosphere. A comparable device performance and long life-time stability of solution-processed MoO_x HTL were achieved compared to thermally evaporated MoO_3 and PEDOT:PSS HTLs respectively [158].

Subsequently, Tan et al. showed a smooth MoO_x film (RMS < 3nm) demonstrating high hole mobility and high light transmittance by modifying the same recipe ($MoO_2(acac)_2$) at lower annealing temperature 150 °C for only 10 min in the air. The resulting MoOx film showed a better device stability than PEDOT:PSS which maintained 94% and 88% of its initial PCE value respectively after being stored in nitrogen filled glove-box for 35 days [159].

Meanwhile, Hammond et al. introduced molybdenum tricarbonyl trispropionitrile ($Mo(CO)_3(EtCN)_3$) dissolved in acetonitrile solution under nitrogen atmosphere, as a promising precursor for lowering the annealing temperature to 120 °C in the air. The resulting MoO_3 film has a WF of 5.15 eV and was increased to 5.38 eV by additional O_2- plasma treatment. PCE of 3.5% was reported when MoO_3 films were incorporated into P3HT:PC_{60}BM device [133].

Next, Xie et al. have proposed one-step synthetic route of low-temperature, solution processed MoO_x via oxidation of hydrogen molybdenum oxide bronze ($HxMoO_3$) and H_2O_2

with controlling the oxidation rate by adding ethanol as reducing agent and annealing temperature lower than 100 °C. A high PCE of over 7.7% was achieved by using a smooth layer of MoO_x (RMS = 1.33 nm) compared to 7.2% PCE of PEDOT:PSS HTL [160].

The stoichiometry of MoO_x film shows a strong dependence on the annealing temperature, which affect the hole transport properties and result efficient HTLs. Furthermore, the work function of MoO_x can be well-aligned to the HOMO level of the donor material by vacuum treatment [161]. In addition, the PCE could be further improved to ≈ 8% by incorporating silver nanoparticles (Ag NPs) into the MoO_x solution, thus forming a MoO_x –Ag NP composite HTL [162, 163].

Notably, pure MoO_3 was realized by thermal decomposition of molybdenum (V) ethoxide precursor dissolved in ethanol at 150 °C in the air [164]. Yao et al. proposed a combustion process from an aqueous solution of polyoxomolybdate precursor in addition to acetylacetone as a fuel and HNO_3 as an oxidizer and an oxidizer, and low transformation temperature of the precursor at 150 °C which provide a continuous film of 2.2 nm RMS [165].

Recently, hybrid graphene-MoO_3 particles (G-MoO_3) were prepared via a facile hydrothermal method by Dang et al. A high PCE of 7.07% was achieved when G-MoO_3 was employed as HTL in PCDTBT:$PC_{71}BM$ devices which is 19% higher than devices with MoO_3 HTLs [166,167]. Meanwhile, a mixture of n-type MoO_3 and p-type NiO_x (MoO_3:NiO_x) was first introduced by Bai et al. This mixture was used as a HTL in PBDBT:IT-M based OPV achieving 10.81% compared to 9.79%, 8.97%, and 9.51% for control devices with PEDOT:PSS, MoO_3, and NiOx as HTLs respectively [168].

MoO_3 and NiOx and were prepared from Bis(2,4 pentanedionato)molybdenum(VI) dioxide ($MoO_2(acac)_2$) and Nickel (II) acetylaceonate ($Ni(acaca)_2$) precursors dissolved in isopropanol. Afterwards, MoO_3 film was developed via solution process of molybdenum(VI) chloride presorsor followed by ultraviolet irradiation treatment. This oxide was employed as anode buffer layer in non-Fullerene:polymer (PBDB-T:ITIC) achieving PCE 9.27% compared to 9.15% for PEDOT:PSS based devices [169].

1.7.2 Tungsten trioxide (WO_3)

WO_3 has been considered as a promising HTL for OPVs owing to the decent optical characteristics (optical band gap ~ 3.20 – 3.40 eV, which can be decreased by 0.5 upon annealing in air), and high work function (-4.80 eV) which improves the hole transport properties [134]. WO_3 is n-type metal oxide with deep-lying electronic states, conduction band is very close to the Fermi level and valance band around 3.0 eV below the Fermi level [170, 171]. Its n-type nature arises from the compensation of negative charge at defect sites of oxygen vacancy or metal interstitials. The electronic structure of WO_3 provides excellent electron blocking and hole transport properties as its conduction band is higher than LUMOs of many donors, and its valence band is well matching with HOMOs of many donors. Similar to MoO_3, the electronic structure of WO_3 exhibit high dependence on the stoichiometry, the crystalline structure and thus the deposition conditions [171, 172]

Stubhan et al. introduced the deposition of WO_3 films from nanoparticles (NPs) route. WO_3 was prepared from NPs suspension of WO_3 in an alcohol solvent annealed at low temperature 80 °C for 5 minutes without any O_2-plasma treatment which is an essential step in order to remove the dispersing agent and to improve the hole transport properties. The WO_3 film of work function 5.35 eV and 6 nm surface roughness was prepared by doctor blade method form a suspension of 7 nm particle size WO_3. A comparable device performance was achieved using WO_3 NPs as HTL for both standard and inverted device structure [134].

Subsequently, Tan et al. reported sol-gel WO_3 film with a small surface roughness of 2.6 nm and high hole mobility of 9.4 x 10^{-3} cm^2 V^{-1} s^{-1}. WO_3 was prepared from tungsten(VI) isopropoxide ($W(OC_3H_7)_6$ dissolved in isopropanol solution, followed by thermal annealing at 150 °C for 10 min in air in order to achieve a complete decomposition of the precursor into WO_3 [170]. An enhanced performance (PCE of 6.36%) for P3HT:ICBA based devices when using WO_3 film as HTL was achieve compared with PEDOT:PSS control devices[170]. Afterwards, Choi et al. enhanced the device stability by keeping 90% of the initial PCE value after nearly 200 hours of air exposure without any encapsulation. This was done by utilizing annealing-free WO_3 as HTL which was prepared via the overnight hydrolysis of ethanol solution of tungsten ethoxide ($W(OC_2H_5)_6$) precursor in ambient without any post

treatment [173]. A 3.4% PCE was reported for a conventional P3HT:PCBM device structure. However, the device performance showed a dependence on the variation of WO_3 layer thickness [173].

Next, Özer et al. prepared solution processed WO_3 via sol-gel deposition from the hydrolysis of tungsten oxychloride ($WOClO_4$) solution in ethanol at 250 °C [174]. Lower annealing temperature 180 °C was obtained by using a different solvent (isopropanol) with the same precursor ($WOClO_4$) [175]. Huang et al. prepared a mixture of WO_3 and V_2O_5 particles dissolved in isopropanol solution which enhanced the device performance compared to devices based on only V_2O_5 or WO_3 as HTLs. This was attributed to the efficient hole transport which due to the well-alignment between valance band of V_2O_5 and HOMO of donor material in addition to the electron extraction from the top silver electrode through the conduction band of WO_3 [176].

Ji et al. prepared low temperature WO_3 by ultrasonic spray pyrolysis method of an aqueous solution of ammoniumtungestate ($(NH_4)_{10}W_{12}O_{41}$) precursor in air. A higher PCE of 3.63% was reached with spray pyrolsised WO_3 anode layer, compared to control devices based on vacuum thermally evaporated WO_3 [177]. Recently, ultra-thin WO_3 layers prepared by UVO-treatment of WO_3-octadecylamine was employed as blocking layers in dye sensitized solar cells (DSSCs). The efficiency of devices based on WO_3 films was improved to 21% compared to TiO_2 based devises. This enhancement is attributed to uniform morphology and proper position of Fermi level of WO_3 [178].

1.7.3 Vanadium pentaoxide (V_2O_5)

V_2O_5 is an n-type semiconducting oxide, exhibiting remarkably deep-lying electronic states with band gap ~ 2.80 eV, and high work function of -5.60 eV. V_2O_5 was employed as an optical spacer for improving light harvesting, and to prevent the diffusion of hot metal ions into the active layer [135].

Benmoussa et al. demonstrated sol–gel route to prepare VO_x, the gel was prepared by dissolving V_2O_5 powder in hydrogen peroxide then thermally annealed at 150 °C [179]. Later, solution-processed V_2O_5 was reported by Huang et al. through dispersing V_2O_5

nanoparticles powder into isopropanol (IPA) by ultrasonic agitation or wet grinding [180, 176]. Afterwards, Zilberberg et al. reported another solution processed V_2O_5 with a high WF of 5.60 eV, via the ambient hydrolysis of Vanadium(V) oxitriisopropoxide precursor dissolved in isopropyl alcohol (IPA) at room temperature without any post-treatment. The V_2O_5 film was stored in ambient air for 4 hours, after spin-coated from the precursor, for complete hydrolysis which can be shortened by thermal annealing at the suitable temperature [135]. The electronic band structure of the resultant V_2O_5 film was similar to that of the thermally evaporated V_2O_5, optical bandgap of 2.30 eV, and an ultra-smooth surface with RMS of 0.4 nm were obtained. The fabricated V_2O_5 film exhibited excellent hole transport characteristics in both conventional and inverted architectures and was able to maintain 80% of the initial PCE value for 400 hours, while devices used PEDOT:PSS as HTL failed [135, 181].

Meanwhile, Tan *et al.* synthetized VO_x film with high transmittance in visible region, smooth surface (RMS = 2.4 nm), and high hole mobility of 6.9 x 10^{-3} cm^2 V^{-1} s^{-1}, based on the decomposition of vanadyl acetylacetonate ($VO(acac)_2$) in isopropanol solution (1.5 mg ml^{-1}) by thermal treatment at 150 °C for 10 minutes [182]. The resultant VO_x anode layer contributed to an improved fill factor by decreasing the series resistance and increasing the shunt resistance of the whole device. Subsequently, an enhanced J_{SC}, high FF > 70%, and PCE of 6.35% were obtained for OPVs based on P3HT:ICBA with solution-processed V_2O_5 as HTL compared to that of PEDOT:PSS devices [182].

Afterwards, Xie et al. fabricated solution-processed V_2O_5 of large bandgap 2.70 eV and work function of 5.50 eV, at low-temperature < 100 °C from hydrogen vanadium oxide bronze (HxV_2O_5), which obtained from the oxidation of vanadium powder with H_2O_2 in ethanol solution. OPVs with solution-processed V_2O_5 as HTL exhibited higher PCE (7.6%) than a device using PEDOT:PSS HTL (7.2%). However, its high optical absorption in the visible range (400–500 nm) limits its application as an efficient HTL [160].

Escobar et al. obtained low temperature solution processed V_2O_5 from an aqueous solution of sodium metavanadate ($NaVO_3$). The V_2O_5 hydrate gel first obtained by cation-exchange from the aqueous solution of $NaVO_3$ to metavanadic acid (HVO_3). Then the dehydration process was carried out at 120 °C for 5 minutes which forms a film of $V_2O_5.nH_2O$ on the

substrate. OPVs employed this V_2O_5 as HTLs for both conventional and inverted device architectures exhibited long outdoor stability due to containing of water molecules in the layer structure below 250 °C [183].

Afterwards, Rafique et al. synthesized V_2O_5 nanoparticles (NPs) via hydrothermal method then dispersed NPs in PEDOT:PSS layer forming hybrid HTL. When the hybrid HTL was employed in BHJ OPVs based on PCDTBT:$PC_{71}BM$, the device degradation was decreased and lifetime was significantly improved compared to pristine PEDOT:PSS due to its better optical properties [184]. Jiang et al. prepared $V_2O_5.H_2O$ layer via sol –gel method from low cost V_2O_5 powder. A PCE of 5.87% was achieved by using $V_2O_5.H_2O$ HTL in BHJ OPV based on PBDSe-DT2PyT:$PC_{71}BM$ which is 30% higher than that of PEDOT:PSS (4.55%). This increase in PCE was attributed to the efficient electron blocking at anode and high optical transmittance in wavelength range of 400-500 nm which improves the charge generation and surpass the charge recombination within active layer [185, 186].

Although the excellent hole extraction at the V_2O_5/BHJ interface, the high toxicity of V_2O_5 limits its applications in solution process device fabrication in ambient atmosphere [187].

1.7.4 Chromium oxide (Cr_2O_3)

Cr_2O_3 is n-type semiconductor oxide and an earth abundant. It is stable to light and air exposure, as well as to thermal annealing at high temperatures and can be processed from many solvents such as water and alcohols. However, it is rarely used as interlayer in OPV [188, 189].

Li et al. reported a simple synthetic route for solution processed p-type CrO_x by spin coating of chromium acetylacetonate ($Cr(acac)_3$) precursor then thermally annealed at 60 °C followed by UVO-treatment as can be seen in **Figure 1.21**. The PCE of a P3HT:$IC_{60}BA$ BHJ device was enhanced to 6.55% based on CrO_x HTL compared to 6.06% for PEDOT:PSS based device. This enhancement was attributed to the hydration of CrO_x during the UVO- treatment in air which forms dipolar species $Cr(OH)_3$ in the buffer layer. These species increased the work function forming of an Ohmic contact at the anode/BHJ and improved the device performance [190].

1.7.5 Ruthenium oxide (RuO_2)

Li et al. obtained solution processed RuO_2 by direct UVO-treatment of as-deposited Ruthenium(III) acetylacetonate ($Ru(acac)_3$) precursor for 10 min. Most of $Ru(III)(acac)_3$ will decompose and the resultant film will be mainly RuO_2 as shown in **Figure 1.21**. When RuO_2 was employed as a hole transport layer, it enhances PCE of the PBDTBDD:$PC_{71}BM$ BHJ device to 7.45% which is higher than that of PEDOT:PSS. This enhancement was attributed to the high light transmittance of RuO_2 which improved J_{SC}. [191].

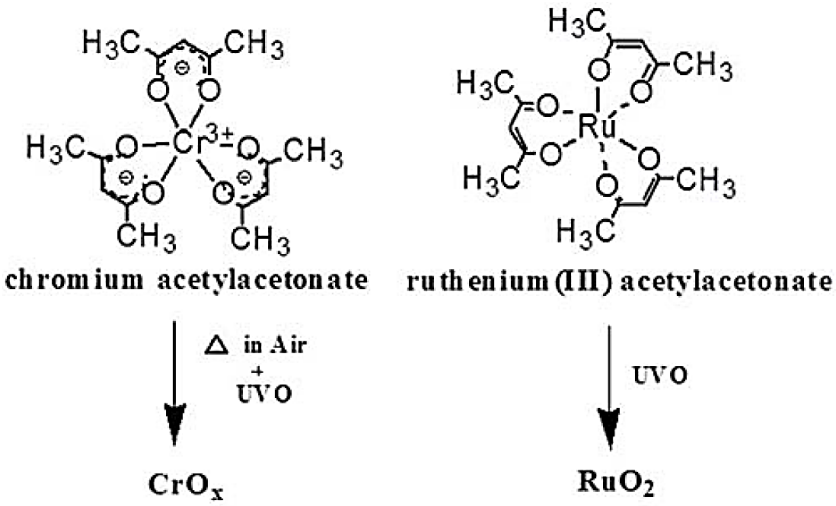

Figure 1.21 The solution processes used to prepare CrO_x and RuO_2, taken from [83, 62].

1.7.6 Rhenium oxide (ReO_3)

ReO_3 is a unique metal oxide with a high work function (6.0 eV) and low vacuum-evaporation temperature (340 °C). In addition to the good hole- collection efficiency of ReO_x, it enhances the light distribution within the bulk heterojunction layer and then enhance the light absorption due to the better-matched refractive index [192].

A solution-processed ReO_x was prepared from methyltrioxorhenium(VII) (CH_3ReO_3, i.e. MTO) precursor dissolved in isopropanol. The as-deposited film was stored in ambient air for 25 min for polymerization in which MTO was gradually converted into organometallic oxide polymeric MTO ($[CH_3ReO_3]_n$, i.e. poly-MTO) as a result of reacting with moisture. Subsequently, the film was thermally annealed at 110 °C to remove the unpolymerized

MTO. Finally, UVO-treatment in air was carried out to decompose the poly-MTO into ReO_x [193].

The PCEs of 7.26% and 8.30% was achieved for P3HT:$IC_{60}BA$ and PBDTTT-C-T:$PC_{71}BM$ BHJ conventional devices respectively based on ReO_x as HTL which were improved by 14% compared to PEDOT:PSS-based device. The enhancement of PCEs mainly arises from the additional light absorption within the photoactive layer in the wavelength range of 400– 550 nm [193].

1.8 Motivation

One way to improve the performance and stability of OPVs is the inclusion of interlayers, which facilitate the transport of both electrons and holes to both electrodes. Zinc oxide is widely used electron transport layer (ETL) that has the advantage of good electrical properties and chemical stability. The most commonly used hole transporting material (HTL) is poly(3,4-ethylenedioxythiophene):polystyrene sulfonate (PEDOT:PSS), which has better electrical properties than the most of the alternatives, but its acidic and hydroscopic nature limits the durability of the OPV, so a replacement is needed.

Although the wide spread of the previously mentioned oxides in OPVs achieving reasonable efficiencies, the high toxicity of V_2O_5 and CrO_3 and the shortage of tungsten, make them not very appropriate for green and low cost OPVs processing in ambient conditions. Therefore, there is a vital need to develop nontoxic, abundant, and solution-processable hole transport layer for highly efficient OPVs.

n-type transition metal oxides such as MoO_3, V_2O_5, and WO_3 are extensively investigated as HTLs for various optoelectronic applications. Therefore, there is an increasing interest in obtaining p-type transition metal oxides such as copper oxides (CuO, Cu_2O) and nickel oxide (NiO) with high hole conductivity and processed via different fabrication techniques.

1.9 Thesis Outline

This thesis focuses on the development of high-performance OPVs based on p-type transition metal oxides as potential alternatives to PEDOT:PSS. The optoelectronic and hole transport properties of two metal oxides, Nickel oxide (NiO) and Copper oxide (CuO_x) are studied using various precursors and device characterization techniques. Notably, this research investigates TMOs as HTLs that are fabricated via different fabrication techniques such as thermal evaporation and solution process at low temperatures, which are favourable for large-area applications.

This chapter provides a discussion of the development of OPVs, the operating principle, and the importance of interlayers. Next, a comprehensive review of the literature on the current development of hole transport inorganic materials is presented and mainly focusing on transition metal oxides that formed the basis of this research. Following the introduction, Chapter 2 outlines the experimental steps employed in this study including the sample preparation procedures, material characterization techniques, and optoelectronic of device performance.

Chapters 3-5 present a detailed analysis of the results obtained in this research. Chapter 3 reports the development of vacuum sublimed NiO_x layers and their application as CTLs in organic photovoltaics (OPVs). Evaporated layers of NiO_x of varying tungsten content are incorporated into bulk heterojunction OPVs and compared against control cells based on other commonly used, CTLs. These experiments allowed to identify an optimum W:Ni ratio in the evaporated films for best device operation. Chapter 4 obtains the synthesis of CuO_x at low temperature via solution process of commonly used copper acetate precursor. The suitable HTL thickness and annealing temperature were recognized for comparable device performance. Chapter 5 describes the preparation of copper oxide (CuO_x) layer via a novel synthetic route at low temperature from copper ethoxide precursor. The fabricated CuO_x film has been successfully integrated as the hole-transporting layer (HTL) for OPVs. Finally, the Summary and key outcomes of this research project are concluded in chapter 6.

2 Fabrication and Characterization Techniques

2.1 Introduction

This chapter describes the fabrication methods employed to deposit TMOs and fabricate OPVs in this thesis and provides an overview of the working principles of various characterization techniques used to investigate the structural and optoelectronic properties of thin films. A brief discussion of each method is presented in this chapter. However, more details of all experiments are shown in the relevant chapters.

2.2 Substrate preparation

Thin films were deposited on indium tin oxide (ITO) coated glass substrates (Kintec Company, 10 Ω per square), quartz substrates, and silicon (Si) wafers with thermally-grown silicon dioxide (SiO_2) of (400 nm ± 5%) (Active Business Company GmbH). Prior to deposition of thin films, substrates were cleaned thoroughly by ultra-sonication in a sequence of solvents 10 min each to remove any surface contaminants. The sequence was as follows: sonication in de-ionized (DI) water with Decon-90 detergent followed by rinsing with DI water to remove the detergent from substrates, then sonication in pure DI water, acetone and isopropanol (IPA). The clean substrates were then dried by blowing nitrogen over substrate surface. For the final step, substrates were placed inside UV-ozone cleaner (UVOCS® model T0606E) for 15 min to remove any organic residuals from substrate surface, whilst also improving substrate surface energy for thin film depositions [194].

2.3 Thin film processing techniques

In this thesis, the thin film deposition process was carried out using either solution processing or thermal evaporation.

2.3.1 Thin film deposition via Spin Coating

In earlier studies, metal oxide films were prepared through vacuum deposition processes, which are very expensive and incompatible with the high throughput manufacturing processes. Therefore, vacuum-free techniques that can be carried out at room

temperature in the ambient atmosphere are needed for reducing the fabrication cost, ensuring compatibility with roll-to-roll processing techniques.

Spin coating is the most commonly used technique for the deposition of homogenous metal oxide films over large area substrates (30 cm) by the sol–gel method. Cost-effectiveness, low maintenance, and ease of operation are the major advantages of this technique. However, the large material losses (> 90 %) limit compatibility with roll- to-roll processing.

For spin coating process, a sufficient amount of solution is placed by using a pipette onto the substrate placed on the sample holder within the spin coater. The substrate is then rotated at a defined speed for a specified time in order to spread the solution uniformly over the surface due to the centrifugal force and surface tension. Subsequently, the film gets thinner due to solvent evaporation as shown in Figure 2.1. Alternatively, the solution may be applied while the substrate is spinning. The spin casting process is carried out either in a fume hood for aqueous solutions or inside nitrogen-filled glovebox for organic solutions [195].

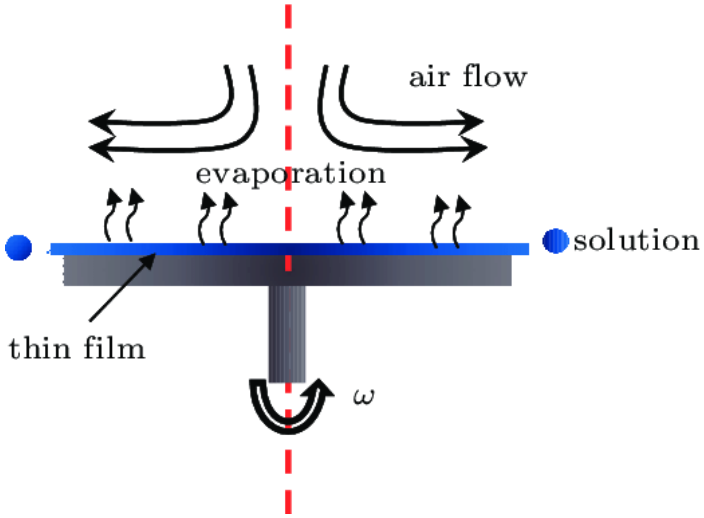

Figure 2.1 A schematic diagram describing the spin coating process, adapted from [196].

Post treatment such as thermal annealing is often carried out to the as- deposited film to remove the organic reside and solvents, which also improve the quality of the film and dry the coating. The film thickness and quality are controlled by the concentration of precursor and deposition conditions such as spin speed and time, and thus, these variables should be optimized to improve the device performance.

2.3.2 Thin film/metal contact deposition via Thermal evaporation

Thermal evaporation under high vacuum was used to deposit nickel oxide thin film and metal contacts onto substrates. This was carried out by using a Kurt J. Lesker Mini SPECTROS^{TM} evaporation system. Samples were loaded into a substrate holder, with shadow masks (made of thin steel sheets) placed on the substrate surface in order to acquire specific exposed regions. The sample holder was placed at the top of a vacuum chamber whilst metals or powders to be evaporated are loaded into a source crucible or boats held by a heating element at the bottom of the chamber as shown in **Figure 2.2**. The chamber is then pumped down to high vacuum ($\sim 5 \times 10^{-6}$ mbar) to be ready for metal deposition. Obtaining a high vacuum environment is important to prevent the oxidation process due to the presence of oxygen. Suitable voltages were then applied across the heating element, which slowly increases the electrical current (temperature) over a period of approximately 5 minutes to avoid damage to the crucible or the boat from thermal shock. The evaporation rate and the required thickness are monitored by the crystal sensor. Finally, the chamber was vented with nitrogen until it reaches the atmospheric pressure, then the samples can be removed from the chamber.

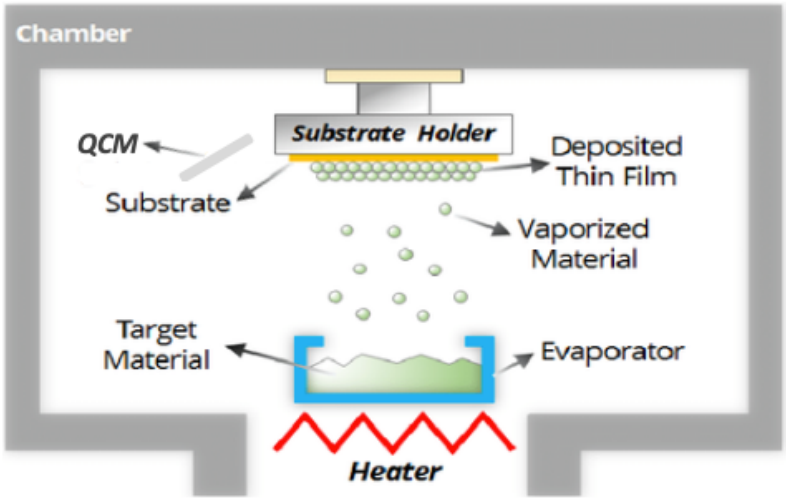

Figure 2.2 A schematic diagram of thermal evaporation deposition process, adapted from [197].

2.4 Thin film characterization of TMOs

Understanding how TMOs affect the interface properties, such as the energy level alignment at BHJ/anode interface, surface morphology, and optical transparency, is critical for further improvement in the performance of OPVs. X-ray photoelectron spectroscopy (XPS), X- ray diffraction (XRD), atomic force microscopy (AFM), and UV-VIS-NIR spectroscopy are essential techniques to study the optical and interface properties.

2.4.1 Compositional Identification

Owing to the chemical reactions at the surface of the metal oxides film, prepared by sol-gel process, a variety of surface components can be formed. Therefore, determination of the elemental and molecular composition is needed, to further understanding the relationship between the function and the composition of the interfacial layer.

2.4.1.1 X-ray Photoemission spectroscopy (XPS)

X-ray photoelectron spectroscopy (XPS) is used for analysing the surface components based on the photoelectric effect. When a material, placed in ultra-high vacuum, is irradiated with a high-energy X-ray beam, electrons are emitted from the material with a kinetic energy equal to the difference between the incident photon energy and the binding energy. The characteristic XPS peaks, at certain kinetic energies of the emitted electrons, can identify each element in the sample. Furthermore, the intensity of the characteristic peaks determines the percentage of every element. Therefore, quantitative analysis of the surface composition can be realized using XPS as shown in Figure 2.3.

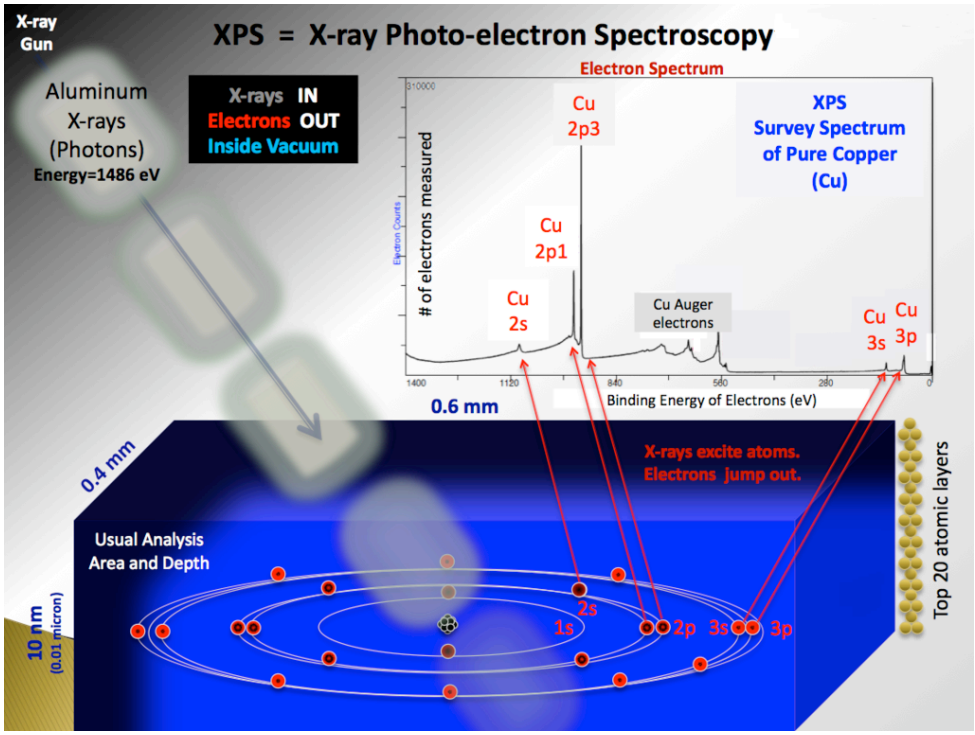

Figure 2.3 X-ray photoelectron spectroscopy working principles, adapted from [198].

For XPS measurements, metal oxides thin films were deposited on conductive ITO-glass substrates. The spectra were recorded on a Thermo Scientific K-Alpha+ spectrometer operating at a base pressure of $2x10^{-9}$ mbar. This system incorporates a monochromated Al Kα X-Ray source (Photon energy = 1486.60 eV) and a 180° double focusing hemispherical analyser with a 2D detector. The X-ray source was set to 72W, operated at 6 mA emission current and 12 kV anode bias. Data were acquired at 200 eV pass energy for survey scan, 20 eV pass energy for core level using an X-ray spot size of 400 μm^2. Samples were loaded using carbon conductive tape, and in addition a flood gun was applied to reduce sample charging. All spectra were aligned using the C 1s contribution of adventitious carbon. All data were analysed using the Avantage software package [86].

2.4.1.2 X-ray diffraction (XRD)

XRD is a structural characterization technique, used to identify the crystal structure of the sample. When the specimen is exposed to X-rays beam of a wavelength comparable to the interspacing between the atoms, the crystalline atoms and planes will diffract the incident beam in many directions at different angles yielding peaks of different intensities. The

interspacing (d) between atoms can be measured by Bragg's law; n λ = 2d sinθ, where n, λ, and θ are an integer number, wavelength of the incident beam, and the diffraction angle respectively as shown in Figure 2.4.

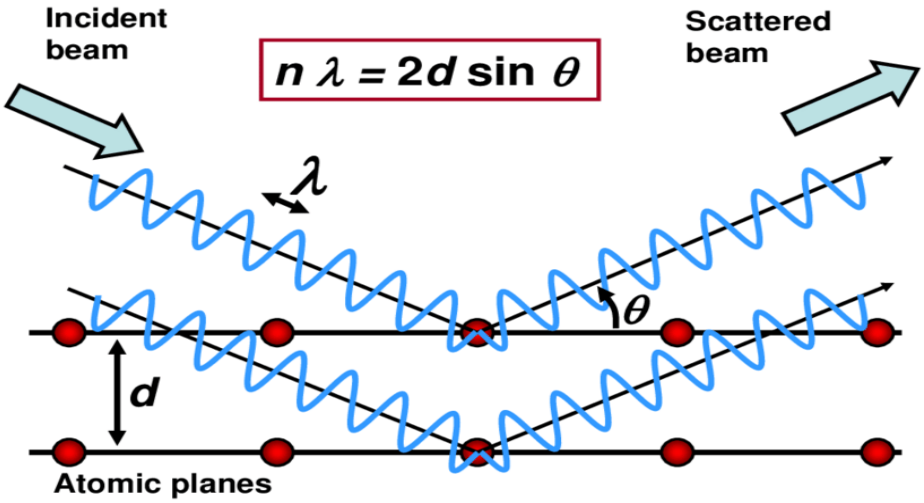

Figure 2.4 X-ray diffraction working principle (Bragg's law), adapted from [199].

The structure of TMOs thin films was determined using a PANalytical X'Pert Pro diffractometer at an accelerating voltage 40 KV and a filament current of 40 mA. The system produces Cu K_α radiation at a wavelength of 1.54 Å. The diffraction patterns were analysed using Highscore software.

2.4.2 Morphological characterization

2.4.2.1 Atomic force microscopy (AFM)

Atomic force microscopy (AFM) is a very high-resolution type of scanning probe microscopy, used to study the morphology of thin films. There are different imaging modes of AFM such as contact, non-contact and tapping modes. The most commonly used mode is the tapping (AC) mode, which involves probing the sample surface with a nano-scale tip attached to a vibrating cantilever at its resonance frequency. This vibrating frequency and amplitude can be changed due to the interactions between the tip and the surface via van der Waals forces. The variation in the amplitude of the tip gives the topography of the surface as shown in Figure 2.5.

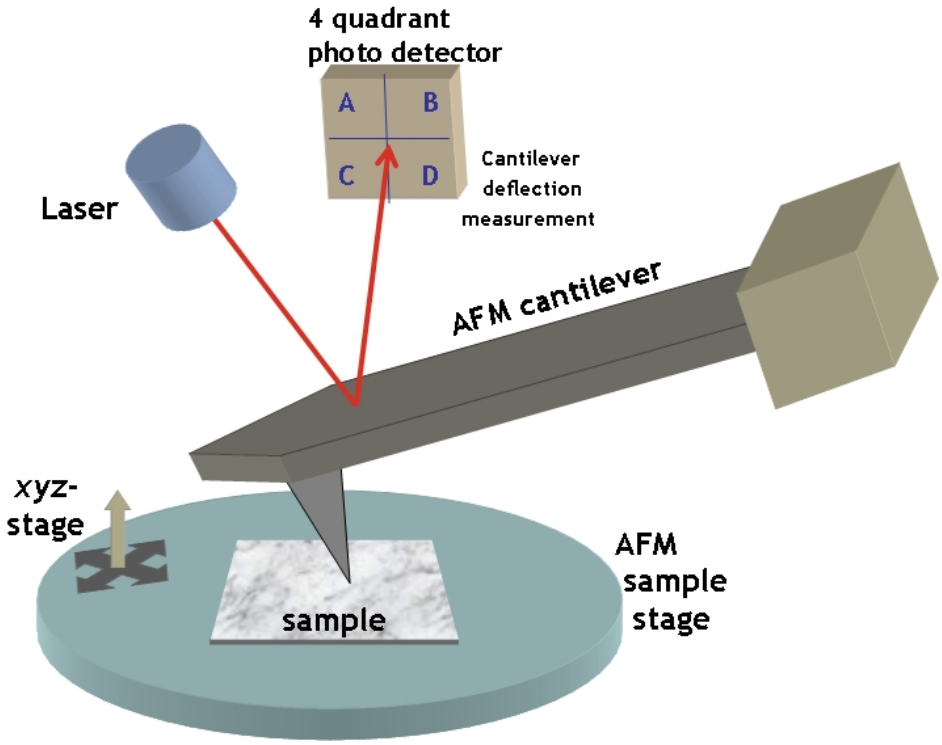

Figure 2.5 A schematic diagram describing the working principle of AFM, adapted from [200].

The surface morphology of thin films deposited on ITO substrates were studied using tapping-mode AFM using an Agilent 5500AFM system, which employed a cantilever with frequency ~ 270 KHz and a force constant 40 N m^{-1}. Topography and phase images are recorded using PicoView scanning probe microscopy control software. Information on material crystallinity, grain size, and thin-film uniformity were determined using Gwyddion software; all surface height data were extracted from AFM topography images at an identical resolution in order to generate representative distributions using Origin software [86].

2.4.2.2 Scanning electron microscope (SEM)

SEM is an imaging technique used to obtain the surface topography and composition. SEM is scanning the surface by a focused beam of electrons, which interact with the sample, yielding a variety of signals, including secondary and back-scattered electrons. The resulting

electrons are detected at different angles and their intensities will display the topography of the surface.

A Leo Gemini 1525 Field Emission Scanning Electron Microscope (FESEM) was used with accelerating voltage of 5 kV. The field emission gun and the sample chamber were held at high vacuum during imaging, ~ 10^{-7} Pa and ~10^{-3} Pa respectively. First, the samples were coated by thin layer of 5 nm chromium by sputtering in order to increase surface conductivity for better image quality. To reduce the electron charging effect under electron beam irradiation, the edge of the substrate surface was coated by conductive carbon tape that the other side was connected to the aluminium sample holder. For imaging, in-lens detector was used to record Secondary electrons (SE), which are produced within only several nanometres of the sample surface, with typical energies < 50 eV. All data were analysed using ImageJ program.

2.4.3 Optoelectronic characterization

2.4.3.1 Ultraviolet-Visible-near infrared Spectroscopy (UV-VIS-NIR)

UV-VIS-NIR spectroscopy is used to measure the optical properties of the thin film of TMOs such as transmittance, absorption coefficient, and optical band gap. When a monochromatic light in the range of UV-Vis-NIR is incident on the film, part of light is absorbed, other transmitted and the rest is reflected. Transmittance of the film is the relative intensities of the transmitted and incident light and it can be calculated from the Beer-Lambert law [201].

$$I = I_o\, e^{-ax}$$

The absorption coefficient α is given by

$$\alpha = \frac{1}{x} \ln \left(\frac{I_o}{I}\right)$$

Where I_o is the incident light intensity, I is the transmitted light intensity, and x is the film thickness.

The transmittance and reflectance spectra of TMOs films deposited on quartz substrates were measured in the 200 – 1400 nm wavelength range, using a Shimadzu UV-2600 spectrophotometer equipped with an ISR- 2600Plus integrating sphere. Then the absorbance was calculated from the transmittance and reflectance spectral data in order to determine the optical bandgap of the semiconductor using Tauc plot analysis.

Tauc plot is the relationship between $(\alpha h\nu)^n$ and $h\nu$, where α is the absorption coefficient, $h = 4.136\,x10^{-15}\ eV\ .s$, is Plank's constant, ν is the frequency of the incident light, and $n = 2$ for direct bandgap or ½ for indirect bandgap. The optical bandgap is determined by extrapolating the linear fitting of the curve to the energy axis as shown in Figure 2.6, according to the following equation$(\alpha h\nu) = A(h\nu - Eg)^{\frac{1}{n}}$, which gives the bandgap at$(\alpha h\nu)^2 = 0$.

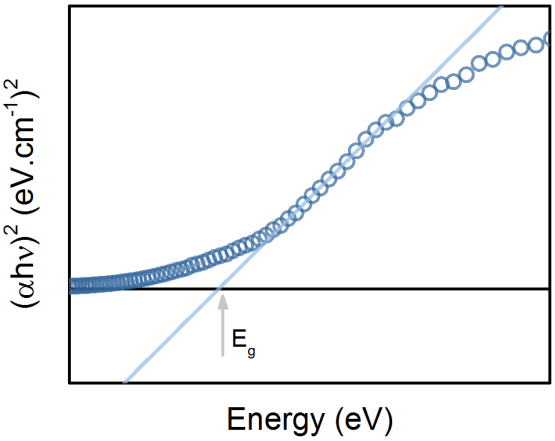

Figure 2.6 Tauc plot of $(\alpha h\nu)^n$ versus $h\nu$ illustrating the linear fitting of the curve to determine the bandgap at x-axis intercept, [Auther's own work].

2.4.3.2 Kelvin Probe Measurements

The Fermi level (E_f) and valence band maximum (VBM) of TMOs thin films were determined using Kelvin Probe (KP) contact potential difference measurements and Air Photoemission Spectroscopy (APS), respectively. Thin films of TMOs were deposited ITO coated glass substances.

The working principle of the Kelvin Probe is based on the concept of a vibrating capacitor to measure the work function of conducting materials or surface potentials of semiconductor surfaces in a non-contact manner. Due to the energy differences (i.e. work functions and Fermi levels) between the Kelvin Probe tip and the samples, when electrical contact is made, the equalisation of the Fermi levels results in the generation of electrical charges on the respective surfaces. Therefore, the ability to detect these charges allows the Kelvin Probe to determine surface potentials. During the measurement, the vibrating tip is typically at a distance of 0.2–2.0 mm away from the sample surface, and an electrical contact is connected to another part of the sample in order to form the vibrating capacitor.

Figure 2.7 Photograph showing Kelvin Probe-Air photoemission spectroscopy set-up, taken from [202].

The KP-APS set-up comprised of a KP Technology SKP5050 Scanning Kelvin Probe and an APS02 Air Photoemission System as shown in Figure 2.7. The contact potential difference of each semiconductor thin-film was measured relative to that of a silver reference sample, and hence, the Fermi level was calculated with respect to the work function of the reference metal, which was determined as 4.70 ± 0.05 eV using APS. The energy corresponding to the valence band edge was extracted from APS data, where each sample was exposed to ultraviolet radiation of wavelengths in the 200 – 300 nm range, and the photoemission signal from the layer surface was recorded as a function of wavelength. The oxygen level inside APS02 module is reduced by continuous flush of nitrogen during the operation of ultraviolet source to avoid ozone generation.

2.5 Solar Cell Fabrication and Characterization

Conventional and Inverted structures of OPVs were fabricated using TMOs as charge transport interlayers (CTLs). Thin films of TMOs such as NiO_x and CuO_x were thermally evaporated in vacuum or spin-coated on ITO-coated glass at different spin speed, and then annealed at various temperatures. The BHJ active layer blends were next deposited in inert atmosphere (nitrogen-filled glovebox) on top of the CTL layers, according to certain procedures discussed in the relevant chapters. After which the cells were completed by the thermal evaporation of a 10 nm thick layer of molybdenumtrioxide (MoO_3) followed by a 70 nm thick layer of silver electrode (Ag) for inverted OPVs or 10 nm of calcium (Ca) followed by 70 nm of aluminium (Al) for conventional OPVs. This evaporation process was carried out through shadow masks at a base pressure of 5×10^{-6} mbar.

The J-V characteristics of the solar cells were performed in a nitrogen-filled glovebox using a Keithley 2400 source meter. The AM1.5 illumination was provided by a Sciencetech Inc. Solar Simulator SF300-A, with an active area of 5 mm^2 defined by a metal stencil mask. The intensity of light is calibrated to 1 sun (100 mW cm^{-2}) with a KG- 5 silicon reference photodiode certified by Newport. The J-V curves are recorded using LabView software, and then Power conversion efficiency (PCE), open-circuit voltage (V_{OC}), short-circuit current density (J_{SC}), and fill factor (FF) were extracted. The datasets are analysed using Origin software and the series resistance (R_S) and shunt resistance (R_{Sh}) are estimated from the reciprocal of the slope of J-V curves when J=0 and V=0, respectively.

3 Thermally Evaporated Nickel Oxide as a Universal Electron Transport Layer

3.1 Introduction:

Interfacial layers such as transition metal oxides (TMOs) have significantly contributed to the improved performance and stability of organic photovoltaics. Therefore, significant research has been focused on developing and exploring new material precursors and recipes as well as novel processing techniques considering the improvement of the charge transport properties and ensure the compatibility with large area optoelectronic applications.

Nickel oxide (NiO_x) has attracted great attention in recent years for its potential as a charge transport layer (CTL) in various optoelectronic devices due to its high optical transparency, low-cost, and environmental stability. However, solution processing of NiO_x is still challenging as it is largely insoluble in most of common solvents and the inhomogeneity of the resulting NiO_x layers' surface morphology renders the applicability of such methods for large-area manufacturing. Therefore, thermal evaporation represents an attractive alternative as deposition of uniform layers with precise thickness control can easily be achieved over large areas.

This chapter reports the development of vacuum sublimed NiOx layers and their application as CTLs in organic photovoltaics (OPVs). First, optical characterization was carried out, then the optical bandgap was determined by Tauc analysis from absorbance and absorption coefficient calculations. Next, the Fermi level and the valence band maximum of evaporated films of varying thickness and tungsten content were obtained by Kelvin probe and air photoemission measurements. XPS helps to understand the tungsten presence in NiO_x films and its percentages in each sample. Evaporated layers of NiO_x of varying thickness are incorporated into bulk heterojunction OPVs and compared against control cells based on other, commonly used, CTLs such as ZnO. These experiments allowed to identify an optimum NiO_x film thickness and tungsten doping concentration for the comparable device operation. Our work demonstrates the potential of thermally evaporated NiO_x as efficient electron transport layers for organic photovoltaic devices.

3.2 Electronic Properties of Nickel oxide

Nickel (II) oxide (NiO) is the most widely studied p-type TMO, it forms an Ohmic contact (energy level alignment) with many donor materials in OPVs because its valence band (−5.0 eV) is well matched with HOMO levels of many polymers [130, 147]. Furthermore, NiO provides effective electron blocking ability because its conduction band (−1.70 eV) is higher than LUMOs of many organic donors and acceptors. Moreover, it has high transparency with wide band gap > 3.60 eV [130, 147]. Nickel oxide has cubic crystal structure as shown in Figure 3.1.

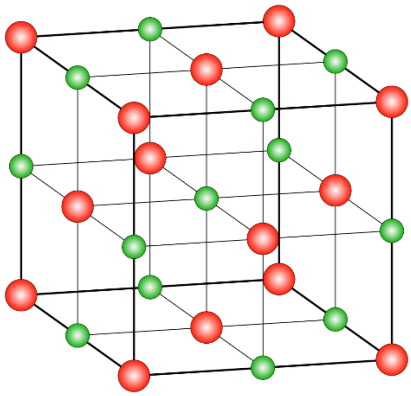

Figure 3.1 Crystal structure of NiO, where each nickel atom (green) is attached to six oxygen (red), adapted from [203].

The high work function of NiO (-5.0 eV) promotes an Ohmic contact at BHJ/anode interface [204]. However, the work function depends significantly on the deposition conditions, oxidation states, and surface chemistry. Therefore, the WF of NiO can be reduces when adsorbs surface contaminants (hydroxyl groups) or upon air exposure [205].

3.3 Review on Nickel oxide as a charge transport layer

Much research has been focused towards the development of solution processed NiO_x. Mashford et al. was first introduced NiO_X films via wet-chemical processing of nickel acetate tetrahydrate ($Ni(CHCOO)_2.4H_2O$) dissolved in methanol with diethanolamine then thermally annealed at high temperature 425 °C [206]. Another sol-gel NiO_x was introduced by Steirer et al. from ($[Ni(H_2N(CH_2)_2NH_2)_2](HCO_2)_2$) precursor and annealing at lower

temperatures 250–300 °C [129]. Afterwards, NiO_x was prepared from nickel formate dehydrate ($C_2H_8NiO_6$) dissolved in ethylene glycol containing ethylenediamine. PCE of 5.1% was achieved with NiO_x HTL compared with 2.3% for PEDOT:PSS control devices [207]. Next, Steirer et al. and Manders et al. reported the formation of NiO_x via thermal decomposition of nickel acetate tetrahydrate ($Ni(CH_3COO)_2.4H_2O$) precursor dissolved in ethanol and monoethanolamine (MEA) as stabilizer at 275 °C followed by O_2-plasma treatment which increased the work function from 4.80 eV to 5.30 eV [130, 208]. Afterwards, the processing temperature was further decreased to 150 °C by Zhai et al. via UVO-treatment to the same precursor [209]. Subsequently, Bai et al. utilized a combustion process to prepare NiO_x from nickel nitrate as oxidizer and glycine as a fuel, at 175°C to start the combustion reaction [210]. Annealing-free NiO_x was demonstrated by Zhang et al. from colloidal NiO NPs via sonochemical synthesis at low temperature through ultrasonic irradiation [211]. Jiang et al. prepared NiO_x (NPs) via the chemical precipitation reaction between $Ni(NO_3)_2{\cdot}6H_2O$ and NaOH without any post annealing [212]. Next, Lin et al. prepared NiO by two steps annealing process from nickel (II) acetylactenote dissolved in anhydrous ethanol with addition of small amount of HCL obtaining PCE of 19.04% for perovskites solar cells [213, 214]. NiO HTLs was demonstrated by Tang et al. via solvothermal method using well dispersed toluene solution of NiO nanocrystals (NCs). PCE of 15.47% for perovskites solar cells was realized which is higher than that of PEDOT:PSS (11.42%) [215, 216].

However, the difficultly in producing stoichiometric NiO in ambient air due to the complexity of the surface chemical reactions and non-uniform surface of the resulting NiO films limits the compatibility of such methods for large-area manufacturing. Thus, NiO was also processed by gas-phase methods such as chemical vapour deposition (CVD) [217, 218] and atomic layer deposition (ALD) [219, 220] in addition to physical processes such as pulsed laser deposition (PLD) [221], physical vapour deposition (PVD) [222], and magnetron sputtering [223, 224, 225].

Prior to embarking on the experimental work detailed in this chapter, the author experimented the processing of NiO from aqueous ammonia [NH3(aq)] solution. However, NiO is found to be largely insoluble in aqueous solutions which restricts the solution processing of NiO. Therefore, in this work, NiO is prepared by thermal evaporation which can achieve the deposition of uniform layers with precise thickness control over large areas.

3.4 Preparation of NiO_x Film by Thermal Evaporation

NiO_x was thermally evaporated on either cleaned quartz (for UV–Vis–NIR spectra measurements) or glass/ITO substrates (for AFM, Kelvin probe/APS measurements, and OPV device fabrication) using a Kurt J. Lesker evaporator. NiO powder (99.99%, Sigma-Aldrich) was evaporated from an alumina coated tungsten boat at a base pressure of 5×10^{-6} mbar. The deposition rate is maintained at 0.1 Å/s, and the NiO_x film thickness is measured by a quartz crystal microbalance, located 50 cm above the source and next to the substrates as shown in **Figure 3.2**.

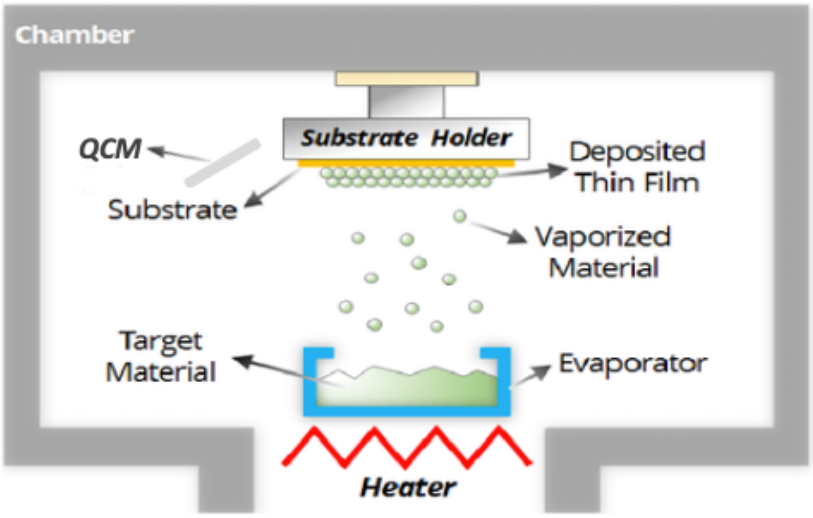

Figure 3.2 A schematic diagram of thermal evaporation deposition process, adapted from [197].

During the NiO evaporation process, the nickel oxide powder melts and alloys with the tungsten boat causing it to become brittle and crack shortly after exposure to nickel oxide liquid. Therefore, it is difficult to evaporate NiO powder using tungsten boat. There were two options to evaporate NiO avoiding cracking the tungsten boat. First option is to use alumina crucible. However, it depends on the external power heating so much more power is needed to raise the temperature to achieve a successful NiO film deposition. The second choice was to use alumina coated tungsten boat, in which alumina acts as an isolating layer between nickel and tungsten. Therefore, alumina coated tungsten boat was used in this work to evaporate NiO as shown in **Figure 3.3**. Three quarter inch dimpled boat coated with

alumina (EVS9BAOW) was used. A current up to 190 Amps can pass through this boat providing the required power (245 Watts) to reach the melting point of NiO (1955 °C) [226].

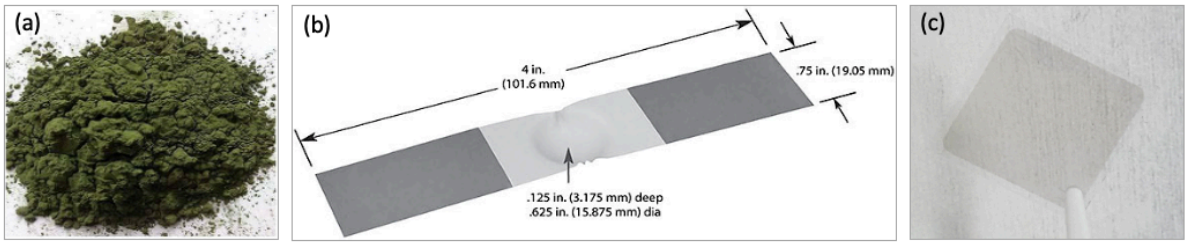

Figure 3.3 Photographs of (a) NiO powder, (b) alumina-coated tungsten boat employed adapted from Ref [226], and (c) 20 x 20 mm substrate with 10 nm NiO_x.

Thermal Evaporation of NiO films involves heating NiO powder, in the first ramp, to its melting point at some level just below vaporization to achieve an acceptable degree of equilibrium. Next, the second ramp set the actual power level close for the desired deposition rate and making it up to vaporization. Then the shutter opens and the deposition begins until the desired film thickness is achieved. The films thickness depends not only on the power but also on time of deposition. As the rate of deposition 0.1 Å/s was used so 8.5, 11.5, 16.5, and 33.5 min were required to achieve films of thickness 5, 7, 10, 20 nm respectively. At the end, the shutter closes and a cool down profile similar to the heat up one is applied.

3.5 Characterization of thermally evaporated NiO_x

3.5.1 Optical characterization

Following to the successful optimization of thermal evaporation parameters, uniform darkish layers of NiO_x were obtained on quartz substrates as shown in figure 3.3 (c). The UV-Vis-NIR transmittance and reflectance spectra of the evaporated NiO_x films were measured in 200–1200 nm wavelength range as a function of the deposition thicknesses (5, 7, 10, 20 nm), against an air reference as shown in Figure 3.4 (a). Subsequently, the absorbance and absorption coefficient were calculated from the transmittance and reflectance spectral data in order to determine the optical bandgap of the NiO_x semiconductor using Tauc analysis.

For different thickness films, high transmittance was obtained in the visible-NIR region, with an average transmission of ~ 86% in the wavelength range 350 to 1200 nm, with an absorption peak at ~ 200 nm as shown in **Figure 3.4**. It is also noted that the film of thickness 20 nm varied considerably from the other samples with lower transmission of average ~50% and higher absorption ~30% in the UV range. The reflectance is also affected by film thickness variation. The spectra for different film thickness show ~7- 9% reflectance over visible region and higher reflectance ~10-20% over UV wavelength range.

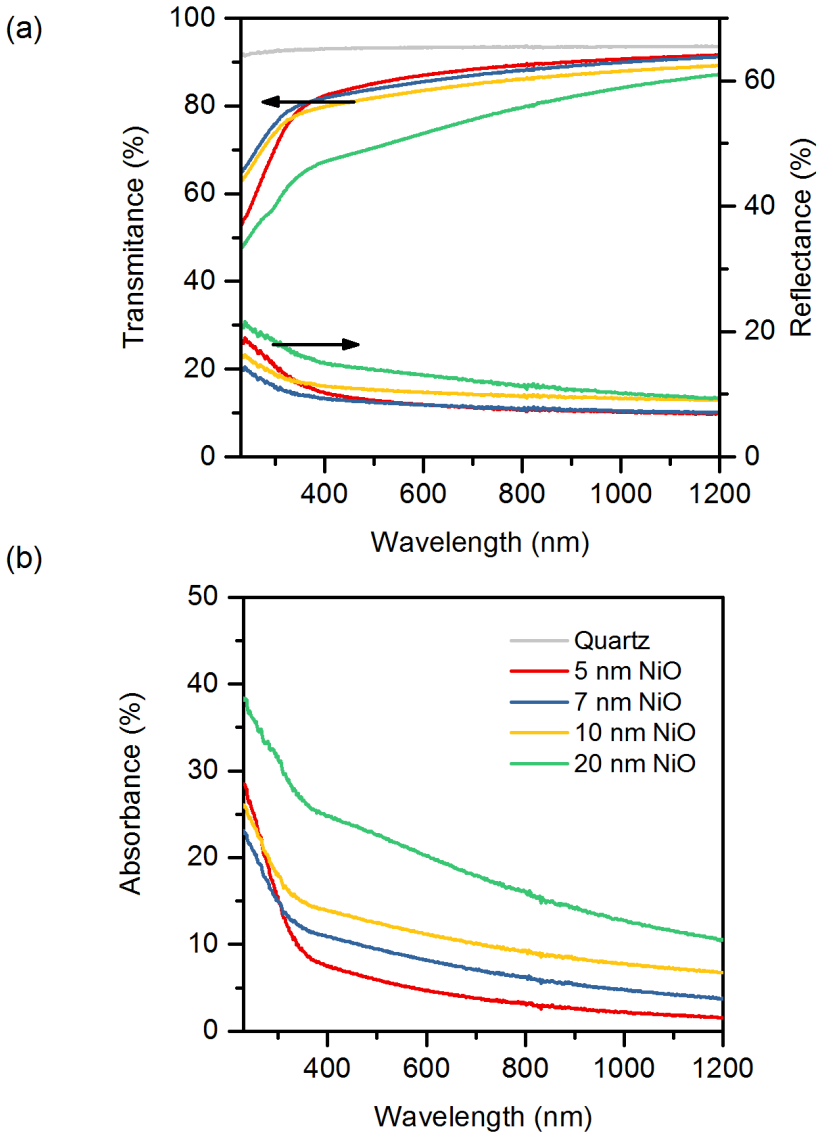

Figure 3.4 (a) Transmittance and reflectance spectra of the films with different thickness show high optical transparency, (b) UV-Vis-NIR Absorbance spectra of the deposited films on quartz substrates.

The optical bandgap (E_g) of thermally evaporated NiO_x of different thickness were determined from the Tauc analysis as shown in **Figure 3.5**. $(\alpha h\nu)^2$ is calculated using the transmittance and reflectance data of and plotted versus incident photon energy $(h\nu)$. E_g was found to be approximately 3.91, 3.80, 3.68, and 3.43 eV for NiO_x films of thickness 5, 7, 10, 20 nm respectively. These results show that thermally evaporated NiO_x has a wide bandgap. The calculated bandgap for 10 nm (3.68 eV) is in good agreement with the bandgap value of NiO_x in literature (3.60 eV) while the bandgap values for 5, 7 and 20 nm are different from the literature E_g value of NiO_x [130].

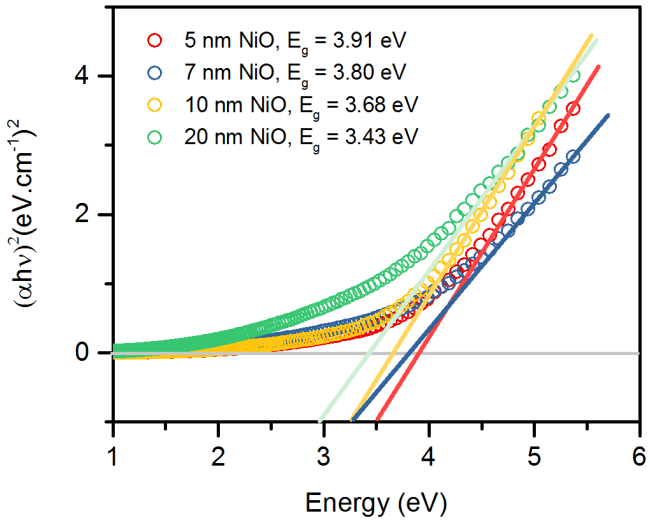

Figure 3.5 Tauc plots of thermally evaporated NiO_x of different thickness. $(\alpha h\nu)^2$ is calculated from the absorbance spectra of the deposited films on quartz.

3.5.2 Electronic characterization

The Fermi level (E_F) and valence band maximum (VBM) of thermally evaporated NiO_x films of different thickness were determined using Kelvin Probe measurements (KP) and Air Photoemission Spectroscopy (APS) respectively as shown in **Figure 3.6**.

It is necessary to determine the Fermi level and valence band maximum in order to explore the alignment of energy levels of evaporated NiO_x with the work function of electrodes and the highest occupied molecular orbital (HOMO) and the lowest occupied molecular orbital (LUMO) active layer materials.

The Fermi level (E_F) was calculated with respect to the work function of the reference metal (silver). The Fermi level E_F of thermally evaporated NiO_x ranges from 3.80 eV to 4.10 ± 0.02 eV and was found to be dependent on the thin film thickness. For APS measurements, the APS signals were recorded from NiO_x films deposited on fully covered ITO-glass substrates, then the spectra were analysed to estimate the valence band maximum (VBM). By measuring different sets of NiO_x films of various thickness, the VBM was found to be 4.20, 4.30, 4.10, and 4.00 ± 0.05 eV for 5, 7, 10, and 20 nm respectively. The VBM was found to be 0.20 eV below the Fermi level which is in good agreement with the literature and indicates the p-type nature of evaporated NiO_x films. Notably, there was a slight change in the E_F and VBM values of NiO_x layers about ± 0.01 eV after 2 weeks of air exposure (data not shown). This result verifies the chemical stability of thermally evaporated NiO_x films.

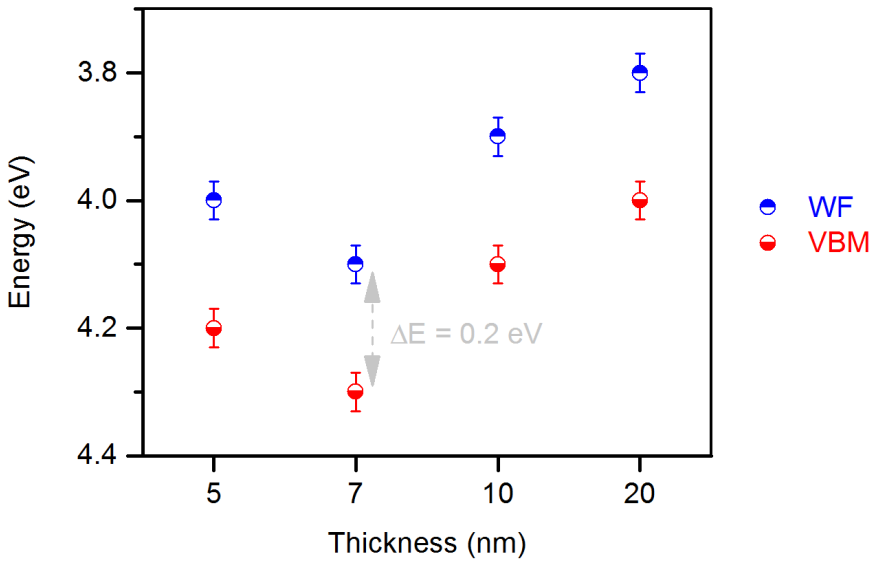

Figure 3.6 The work function (WF) and valence band maximum of evaporated NiOx films of different thickness (5, 7, 10, and 20 nm) deposited on ITO substrates.

It is clearly noted that the measured E_F and VBM values are smaller than that of NiO in literature (4.80 and 5.0 eV) [130] by 1 eV. This difference in energetics values between experimental and literature NiO highlights the potential of thermally evaporated NiO_x to be employed as electron transport layer (ETL) rather than hole transport layer (HTL).

Table 3.1 Summary of the optical and electronic characteristics of thermally evaporated NiO_x of different thickness.

Thickness (nm)	Bandgap (eV)	Fermi level (eV)	Valance band (eV)
5	3.91	4.00	4.20
7	3.80	4.10	4.30
10	3.68	3.90	4.10
20	3.43	3.80	4.00

By knowing 1) VBM which is in the range 4.10 - 4.30 eV, 2) optical band gap E_g which is in the range 3.40 - 4.25 eV, and 3) E_F estimated in the range 3.90 - 4.10 eV as lying ~ 0.20 eV above VBM (data summarised in **Table 3.1** . The energy levels diagram of thermally evaporated NiO_x can be constructed as shown in **Figure 3.7**.

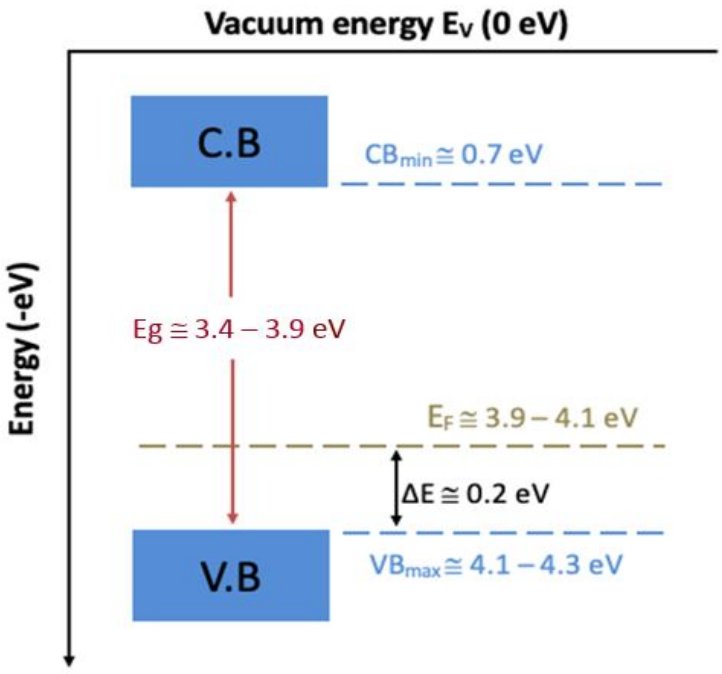

Figure 3.7 A schematic diagram of electronic energy levels of thermally evaporated NiO_x including VBM which is in the range 4.10-4.30 eV extracted from Air photoemission spectroscopy (APS), optical band gap Eg which is in the range 3.40-4.25 eV obtained from optical measurements, and E_F was estimated in the range 3.90-4.10 eV as lying ~ 0.20 eV above VBM using Kelvin probe measurements. Conduction band minimum (CBM) is also indicated.

3.6 Application of thermally evaporated NiO_x in OPVs

Firstly, the compatibility of thermally evaporated NiO_x films as hole transport layers (HTLs) was studied by incorporating them in a conventional structure of OPVs based on P3HT:ICBA as an active layer. However, OPV devices were shunted and did not work in the conventional structure in which the thermally evaporated NiO_x employed as HTL. After probing the electronic structure of these films, it was found that they have low work function approximately 4.0 eV as shown in Figure 3.7, which could match well with LUMOs of most acceptors. Therefore, in the following section, thermally evaporated NiO_x was utilized as ETL.

3.6.1 OPV device fabrication

Organic solar cells were fabricated in an inverted structure using evaporated NiO_x and solution processed ZnO as ETLs. For ZnO, zinc acetate (99.99%, Sigma-Aldrich) was dissolved in 2-methoxyethanol (anhydrous, 99.8%, Sigma- Aldrich) containing 3% ethanolamine (99.5%, Sigma-Aldrich), and was subsequently spin-cast on pre-cleaned ITO-coated glass substrates (see section 2.2) at 3000 rpm and then annealed at 180 °C for 20 min in air. The BHJ active layer blends were next deposited in the glovebox on top of ETLs according to the following procedures: 1) a commonly used P3HT:ICBA blend system (1:0.7 weight ratio) was spin coated at 1000 rpm for 1 minute from a 20 mg mL^{-1} chlorobenzene solution. 2) As-deposited films were then annealed at 150 °C for 10 minutes resulting in a film thickness of ~ 90 nm. 3) After which the cells were completed by the thermal evaporation of a 10 nm thick layer of molybdenum trioxide (MoO_3, 99.97%, Sigma-Aldrich) 4) followed by a 70 nm thick layer of silver electrode, through shadow masks at a base pressure of 5×10^{-6} mbar. The device active area was defined by a metal stencil mask (5 mm^2). Figure 3.8 displays the schematic structure of the BHJ solar cell, the energy levels of the relevant used materials, and the chemical structures of P3HT and ICBA [227].

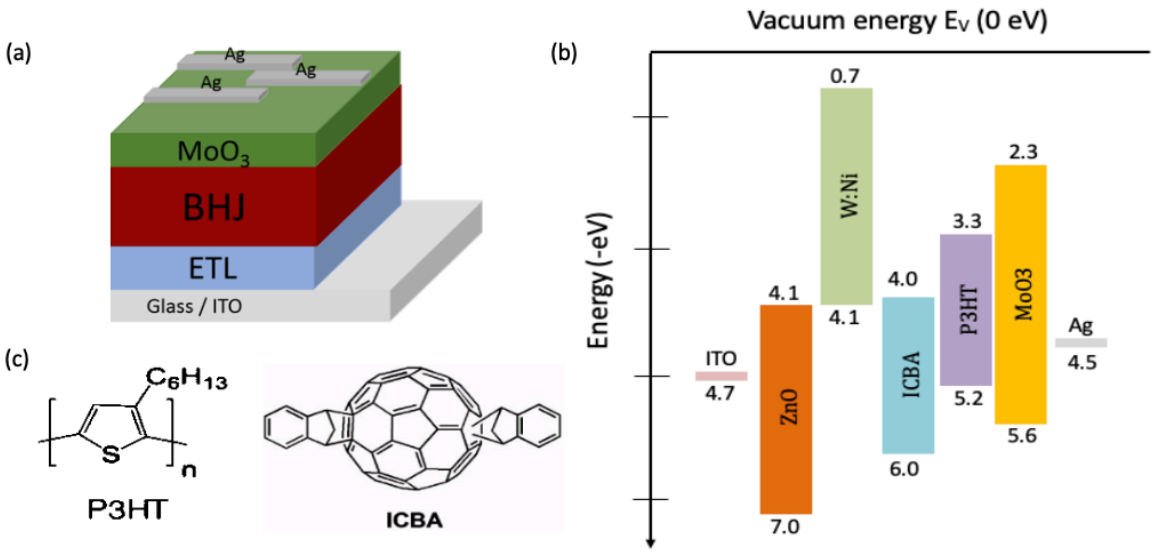

Figure 3.8 Fabrication of organic solar cells with NiO_x and ZnO ETLS, (a) Schematic of inverted BHJ solar cell employed, (b) Energetics of the different materials used, (c) Chemical structures of the active layer components P3HT and ICBA.

3.6.2 OPV device characterization

The J–V characteristics of the solar cells were performed under AM 1.5G illumination as shown in **Figure 3.9**, and the measured device parameters are summarized in **Figure 3.10**.

It is clearly seen from J-V characteristics that the thickness variation of evaporated NiO_x films (5, 7, 10, 20 nm) significantly influences the device performance. The open circuit voltage (V_{OC}), Fill factor (FF), and short circuit current (J_{SC}) were enhanced from 0.38 to 0.72 V, 0.39 to 0.46, and 7.87 to 8.63 mA cm^{-2} respectively as the thickness increased from 5 to 10 nm. The power conversion efficiency (PCE) increase significantly from 1.18 to 2.86 ± 0.05% for thickness 5 to 10 nm. This increase could be attributed to the increase in shunt resistance (R_{sh}) which reduces the leakage current and charge recombination so increases the electron transport at ETL/BHJ interface. This also could be ascribed to the decrease in series resistance (R_s) which may originate from the favourable energy level alignment of evaporated NiO_x ETL with the active layer due to the well matching work function of evaporated films with the LUMO of ICBA acceptor.

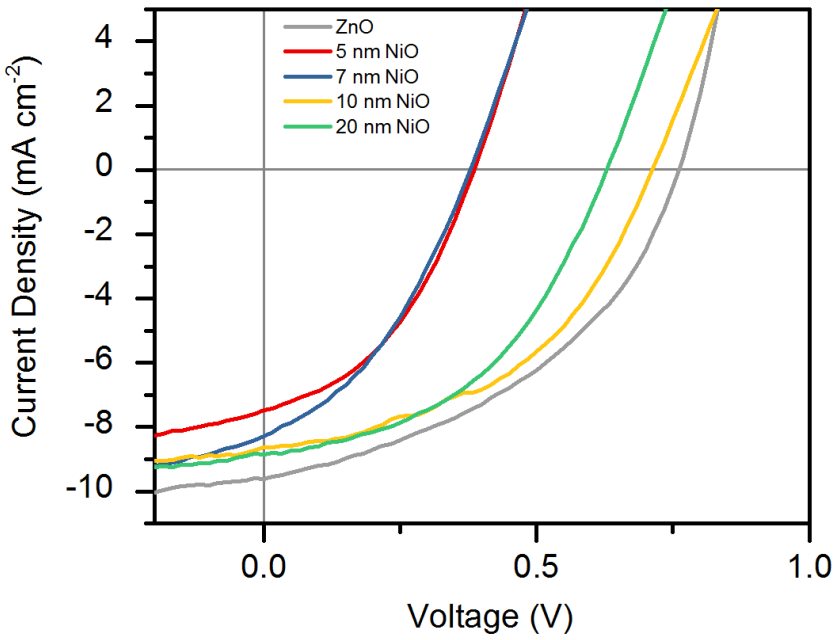

Figure 3.9 J-V curves measured under simulated AM1.5G illumination for inverted P3HT:ICBA OPV cells based on ZnO as a reference and thermally evaporated NiO_x of different thickness (5, 7, 10, 20 nm).

However, when the film thickness increases to 20 nm, the device characteristics showed lower values than that of 10 nm film. This decrease could result from lower transmission of average ~ 50% and higher absorption ~ 30% in the UV range. In addition to the higher series resistance (R_s) and lower shunt resistance (R_{sh}) of the thicker film as shown in **Figure 3.10**.

In brief, the optimum thickness of the evaporated NiO_x buffer layers was found to be 10 nm. The characteristics of device with the optimum ETL thickness showed PCE of 2.86 ± 0.05% with V_{OC} of 0.72 V, J_{SC} of 8.63 mA cm^{-2} and FF of 0.46. However, OPVs with ZnO ETL exhibited PCE of 3.29 ± 0.05% with V_{OC} of 0.77 V, J_{SC} of 10.3 mA cm^{-2} and FF of 0.43. The increase in J_{SC} and V_{OC} could be attributed to better energy level alignment of ZnO with the active layer than that of evaporated film which improve the contact at ETL/BHJ interface. However, the decrease in FF could result from the difference in processing methods as ZnO was solution processed and NiO_x was thermally evaporated. This indicates that uniform layers with precise thickness were achieved by thermal evaporation.

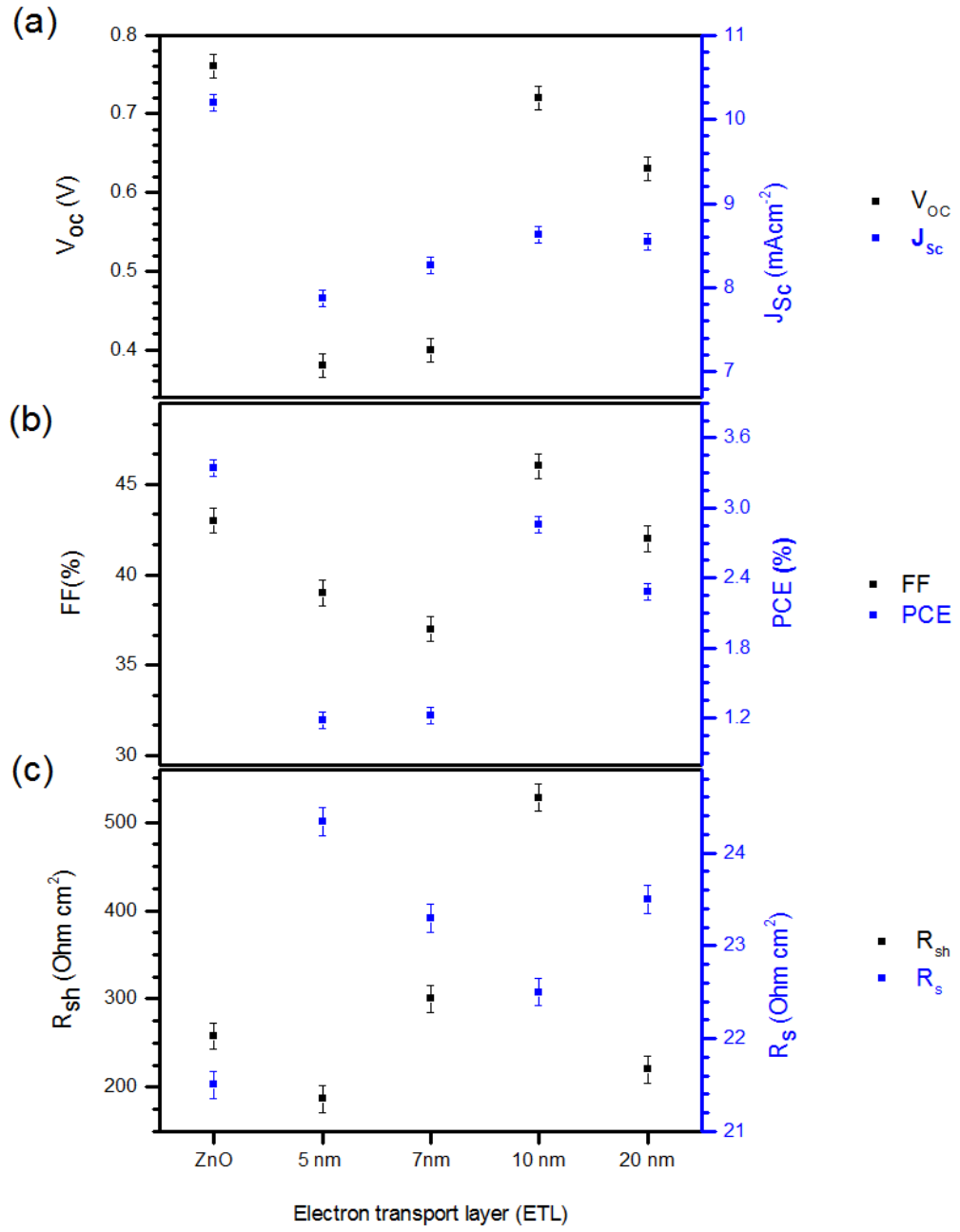

Figure 3.10 Measured device characteristics for P3HT:ICBA based devices fabricated with ZnO and different thickness of evaporated NiO_x as ETLs, measured under AM1.5 simulated solar illumination. (a) Open circuit voltage (V_{OC}) and short circuit current density (J_{SC}), (b) Fill factor (FF) and power conversion efficiency (PCE), (c) Shunt resistance (R_{sh}) and series resistance (R_s).

3.7 Microstructural analysis of evaporated NiO_x thin Films

X-ray photoemission spectroscopy (XPS) measurements were carried out for NiO_x films in order to investigate the elemental composition and to understand the reasons of n-type nature of the evaporated films. **Figure 3.11** shows the XPS survey spectra of a series of evaporated NiO_x samples, deposited with the same thickness (10 nm). Unexpectedly, dominating peaks of tungsten (W) were found across the survey spectra. This was ascribed to the alloying between the Ni and W-boat during evaporation. Although alumina coated tungsten boat was used, alumina did not avoid this alloying effect, but it prevented the boat's cracking during the evaporation. Therefore, the existence of W-peaks explains the n-type nature of the evaporated films.

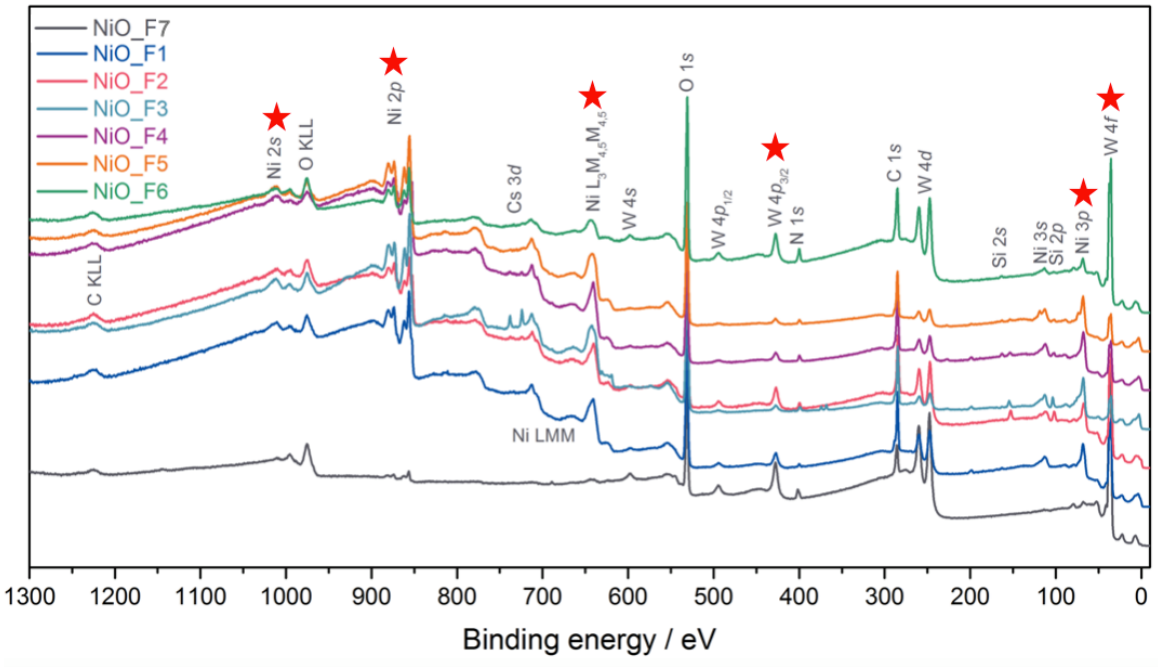

Figure 3.11 Survey spectra of different films of 10 nm NiO_x indicating core levels and Auger lines. The lines marked with an asterisk are major Ni Auger lines indicate the presence of W with different concentrations.

A survey spectrum scans the energy range of interest, in this study 0 – 1300 eV. The sharp peaks in the electron signal correspond to the elastic scattering of electrons. Inelastic scattering tends to produce broad peaks, and indeed the background. Notably the background level is significant higher at the higher binding energy. This is due to the fact

that the energy of electrons is lost as a result of inelastic scattering, leading to less kinetic energy recorded at the spectrometer. As previously introduced, binding energy proceeds in the opposite direction to kinetic energy. Hence the decrease in kinetic energy is typically presented as an increase binding energy, which explains the rising background level at high binding energy.

The dominating elements in the samples are indicated above the corresponding peaks. All samples were deposited on SiO_2 substrate, which contribute to the peaks of Si and O. Ni and W both showed dominating peaks across the survey spectra. The peak intensity depends on the number of atoms per unit volume, as well as the probability of electrons undergoing elastic scattering and escaping from the sample surface (cross section of the element). The ratio between nickel and tungsten is calculated from the area of Ni $3p_{3/2}$ and W $4f_{7/2}$, adjusting for the cross section of Ni and W. Although all sample were deposited under the same evaporation conditions and thickness, different W:Ni ratios were determined, uncontrolled, as shown in Table 3.2. The second evaporation tends to result in higher W content than the first evaporation from fresh boat, for example, sample number 2, 6, and 7.

Table 3.2 Estimated Ni:W ratio on evaporated NiO_x sample surface (with an error of up to 5%), all samples are 10 nm thickness.

Sample	Ni:W
1	80:20
2	56:44
3	90:10
4	76:24
5	87:13
6	44:56
7	09:91

As shown in **Table 3.2**, a wide range of Ni:W ratio was achieved. Atomic ratio Ni:W of 80:20 was selected to investigate in further details. **Figure 3.12** shows the C 1s of the resulting film, in comparison with a nickel oxide (NiO) reference sample (99.8% Sigma Aldrich) as originally intended [238]. C 1s is typically used for charge correction, in which the C-C peak is assumed a constant position of 284.8 eV. Charging occurs when the electron vacancies (left by the ejection of electrons) cannot be compensated in time with other surrounding free electrons. Charging is an important error to consider especially among semiconductor and insulating samples, where the concentration of free electrons is relatively low. Methods such flood gun and sample heating are typically used to reduce the charging effect. From our C 1s spectra, we found no evidence of surface charging, as the C- C peak locates precisely at 284.78 eV. The lack of surface charging means that the resulting film has relatively high conductivity of electrons, which attribute to high electron mobility and/or charge carrier population of electrons.

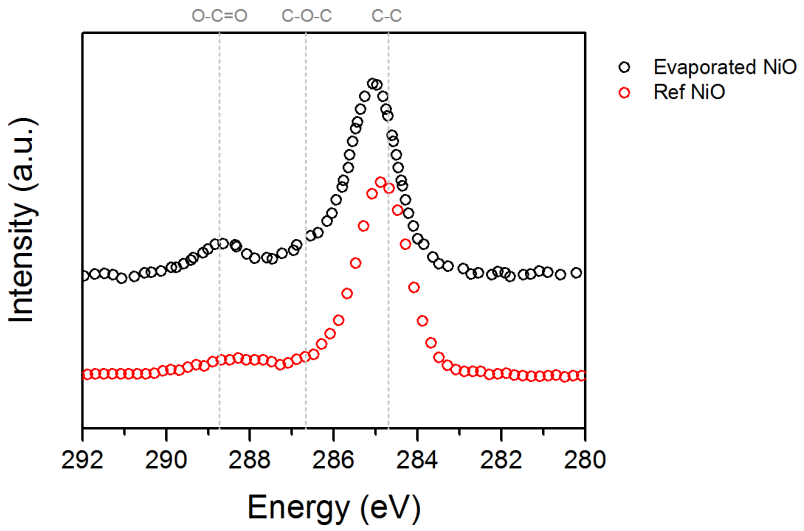

Figure 3.12 C 1s spectra of Evaporated NiO_x sample in comparison with the NiO reference (Sigma Aldrich, adapted from Ref [228]).

O 1s spectra contains information of the oxygen species on the surface and within the crystal structure. Surface oxygen typically consists of adsorbed water and surface hydroxides, whereas the lattice oxygen shows the existence of oxides. It is usually difficult to distinguish between surface oxygen species, owing to the overlapped peak positions. Two metal sources, Ni and W, adds further complications to distinguish between difference

hydroxide species ($Ni(OH)_2$ and $W(OH)_6$). Despite the difficulties with the overlapping peaks, the distinction between surface oxygen and lattice oxygen is apparent: Surface oxygen is typically found at higher binding energy. In **Figure 3.13**, our sample O 1s is compared with a NiO reference sample. Nickel oxide lattice oxygen (Ni-O) has a characteristic peak at ~529.00 eV. Similar to most transition oxides, this oxide peak is seldom reported to overlap with surface oxygen species. In contrast, our sample shows an absence of the lattice oxide peak at lower binding energy, but only a dominating peak at higher binding energy.

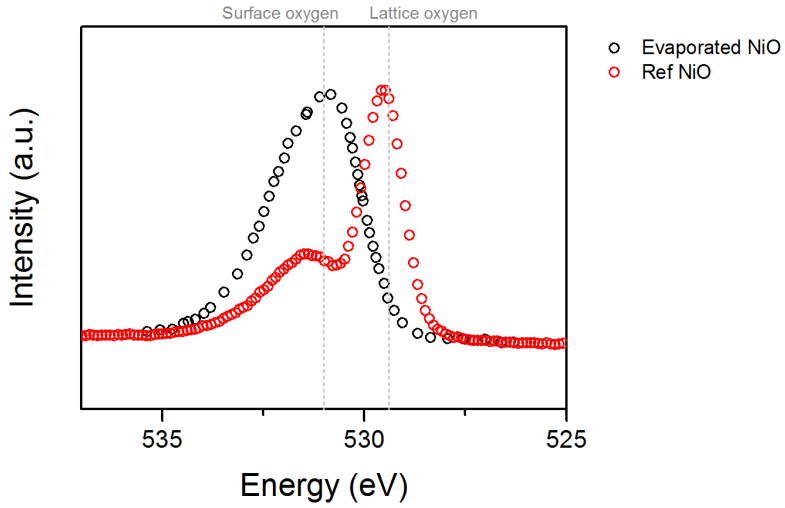

Figure 3.13 O 1s spectra of evaporated NiO_x sample in comparison with the NiO reference (Sigma Aldrich, adapted from Ref [238]).

3.8 Impact of W-content on film properties

In sections 3.5.1 and 3.5.2, we studied the optical and electronic properties of evaporated films as a function of thickness variation without consideration of existence of W as it was unknown at the time of these characterizations. Therefore, after the unexpected discovery of W in the evaporated samples and obtaining different Ni:W ratios, the impact of W:Ni ratio on the optical characteristics and electronic structure of the thermally evaporated films was investigated for certain sample thickness (10 nm).

3.8.1 Optical Properties

Ultraviolet-visible-infrared (UV-Vis-NIR) transmittance spectra were obtained in 200-1200 nm range for evaporated films as a function of W:Ni ratios (10, 13, 20, 25 at.%), against an air reference as shown in **Figure 3.14**. High transmittance was obtained in the wavelength range 400 to 1200 nm, with an average transmittance of 85%. However, the film of 25 at% W:Ni ratio varied considerably from the other samples and shows lower transmittance in the UV range.

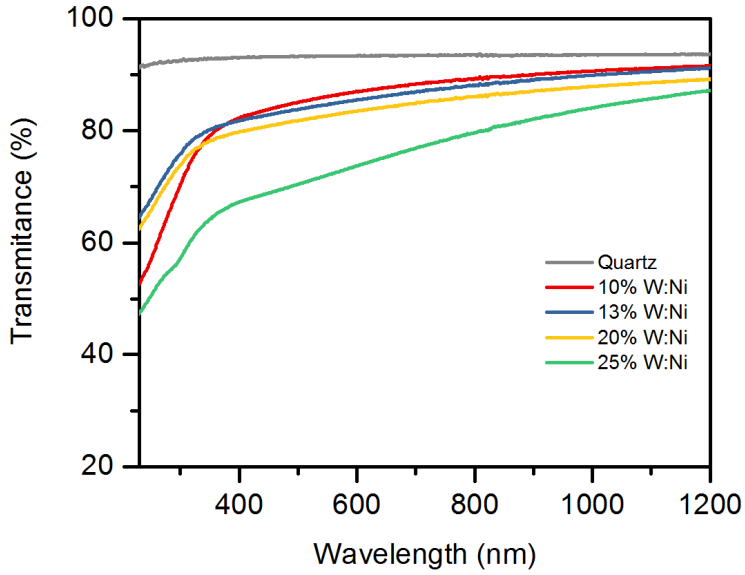

Figure 3.14 Transmittance spectra of evaporated films with different W:Ni ratios, deposited on quartz substrates.

Subsequently, the absorbance and absorption coefficient were calculated from the transmittance and reflectance spectral data in order to determine the optical bandgap of the evaporated films of Various W:Ni ratios using Tauc analysis. The optical bandgap (E_g) was obtained from the linear fit of Tauc plot as shown in **Figure 3.15** and found to be ~ 3.00, 3.20, 3.10, and 3.00 eV for films of (10, 13, 20, and 25 at%) W:Ni ratios respectively.

These E_g values are different from the previously calculated one in figure 3.5 which is attributed to the unexpected existence of W level with different ratios.

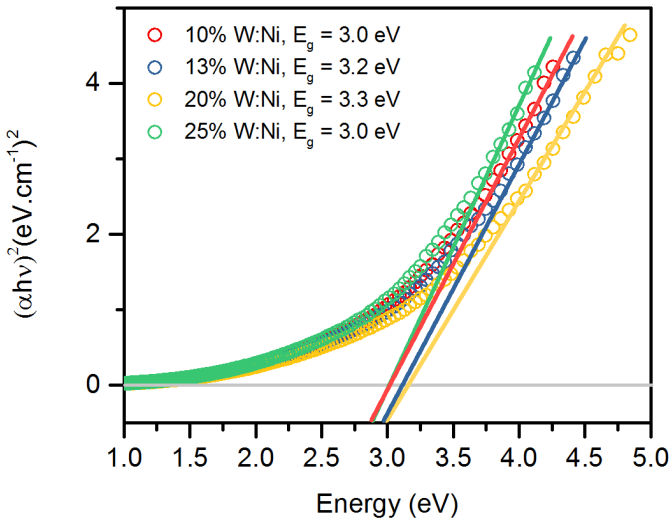

Figure 3.15 Tauc plots of thermally evaporated films of different W:Ni ratios, $(\alpha h\nu)^2$ is calculated from the absorbance spectra of the deposited films on quartz.

3.8.2 Surface morphology

The surface morphology of films evaporated on ITO-coated glass substrates was investigated as a function of W:Ni ratios by using tapping-mode atomic force microscopy (AFM) as shown in **Figure 3.16**. The surface height (nm) data were extracted at identical resolution from AFM topography images in order to generate representative distributions. In addition, large scan area ($10\ x\ 10\ \mu m$) was used in order to represent the large area film uniformity data and there was no evidence of microscopic pinholes and defects.

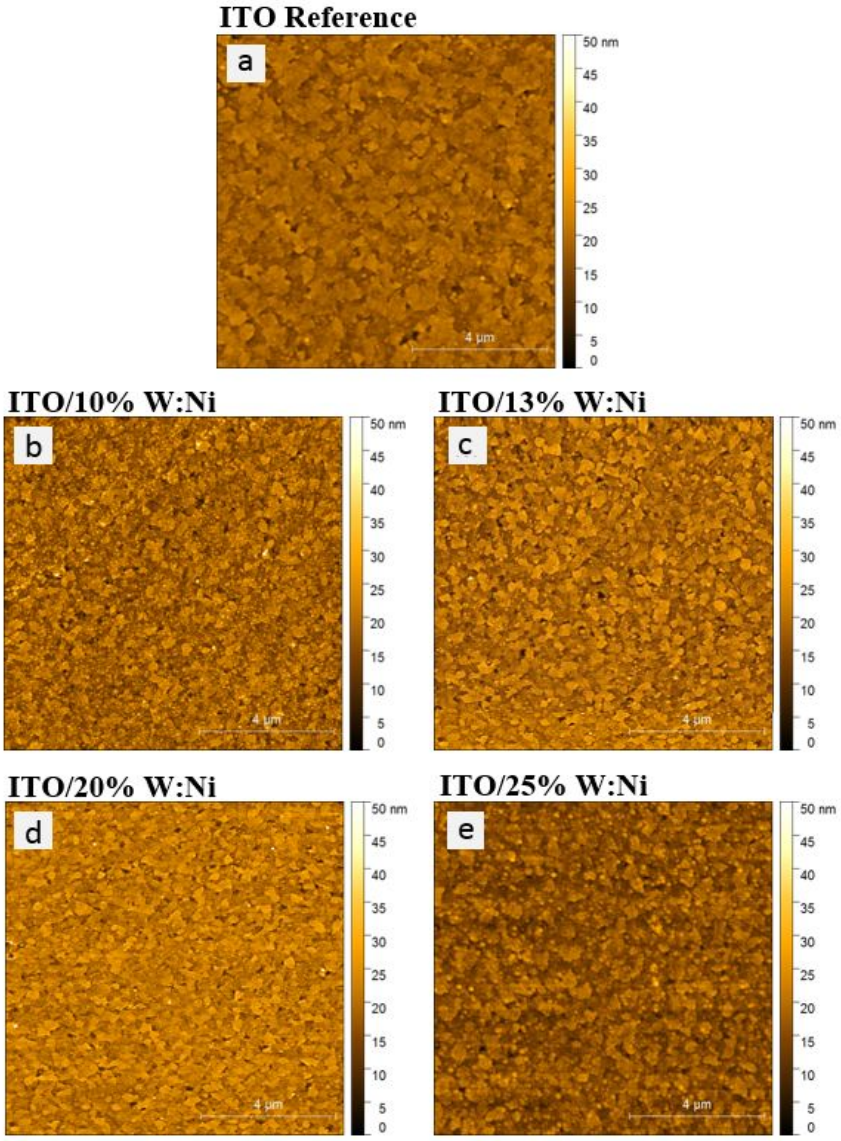

Figure 3.16 AFM surface topography images (scan area of $10\ x\ 10\ \mu m$*) of evaporated films of various W:Ni ratios deposited on glass-ITO: (a) bare ITO reference substrate. (b) 10 at% W:Ni, (c) 13 at% W:Ni, (d) 20 at% W:Ni, (e) 25 at% W:Ni, (e) 25 at% W:Ni.*

The RMS values of ITO reference and evaporated films of various W:Ni ratios (10, 13, 20, 25 at%) were extracted from the height distributions as shown in Figure 3.17and were found to be 3.20, 2.97, 2.54, 2.29, and 2.33 ± 0.05% nm respectively. The obtained results show that all evaporated films have smooth surfaces, and this indicates that the thermal evaporation process significantly planarizes the ITO surface and decrease its surface roughness.

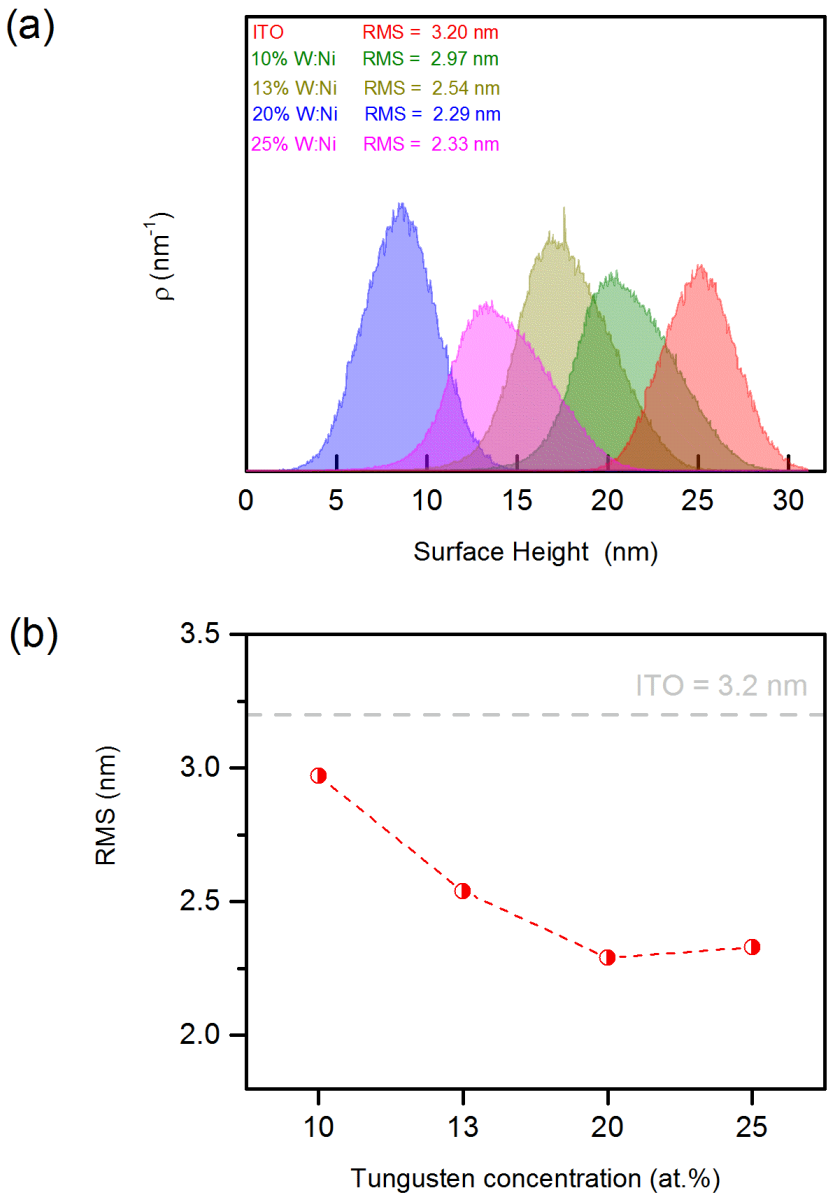

Figure 3.17 (a) Surface height histograms extracted from AFM data shown in Figure 3.16 of bare ITO reference, and thermally evaporated films of different W:Ni (10, 13, 20, 25 at%). (b) Surface roughness (RMS) calculated from the height distributions of (a) versus the W-concentrations.

It is clearly noted that the evaporated film with 20 at% W:Ni ratio has a uniform smooth surface with the lowest RMS ~ 2.29 nm. A smooth interfacial layer improves the contact quality at ETL/BHJ interface and limits the formation of charge recombination pathways within the active layer. This is essential for the enhancement of device performance [111].

3.8.3 Electronic properties

In order to investigate the impact of W:Ni ratio on the electronic structure of the evaporated films, kelvin probe measurements were carried out to determine the work function of evaporated films of different W:Ni contents as shown in Figure 3.18. The work function was found to be 3.80, 3.90, 3.95, 4.15 ± 0.05% eV for 10, 13, 20, and 25 % of W atomic concentrations respectively.

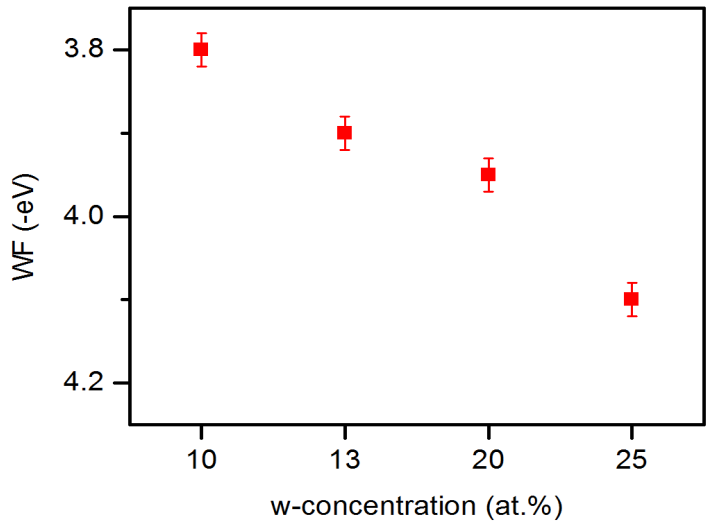

Figure 3.18 a) The work function of evaporated films on ITO substrates as a function of W concentration (10, 13, 20, and 25%), measured by Kelvin probe (KP).

These WF values are different from the previously calculated one in figure 3.6 which is attributed to the unexpected existence of W level with different ratios.

3.9 Impact of W:Ni ratio on OPV performance

In order to investigate the influence of the variation of W:Ni ratio in thermally evaporated films on the device performance, Inverted architecture of BHJ organic solar cells were fabricated based on P3HT:ICBA with evaporated films of different W:Ni ratios (10, 13, 20, and 25 at%) and ZnO reference as ETLs. The BHJ active layer (P3HT:ICBA) blend and ZnO thin film were prepared as previously explained in 3.6.1.

The J–V curves of fabricated devices are shown in *Figure 3.19* and the measured device characteristics were obtained in **Figure 3.20**.

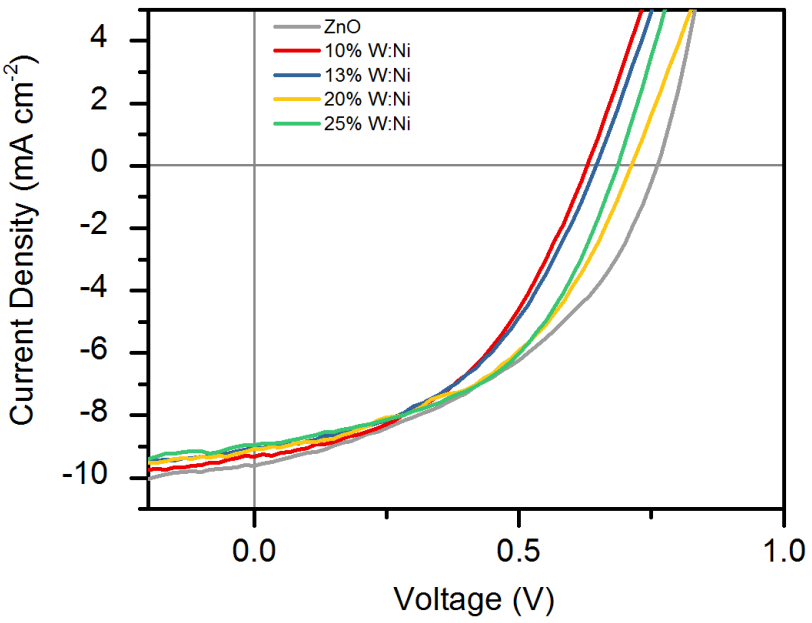

Figure 3.19 J-V curves measured under simulated solar light illumination for inverted P3HT:ICBA OPV cells based on evaporated films of different W:Ni ratios and ZnO as a reference.

It is notable that the W:Ni ratio impacts on the device performance. The Fill factor (FF) was improved from 0.40 to 0.46 as the W:Ni ratio increases from 10 to 20 at%. This increase could be attributed to the enhancement in shunt resistance (R_{sh}) which improves the interfacial contact between ETL and active layer and increases the number of charges reaching the cathode. However, when the W:Ni ratio increased to 25 at%, the FF decreased to 0.42 which is lower than that of 20 at%. This result was confirmed by investigating the surface morphology of evaporated films of different W atomic concentration. It was found that the evaporated film with 20 at% W:Ni ratio has a smooth surface with RMS ~ 2.29 nm which is lower than that of 25 at% (2.33 nm). A smooth ETL limits the charge recombination at ETL/BHJ interface which improves the FF. The short circuit current (J_{SC}) was reduced from 8.63 to 8.55 mA cm^{-2} as the W:Ni ratio increased from 20 to 25 at%. This decrease could result from lower transmittance of the film of 25% W:Ni than the other samples in the UV range. In addition to the higher series resistance (R_s) of the higher W concentration (25 at%) film as shown in **Figure 3.20**.

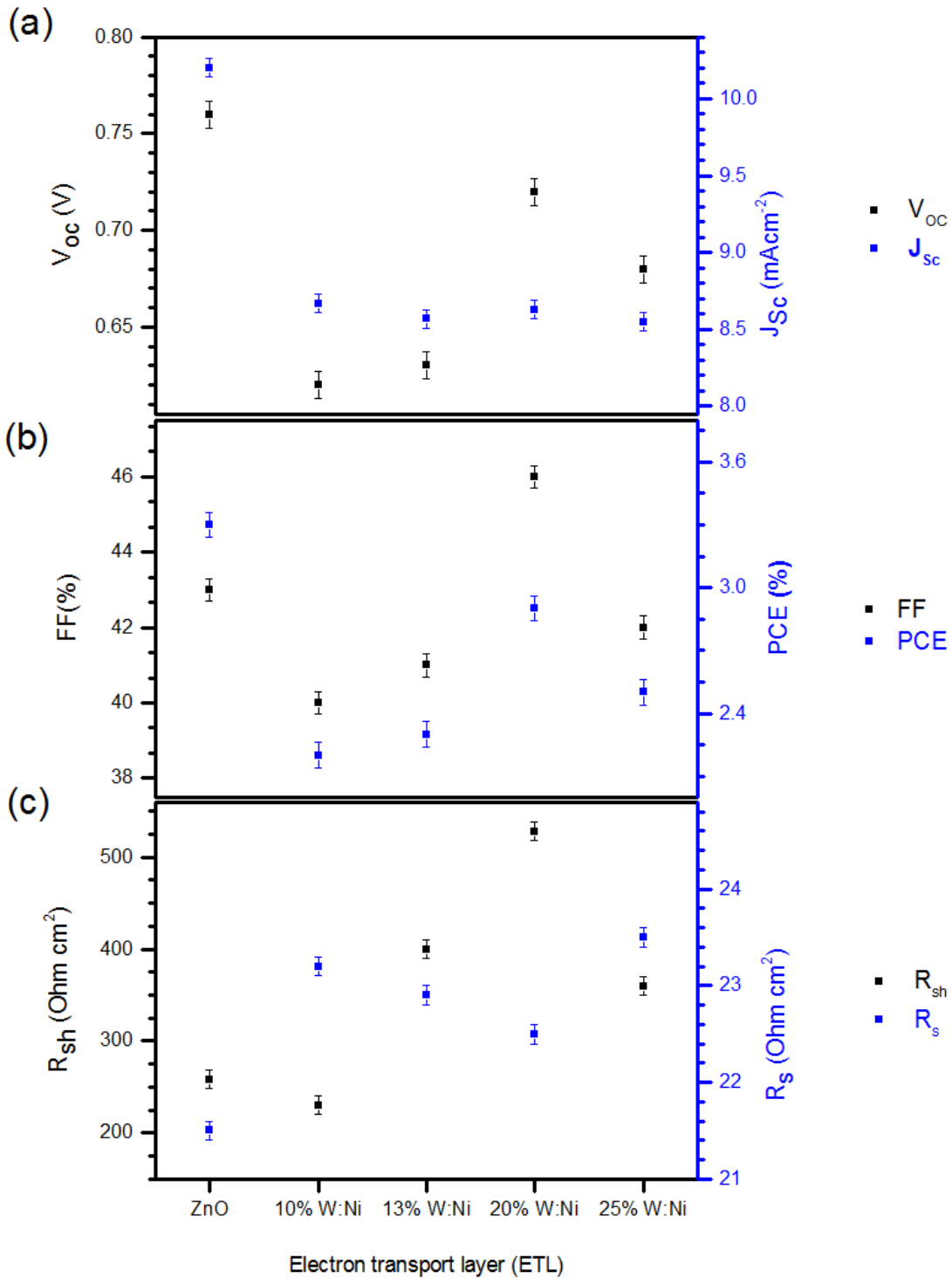

Figure 3.20 Measured device characteristics for P3HT:ICBA based OPV devices fabricated with ZnO and evaporated films of different W:Ni concentrations (10, 13, 20, 25 at%) as ETLs. (a) Open circuit voltage (V_{OC}) and short circuit current density (J_{SC}), (b) Fill factor (FF) and power conversion efficiency (PCE), (c) Shunt resistance (R_{sh}) and series resistance (R_s).

The open circuit voltage (V_{OC}) considerably increases from 0.62 to 0.72 V as the tungsten concentration increases from 10 to 20 at%. However, when the W:Ni ratio increased to 25 at%, the V_{OC} decreased to 0.68. This could be ascribed to the shift of the work function (WF) of evaporated films to lower energies with increasing the tungsten concentration as shown in**Figure 3.21**.

The WF changes from - 3.80 eV for 10 at% W:Ni film to - 4.15 eV for 25 at.% W:Ni film. The energy difference (ΔE) between the WF of evaporated films and LUMO of ICBA acceptor (- 4.00 eV) changes from 0.20, 0.10, 0.05, 0.15 eV for evaporated films of 10, 13, 20, 25 at% W:Ni ratios respectively. The lowest ΔE value is for 20 at% W:Ni which is ~ 0.05 eV. Smaller ΔE values are supposed to provide the better energy levels alignment between ETL and e^- acceptor, which increase the number of electrons being transferred upon contact, leading to a significant increase in the interface's conductivity and improves V_{OC} [229]. Therefore, 20 at% W:Ni ETL showed the best V_{OC} and device performance compared with other ratios.

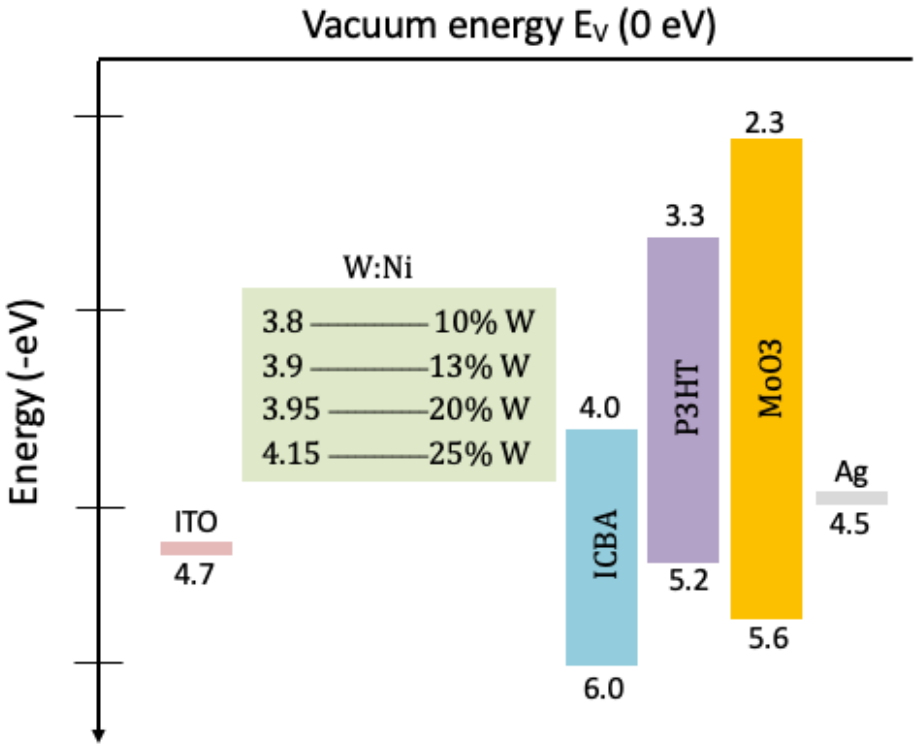

Figure 3.21 A schematic diagram showing the energy levels of various materials used in OPV device and the work function values of evaporated films with different W:Ni ratio(10, 13, 20, and 25 at%).

In brief, the device with the optimum (W:Ni ratio, 20 at%) ETL showed PCE of 2.90 ± 0.05% with V_{OC} of 0.72 V, J_{SC} of 8.63 mA cm^{-2} and FF of 0.46. However, OPVs with ZnO ETL exhibited PCE of 3.30 ± 0.05% with V_{OC} of 0.76 V, J_{SC} of 10.2 mA cm^{-2} and FF of 0.43.

The J_{SC} and V_{OC} of ZnO ETL are higher than that of evaporated film because of the better energy level alignment of ZnO with the active layer than that of evaporated film which improve the contact at ETL/BHJ interface. However, the FF of evaporated film is higher than that of ZnO and this because thermal evaporation provides uniform layers with precise thickness.

3.10 NiO_x as a Universal ETL

The potential of thermally evaporated films of 10 nm and 20 at% W:Ni ratio as a universal ETL was investigated by fabrication of BHJ OPVs with three different active layers, namely, (PTB7:$PC_{71}BM$), (PBDB-T:ITIC), and (PFBDB-T:C8-ITIC) as shown in Figure 3.22 .

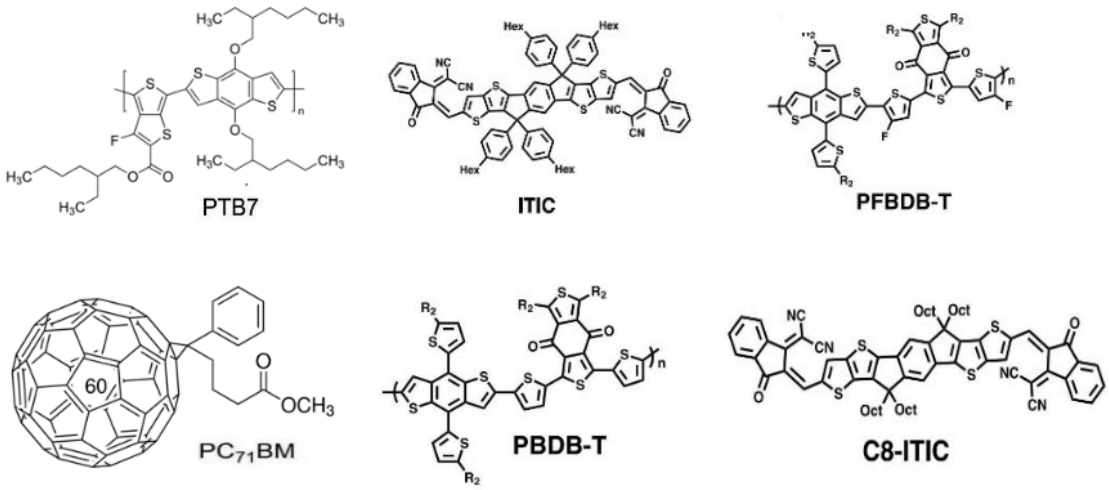

Figure 3.22 Chemical structures of the active layer components PTB7, PBDB-T, and PFBDB-T as donors while PC71BM, ITIC, and C8-ITIC as acceptors.

All devices were fabricated with inverted device architecture of ITO/ (ZnO or 10 nm of 20 at% W:Ni evaporated films as ETL) /BHJ of different donors and acceptors/MoO_3/Ag as shown in Figure 3.23(a) and (b) shows the energetics of the three donors and acceptors.

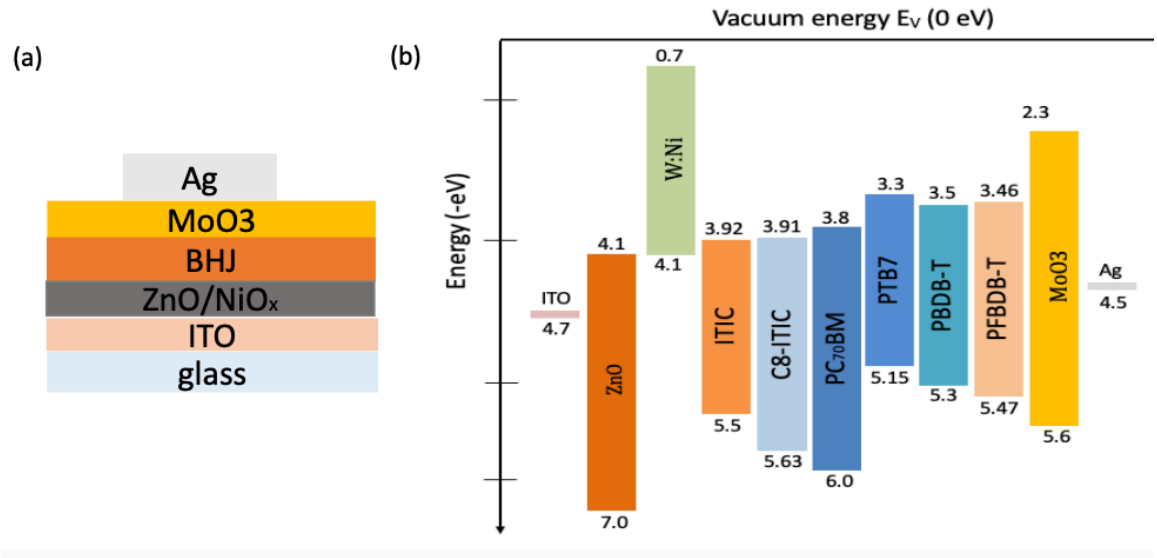

Figure 3.23 Fabrication of organic solar cells with evaporated films of different W:Ni ratios and ZnO as ETLS. (a) Schematic of inverted BHJ solar cell employed, and (b) Energetics of the different materials used.

The BHJ active layer blends were deposited on top of ~ 30 nm of ZnO and 10 nm films of 20% W:Ni as ETLs. PTB7 and $PC_{71}BM$ (1:1.5 w/w) were dissolved in a mixed solvent of chlorobenzene (CB) and 1,8-diiodooctane (DIO) (97:3 v/v) at a concentration of 25 mg ml^{-1}. The solution was stirred overnight at 60 °C in the glovebox. The solution was spin coated in on top of ETLs at 1000 rpm for 120 s. The PTB7:$PC_{71}BM$ films were not annealed but left in the vacuum chamber for 20 min to remove the solvent residuals [230].

While, PBDB-T:ITIC and PFBDB-T:C8-ITIC blend solutions were dissolved in chlorobenzene (CB) at a ratio of 1:1 w/w, and a concentration of 20 mg ml^{-1}, and were stirred overnight at 60 °C in the glovebox. 0.4 vol% of 1,8-diiodooctane (DIO) was used as an additive prior to the spin coating of the blends. Next, the blend solutions were spin coated on top of ETLs at 2000 rpm for 60 s, followed by at 140 °C for 15 min [41].

The thickness of the active layers was ~ 80-100 nm. To complete the devices, 10 nm MoO_3 and 90 nm Ag were evaporated in sequence under high vacuum 5 x 10^{-6} mbar using shadow masks to fabricate devices with active area 5 mm^2.

The J – V curves measured for PTB7:$PC_{71}BM$, PBDB-T: ITIC, and PFBDB-T: ITIC BHJ cells are shown in **Figure 3.24,** while Table 3.3 summarizes their characteristics.

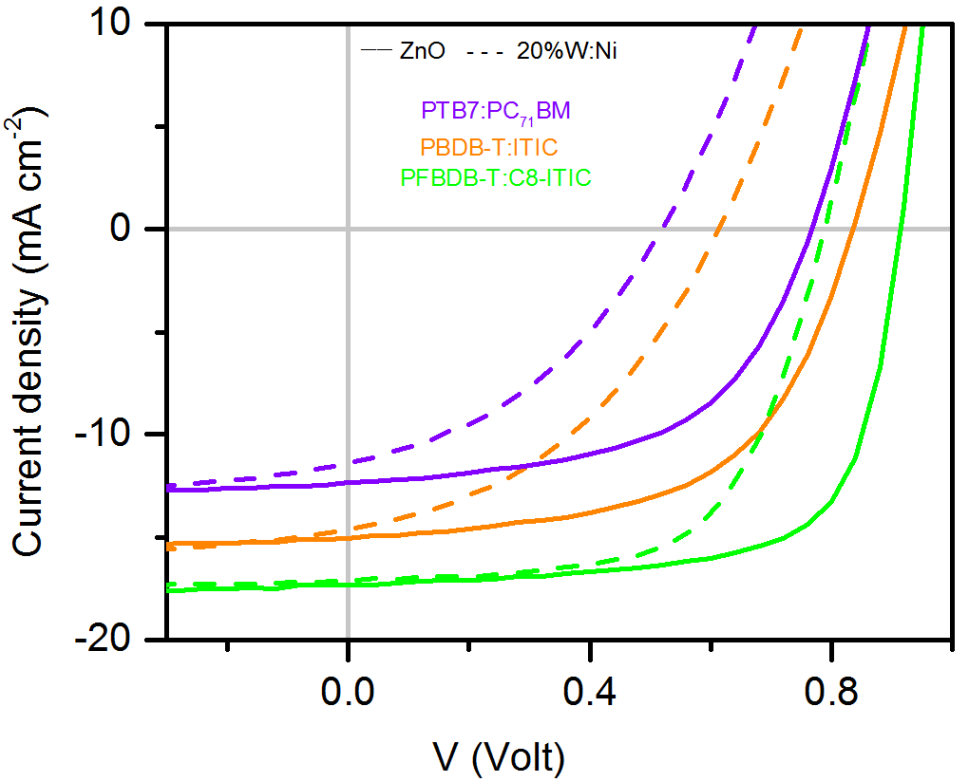

Figure 3.24 J-V curves measured under simulated solar light illumination for inverted OPVs based on different active layers (PTB7:PC71BM, PBDB-T:ITIC, and PFBDBT:C8-ITIC), all devices fabricated with 10 nm of 20% W:Ni and ZnO as ETLs.

It can be seen from Figure 3.24 that the evaporated film performs well as a universal ETL for different BHJ active layers. Notably, J_{SC} of OPV devices based on both ZnO and evaporated W:Ni show approximately similar values as shown in **Table 3.3**. However, V_{OC} of evaporated films is lower than that of ZnO for the three devices and this indicates an unfavourable energy level alignment between the work function of evaporated film and LUMO of acceptors.

Table 3.3 Summary of operating parameters for P3HT:ICBA, PTB7:PC71BM, PBDB-T:ITIC, and PFBDB-T:C8-ITIC OPVs with ZnO and 10 nm of 20% W-doped NiO_x as ETLs, measured under AM1.5 simulated solar illumination.

BHJ	P3HT:ICBA		PTB7:PC71BM		PBDB-T:ITIC		PFBDB-T:C8-ITIC	
ETL	ZnO	W:Ni	ZnO	W:Ni	ZnO	W:Ni	ZnO	W:Ni
J_{SC} (mA cm^{-2})	10.3	8.63	12.5	13	14.9	14.4	17.3	17
V_{OC} (V)	0.77	0.72	0.73	0.64	0.83	0.61	0.91	0.79
FF	0.43	0.46	0.65	0.59	0.57	0.41	0.69	0.62
PCE (%)	3.29	2.86	6	5	7	3.9	10.9	8.5

3.11 Conclusions

In conclusion, the thermal evaporation of controlled thickness, high optical quality NiO_x films was successfully demonstrated for the first time according to literature. It was anticipated that the films would exhibit p-type *i.e.* hole selective transport, however we show that those prepared are n-type in nature.

Firstly, evaporated films of different thickness (5, 7, 10, 20 nm) were employed as electron transport layers (ETLs) in BHJ OPVs in order to determine the optimum thickness which was identified to be 10 nm. The device with the optimum ETL thickness showed PCE of 2.86 ± 0.05% with V_{OC} of 0.72 V, J_{SC} of 8.63 mA cm^{-2} and FF of 0.46. However, OPVs with ZnO ETL exhibited PCE of 3.29 ± 0.05% with V_{OC} of 0.77 V, J_{SC} of 10.3 mA cm^{-2} and FF of 0.43.

X-ray photoemission spectroscopy (XPS) measurements were carried out for NiO_x films of 10 nm thickness in order to investigate the elemental composition and to understand the reasons of n-type nature of the evaporated films. Ni and W both showed dominating peaks across the survey spectra. The ratio between nickel and tungsten is calculated from the

area of Ni $3d_{3/2}$ and W $4f_{7/2}$. The existence of W- peaks explains the n-type nature of the evaporated films.

Subsequently, the impact of W:Ni ratio on the device performance was investigated by incorporation of 10 nm thick films of various W:Ni ratio (10, 13, 20, 25%). The device with the optimum (W:Ni ratio, 20 at%) ETL showed a PCE of 2.90 ± 0.05% with V_{OC} of 0.72 V, J_{SC} of 8.63 mA cm^{-2} and FF of 0.46. However, OPVs with ZnO ETL exhibited PCE of 3.30 ± 0.05% with V_{OC} of 0.76 V, J_{SC} of 10.2 mA cm^{-2} and FF of 0.43. The J_{SC} and V_{OC} of ZnO ETL are higher than that of evaporated film because of the better energy level alignment of ZnO with the active layer than that of evaporated film which improve the contact at ETL/BHJ interface. However, the FF of evaporated film is higher than that of ZnO and this because thermal evaporation provides uniform layers with precise thickness.

Finally, the potential of thermally evaporated films of 10 nm and 20 at% W:Ni ratio as a universal ETL was investigated by fabrication of inverted BHJ OPVs with three different active layers, namely, (PTB7:PC_{71}BM), (PBDB-T:ITIC), and (PFBDB-T:C8-ITIC). Notably, J_{SC} of OPV devices based on both ZnO and evaporated W:Ni show approximately similar values. However, V_{OC} of evaporated films is lower than that of ZnO for the three devices and this indicates an unfavourable energy level alignment between the work function of evaporated film and LUMO of acceptors.

4 Solution Processed Copper Oxide as a Hole Transport Layer

4.1 Introduction

Copper oxides (CuO_X) are drawing renewed attention as promising materials for a wide range of optoelectronic applications such as organic photovoltaics (OPVs), perovskite solar cells and field effect transistors. Their non-toxicity, earth-abundance, low-cost compatibility with solution processing make them favourable candidates for anode buffer layers in OPVs.

This chapter presents the development of solution-processed CuO_x layers and their application as anode buffer layer in organic photovoltaics (OPVs). First, microstructural analysis was attempted by X-ray diffraction (XRD) to study the thermal decomposition of copper acetate sol-gel precursor. XRD helps to identify the optimum annealing temperature of deposited films and confirms the presence of CuO_x. Basic optical characterizations such as transmittance, reflectance, and absorbance are studied with UV- visible-NIR spectroscopy, and the optical band gap of solution-processed CuO_x is determined by using the absorption coefficient calculation via Tauc plot analysis.

With additional electrical characterisation from Kelvin probe and air photoemission spectroscopy, work function and valance band maximum are determined. Furthermore, solution-processed layers of CuO_x of varying thickness and annealed at an optimum temperature are incorporated into bulk heterojunction OPVs and compared against control cells based on other commonly used HTL such as PEDOT:PSS. The impact of processing solvent variation on device performance is further studied. Finally, the film morphology is further provided by atomic force microscopy to understanding the effect of solvents on film formation.

This characterisation allowed a full understanding of the structure and optoelectronic properties of solution-fabricated CuO_x as well as to identify an optimum annealing temperature and film's thickness. Our work demonstrates the potential of solution- processed CuO_x as efficient hole transport layers for organic photovoltaic devices.

4.2 Electronic Properties of copper oxide

Binary copper oxides are cuprite (Cu_2O) and tenorite (CuO). Both Cu_2O (cubic) and CuO (monoclinic) are p-type semiconductors with a band gap of 2.10–2.60 and 1.90–2.10 eV respectively [137]. The p- type character of copper oxides stems from 1) Cu-vacancies (electron accepting defects) as shown in Figure 4.1 (a, b), which introduce an acceptor level at about 0.30 eV above the valence band (5.20 eV) as shown in Figure 4.1(c), and 2) the dominant Cu 3d structure near valence band maximum (VBM), which leads to a more dispersive valence band [149]. These characteristics give rise to high hole mobility in CuO_x, exceeding 100 $cm^2 V^{-1} s^{-1}$ [231]. Furthermore, the high work function of CuO_x (~ 5.30 eV) is close to HOMOs of many donors [136]. This leads to the formation of an Ohmic contact at the BHJ/anode interface.

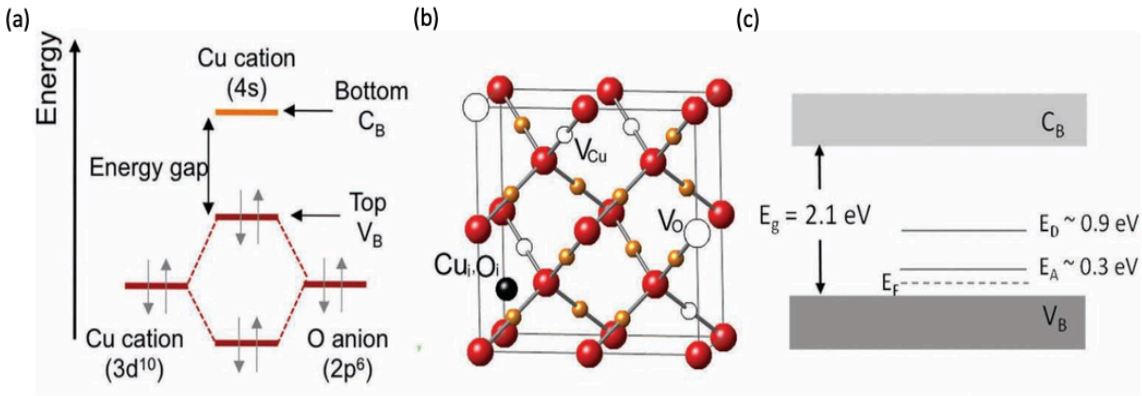

Figure 4.1 (a) A schematic diagram shows the chemical bonding in copper oxide, (b) the crystal structure of Cu_2O showing Cu and O defects, (c) Energy band structure of copper oxide showing the acceptor and donor levels which are 0.30 and 0.90 eV above valence band maximum respectively, taken from [149].

4.3 Review on Copper Oxide Hole Transport Layer

Lien et al. demonstrated CuO_x through the thermal vacuum deposition method as a hole transporting layer with a PCE of 4.06% obtained for P3HT:PC_{61}BM based OPVs with a notable enhancement in device stability, i.e. PCE maintained at 75% of the original value after 40 days [232]. However, this deposition method is very expensive and incompatible with high throughout production of OSCs.

Subsequently, Zhang et al. have employed CuO nanoparticles (NPs), prepared via sonochemical route, as an anode interlayer in PCDTBT:$PC_{71}BM$ based OPVs. PCE has been improved from 6% for PEDOT:PSS based OPV to 6.44% with CuO as HTL [233]. However, NPs tend to form rough film, which is undesirable to the deposition of an upper photoactive layer. Thus, there was a favorable demand for preparing CuO_x through cost-effective solution-processable method such as sol-gel process.

Next, Yu et al. have prepared CuO_x films from an aqueous solution of copper acetylacetonate (CAA) modified by hydrogen peroxide (H_2O_2) without the need of annealing in the ambient air. The resultant CuO_x layer shows high work function 5.45 eV and good optical transmittance (88% at 600 nm) in the visible range. The PCE of OPVs based on PTB7:$PC_{71}BM$ with CuO_x as an anode buffer layer is 8.68%, higher than that of PEDOT:PSS. Moreover, the CuO_x anode buffer layer enhanced the long term stability of the devices to become much better than devices based on PEDOT:PSS buffer layer [234].

Subsequently, Xu et al. have prepared solution processed CuO_x films from 1,2- dichlorobenzene solution of copper acetylacetonate, followed by thermal annealing at 80 °C in the air for 20 min then 15 min UV-ozone treatment. By introducing this CuO_x film as an anode buffer layer, PCE of 4.10% and 6.72% were achieved for P3HT:PCBM and P3HT:ICBA BHJ PVs respectively. In addition, a remarkable PCE up to 7.14% was obtained by utilizing a narrow bandgap conjugated polymer PBDTTT-C, as a donor material [235]. Although CuO_x obtained from copper acetylacetonate (CCA) precursor has achieved the best efficiencies and better device stability when employed as an anode buffer layer. However, the solvent, dichlorobenzene, is not environmentally friendly and can dissolve the active layer. Moreover, the CAA powder cannot dissolve in green solvents such as pure water [234]. Therefore, the use of another precursor is needed.

Kim et al. synthesized Cu_2O thin films by sol–gel method from Cu (II) acetate monohydrate dissolved in 2-methoxyethanol with monoethanolamine (MEA) as a stabilizer. However, films deposited by spin coating method have poor surface uniformity [236]. Therefore, in order to improve the morphology of the films, the post annealing process was carried out in two steps, first in nitrogen at 400 °C followed in oxygen atmosphere for 30 min each. The resulting Cu_2O films exhibited field effect mobility of 0.16 $cm^2\ V^{-1}\ s^{-1}$.

In a similar approach, Yu et al., fabricated CuO_x thin film by spin coating a precursor of copper acetate monohydrate $Cu(COOCH_3)_2.H_2O$, dissolved in a different solvent, N,N- dimethylformamide (C_3H_7NO), with MEA under ambient conditions. Furthermore, the annealing process was modified into only one step in the vacuum at various temperatures (400-700 °C) for 2 hours. The resulting films have shown higher field-effect mobility of 0.29 $cm^2\ V^{-1}\ s^{-1}$ [237]. However, these expensive post-annealing processes are not compatible with low cost R2R production techniques of solar cells. Moreover, the used solvents are not safe and environmentally friendly. Thus, different solvents and annealing process in ambient condition have been employed to solve the mentioned drawbacks.

Afterwards, Lin et al. have deposited CuO_x films (10 nm) via sol–gel route from the solution of copper (II) acetate monohydrate in IPA mixed with monoethanolamine (MEA) and deionized water. The PCE of the inverted device structure based on P3HT:PC_{61}BM as an active layer was enhanced from 3.11% (without the CuO_x interlayer) to 4.02% (with the CuO_x interlayer). Furthermore, the PCE of devices, after ~ 42 days, reduced to 1.5% without CuO_x and to 3.5% with CuO_x respectively [238]. By using another solvent, Shen et al. prepared a mixture of CuO and Cu_2O by the spin coating of 2-ethoxyethanol solution of copper acetate, then the films were thermally annealed at 160 °C for 1 h in air. The device based on P3HT:PC_{61}BM as an active layer and copper oxides mixture as an anode buffer layer, exhibits an enhanced PCE of 4.14% and long-term stability better than that of PEDOT:PSS device [239]. Next, electro-sprayed Cu_xO was fabricated by Bu et al. from copper acetate precursor dissolved in ethanolamine. A PCE of 5.83% was achieved for large area perovskites solar cells with Cu_xO as anode buffer layer compared to 4.01% for PEDOT:PSS control devices [240]. CuO p-channel of field effect mobility of $4x10^{-4}\ cm^2\ V^{-1}\ s^{-1}$ was successfully by Lee et al. fabricated from thermal annealing of Cu(II) acetate at 500 °C [241]. Most recently, Siddiqui et al. enhanced the light collection ability of P3HT:PC_{70}BM by incorporation of CuO NPs dispersed in dichlorobenzene and PCE of 3.82% was achieved [242].

In conclusion, CuO_x is a promising alternative to PEDOT:PSS for OPVs with significantly enhanced efficiency and device stability. However, more investigation of better precursors as well as processing conditions is needed. Therefore, this work presents the development of solution-processed CuO_x layers and their application as anode buffer layer in organic photovoltaics (OPVs).

4.4 Materials Preparation & CuO/Cu_2O Thin Film deposition

Metal carboxylates, such as acetates, are the most widely used precursors for fabrication of metal oxides such as NiO and CuO_x [208, 238]. The acetate precursor can be decomposed in solution by hydrolysis producing a sol-gel of either metal oxide or the corresponding hydroxide which can be oxidised by thermal annealing. Alcohols such as 2-methoxyethanol are suitable solvents for this precursor as pure water will induce complete hydrolysis and subsequent precipitation of the oxide [243]. To improve the solubility and the stabilisation of the precursor solution, chelating ligands such as monoethanolamine (MEA) can be used as the amine group can coordinate with the metal cation in solution, preventing flocculation and precipitation of insoluble products. However, these chelating ligands should be removed from the thin film, by postdeposition annealing processes [244].

In this work, a facile and green method was demonstrated to obtain the solution-processed ultrathin CuO_x film. 0.8 g of copper (II) acetate monohydrate (Aldrich, 98%, $Cu(CH_3COO)_2{\cdot}H_2O$) as a metal cation was dissolved in 10 ml of 2-methoxyethanol (Aldrich, 99.8%, $CH_3OCH_2CH_2OH$) or isopropanol (IPA) (Aldrich, 98%, $(CH3)_2CHOH$) solvent with addition of 1.4 M of monoethanolamine (MEA) (Aldrich, 98%, C_2H_7NO) as a stabilizer. Subsequently, the solution was first stirred at 60 °C for 1 hour then kept under constant stirring overnight at room temperature until a clear blue solution was formed. Before spin coating, the substrates were cleaned by sonication in distilled water, acetone, and isopropanol for 10 min each, and exposed to UV- ozone for 15 min to improve the surface uniformity and in addition, the solution was filtered through a 0.45 µm PTFE filter. Then the precursor solution was spin-coated on the substrates at 3000 rpm for 30 sec with an acceleration of 3000 rpm/sec, followed by annealing at different temperatures for 10 min

on a hot plate in air. The backside of substrate was cleaned using isopropanol after every deposition to ensure optical properties were not compromised.

The solution was spin-coated dynamically in order to produce a better uniformity and avoid the solvent evaporation before the start of the spinning. The spin coating and annealing processes were repeated different times to obtain different film thicknesses. The annealing temperature was chosen according to a previous study of thermal decomposition of the copper acetate, which stated that the decomposition process of copper acetate into Cu, Cu_2O, and CuO occurs between 168 – 302 °C as shown below [245].

1st Step:

$$Cu(CH_3COO)_2 \rightarrow CuCH_3COO + CH_3COOH \Rightarrow$$

$$CuCH_3COO \xrightarrow{\dot{H}} CH_3COH + CuO$$

$$\rightarrow Cu + CO_2 + \dot{C}H_3$$

$$\xrightarrow{\dot{H}} Cu + CH_3COOH$$

$$CuO + Cu \rightarrow Cu_2O$$

2nd Step:

$$Cu \xrightarrow{\frac{1}{2}O_2} CuO \quad \text{AND} \quad Cu_2O \xrightarrow{\frac{1}{2}O_2} 2CuO$$

4.5 Thin Film Characterization

4.5.1 Microstructural Analysis of CuOx Thin Films

Characterization of the microstructure of synthesized films and the influence of processing temperature on the crystallinity of CuO_x films was performed by X-ray diffraction (XRD) as shown in Figure 4.2. The concentration of precursor was first fixed at 0.5M in order to deposit a film of sufficient thickness for XRD signal detection. Figure 4.2 illustrates the XRD pattern of deposited thin films annealed in air at different temperatures from 175-325 °C for 10 minutes. From the patterns, the peaks corresponded to copper and copper oxides were observed.

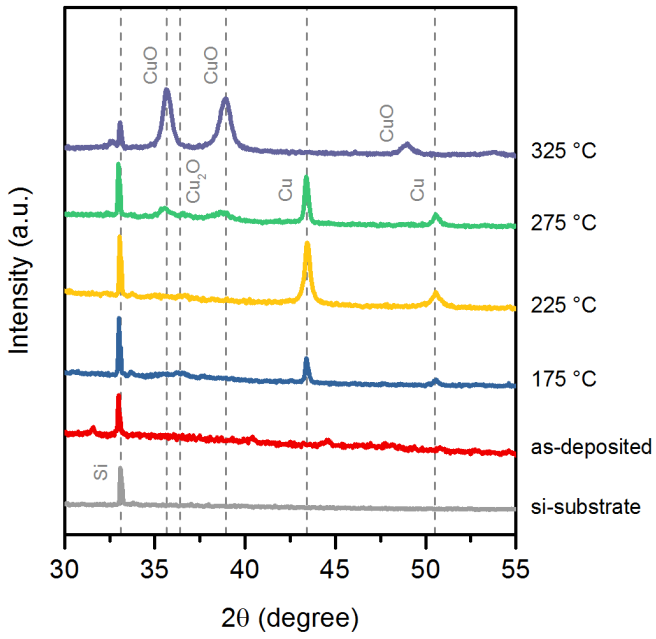

Figure 4.2 XRD patterns of thin films of the same thickness under different heating conditions, deposited on Si-substrate.

It can be seen that the XRD patterns for films annealed at 175 and 225 °C, the two main diffraction peaks at 43.5° and 50.1° match well with the standard JCDPS data (851,236) of the cubic phase of metallic copper. These peaks correspond to the (111) and (200) planes of a single-phase copper, respectively as there is no other peaks are noticed [246].

When the annealing temperature increases to 275 °C, XRD peaks show that the intensity of diffraction peaks for Cu decreases and become broad which indicates that more Cu was oxidised as the annealing temperature increases. This indicates the oxidation of the film forming a mixture of CuO, Cu_2O, and Cu according to the following formula [247],

$$2Cu + \frac{1}{2}O_2 \rightarrow Cu_2O$$

$$Cu_2O + \frac{1}{2}O_2 \rightarrow 2CuO$$

At 325 °C, more intense diffraction peaks of CuO were found which indicates that the film is largely converted into pure CuO, matching well with a monoclinic phase preferential crystal orientation in specific plane (standard JCDPS (050,611). Furthermore, the main Cu

phase peaks become weaker and the peaks of Cu_2O disappeared. These results are in a good agreement with a previous work done by Lin et al [245].

In summary, unlike n-type metal oxide, there is no one-step process to form copper oxide via sol- gel because of the strong intermediate Cu phase formation at low temperature or for short time at high temperature, followed by the oxidation of this formed copper resulting the formation of copper oxides such as Cu_2O and CuO [246].

4.5.2 Optical Characterization

After the successful microstructural identification of the deposited thin film and selecting the appropriate annealing temperature, the transmittance and reflectance spectra of deposited films on quartz substrates and annealed at 275 ˚C were measured in 220– 1200 nm wavelength range as a function of the film thicknesses. Then the absorbance and absorption coefficient were calculated in order to determine the optical bandgap of fabricated CuO_x using Tauc plot analysis.

The UV-Vis-NIR transmittance and reflectance spectra of solution-processed films with different thickness (10, 17, 21 nm) (measured by Dektak profilometer) were investigated, against an air reference, as shown in Figure 4.3 (a). The transmittance spectra show a variation for different thickness and the quartz substrate shows 93% high transparency with no light absorption.

All films show high optical transmittance in the NIR range (800-1200 nm), then the transmittance start to fall around 600 nm for all films agreeing with literature that discusses strong absorption of copper oxide film below 600 nm [232]. The absorption in the ultraviolet region is higher than in visible and NIR regions (600-1200 nm). The reflectance spectra for samples with different layers indicate approximately 6% reflectance over visible wavelength and the reflectance increases slightly by increasing film thickness.

In addition, the broad absorption peak at 350 nm for 17 and 21 nm films imparted the brownish appearance of the films (the colour of copper oxide) as the film absorbance depends on the corresponding wavelength as shown in Figure 4.3(b). However, this colour was not apparent for 10 nm film [248].

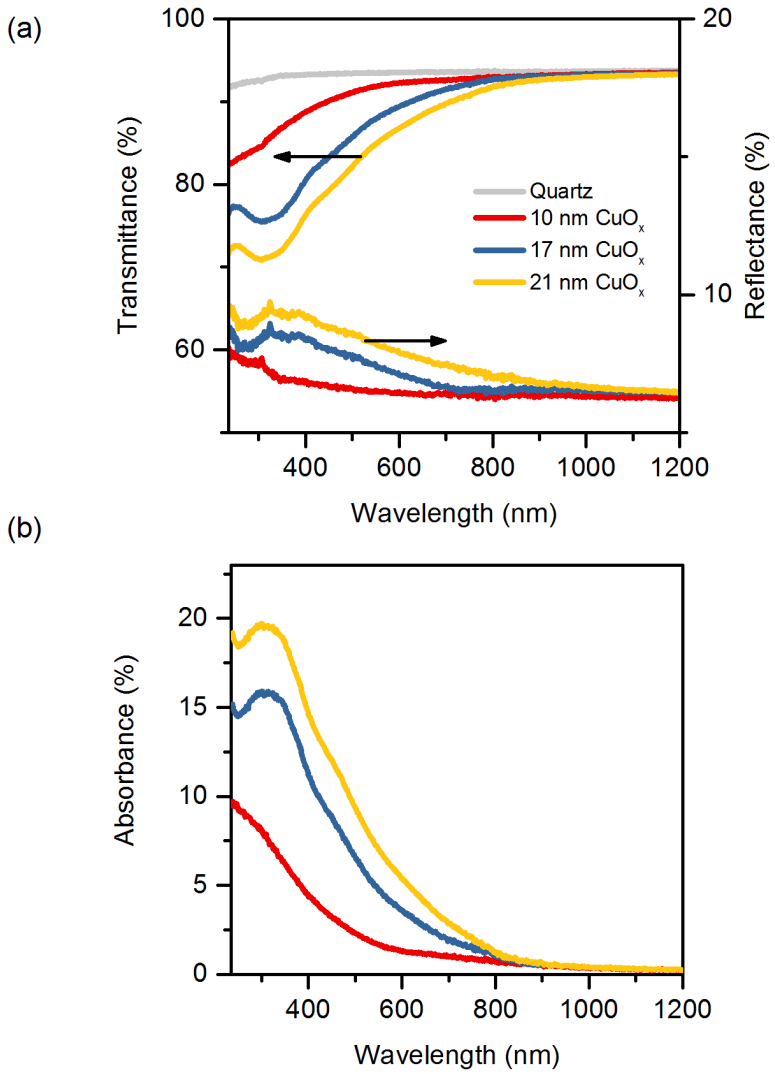

Figure 4.3 (a) Transmittance and reflectance spectra of CuO_x films annealed at 275 ˚C with different thickness showing high optical transparency, (b) UV-Vis-NIR Absorption spectra of the deposited films on quartz.

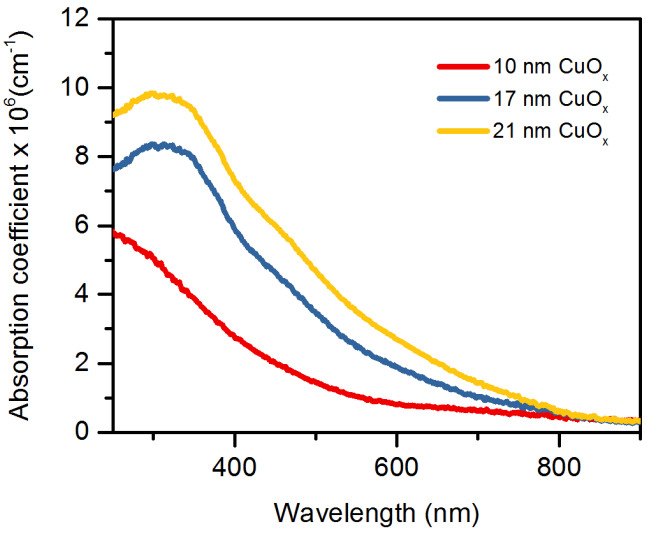

Figure 4.4 The absorption coefficient for CuO_x films with different thickness annealed at 275°C for 10 minutes.

In theory, absorbance of CuO_x film depends on layer thickness and the absorption coefficient is an intrinsic property which does not depend on film thickness. However, only absorption coefficient plots of 17 and 21 nm CuO_x films coincide. At a wavelength range of 300 - 800 nm, the absorption coefficient of 10 nm film is significantly smaller than that of 17, 21 nm CuOx films as shown in **Figure 4.4**.

The direct optical band gap (E_g) of solution-processed CuO_x films were obtained from a linear fit of Tauc plot and found to be approximately 3.1, 2.7, and 2.65 eV for thin films of thickness 10, 17, and 21 nm respectively as shown in **Figure 4.5**. These results show that solution-processed CuO_x has a wide band gap. The band gap calculated for 17, 21 nm CuO_x film are 2.70 and 2. 65 eV that can be considered as Cu_2O (2.1 – 2.6) [137] but for 10 nm, the band gap 3.10 eV is larger than theoretical values.

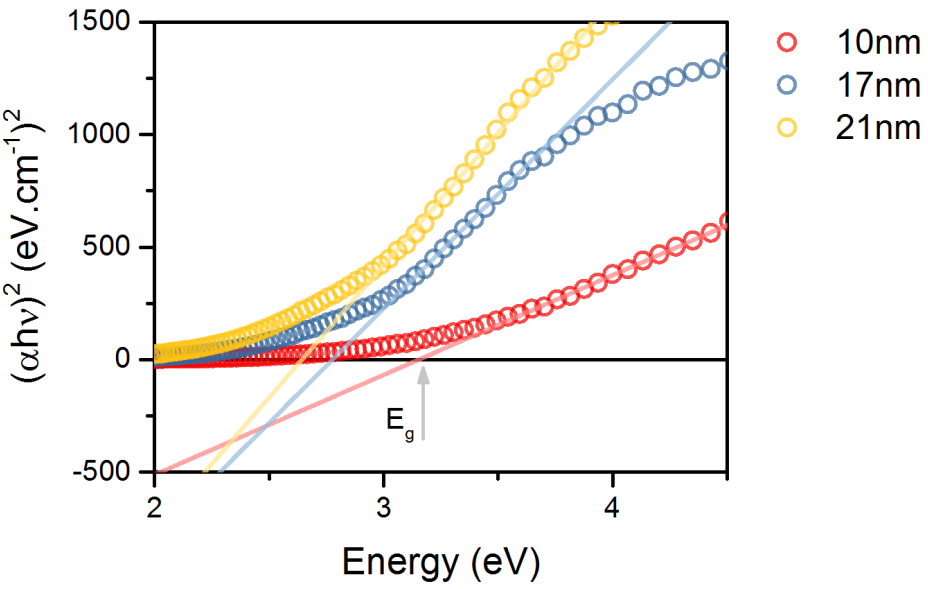

Figure 4.5 Tauc plots of solution-processed CuO_x of different thickness. $(\alpha h\nu)^2$ is calculated from the absorption spectra of the deposited films on quartz

4.5.3 Electronic properties of CuO_x thin films

It is essential to investigate the compatibility of solution processed CuO_x with the work function of common electrodes materials and HOMO of active layer materials. Therefore, Kelvin Probe (KP) and Air Photoemission Spectroscopy (APS) measurements were used to determine the electronic energy levels of the fabricated CuO_x such as the Fermi level (E_F) and the valence band maximum energy (VBM) as presented in **Figure 4.6**. The samples of different thickness were spin-coated on indium-tin-oxide (ITO) coated glass substrates and annealed at 275 °C in air atmosphere.

By measuring different sets of CuO_x films of different thickness (10, 17, 21 nm), the Fermi level (E_F) of CuO_x was measured as 4.77, 4.81, and 4.85 ± 0.02 eV respectively and was found to be dependent on the thin film thickness.

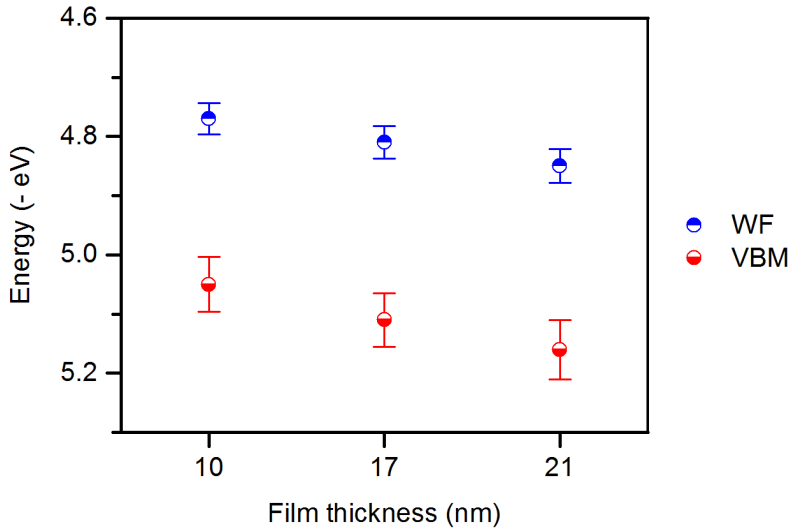

Figure 4.6 The work-function (WF) and the valance band maximum (VBM) measurements for CuO_x films of different thickness (10, 17, and 21 nm) annealed at 275 °C for 10 minutes in air.

For the valance band maximum (VBM) measurements, the sample was exposed to a UV source of 200 – 280 nm wavelength range and the photoemission from the surface was recorded as a function of incident photon energy. The VBM was found to be 5.06, 5.11, and 5.14 ± 0.05 eV for CuO_x films of thickness 10, 17, and 21 nm respectively which was extracted from the linear fit the photoemission spectra.

The Fermi level (E_F) of CuO_x was found to be 0.3 eV above the valence band maximum (VBM) which is in a good agreement with the literature and indicates the p-type nature of the fabricated CuO_x [149]. The obtained results indicate the potential of the solution processed CuO_x to be employed as HTL material as its E_F and VBM values match well with different HOMOs of donor materials.

The energy level diagram of solution-processed CuO_x can be constructed by measuring of VBM [5.06 – 5.14 ± 0.05 eV], optical band gap E_g [2.65 – 2.80 ± 0.01 eV], and E_F [4.77 – 4.85 ± 0.02 eV as lying ~ 0.30 eV above VBM as shown in Figure 4.7.

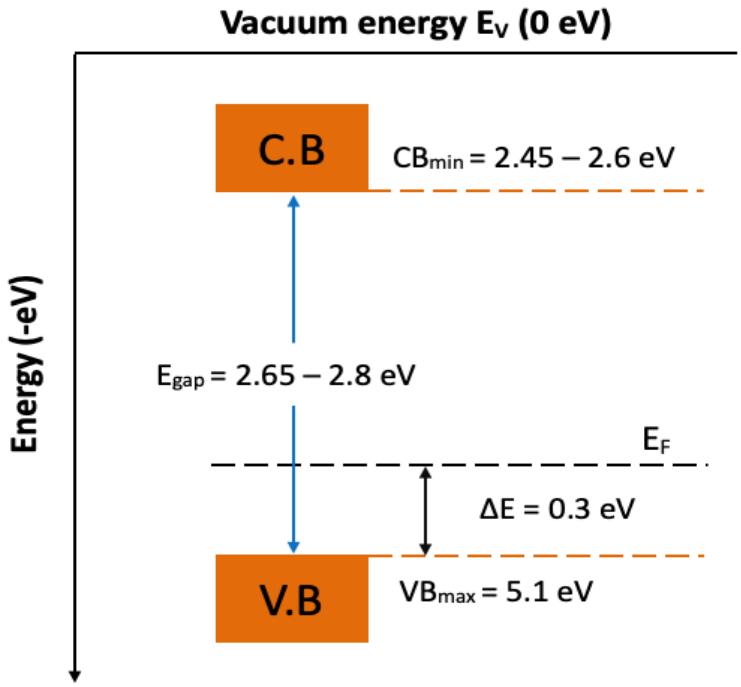

Figure 4.7 A schematic diagram of electronic energy levels of solution processed CuO_x including VBM which is in the range 5.06 – 5.1 ± 0.05 eV extracted from Air photoemission spectroscopy (APS), optical band gap E_g which is in the range [2.65 – 2.80 ± 0.01 eV], as lying ~0.30 eV above VBM using Kelvin probe measurements. The conduction band minimum (CBM) is also indicated.

4.6 Impact of thickness and processing solvent on device performance

4.6.1 OPV device fabrication

Organic solar cells were fabricated using CuO_x and PEDOT:PSS as HTLs. For PEDOT:PSS, an aqueous solution of PEDOT:PSS (Heraeus Clevios™ AI 4083) was used as purchased from Ossila Ltd. After filtering with a 0.45 µm PTFE filter, PEDOT:PSS solution was spun at 4000 rpm for 60 s followed by annealing at 150 °C for 10 minutes in air. The BHJ active layer blend was next deposited in inert atmosphere (dry nitrogen glove box) on top of the HTL layers (PEDOT:PSS, CuO_x) according to the following procedures: 1) a commonly used P3HT:ICBA blend system (1:0.5 weight ratio) was spin coated at 2000 rpm for 40 sec from a 24 mg mL^{-1} chlorobenzene solution. The P3HT was obtained from Prof. John De Mello's group with MW = 62 kDa [249], while ICBA was purchased from Ossila Ltd.

2) As-deposited films were then annealed at 150 °C for 10 minutes resulting in a film thickness of ≈100 nm. 3) After which the cells were completed by the thermal evaporation of a 10 nm thick layer of Calcium at deposition rate of 0.5 $Å s^{-1}$ 4) followed by evaporation of a 70-90 nm thick layer of silver electrode at rate of 1.5 $Å s^{-1}$, through shadow masks at a base pressure of 5 × 10^{-6} mbar [250]. The device area was determined by the overlap between the ITO strip and the cathode (0.045 cm^2). **Figure 4.8** shows the BHJ solar cell structure used and energetics of different materials used in fabrication of OPV.

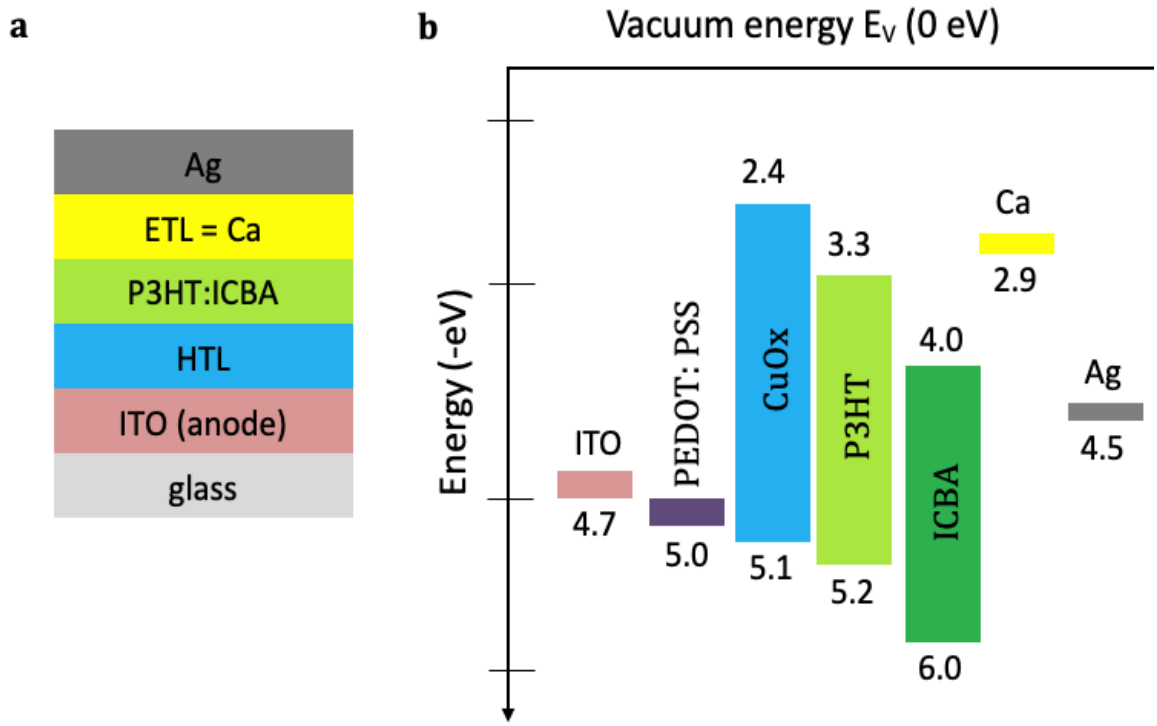

Figure 4.8 The fabrication of organic solar cells with CuO_x and PEDOT:PSS HTLS. (a) Schematic of conventional structure BHJ solar cell employed. (b) Energetics of the different materials used in OPV.

4.6.2 OPV device characterization

The J–V characteristics curves of the devices under the illumination of AM 1.5G, are shown in **Figure 4.9**, and the device parameters are summarized in **Figure 4.10**.

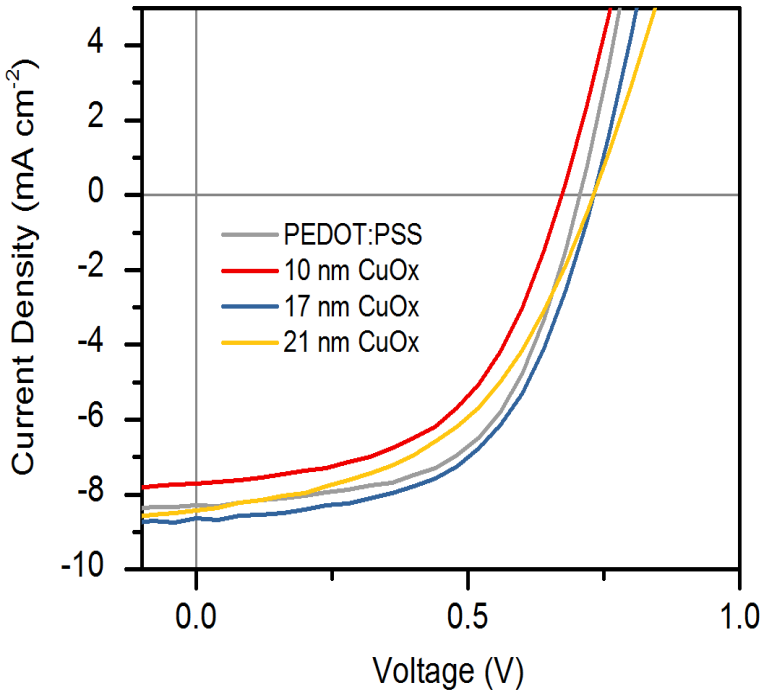

Figure 4.9 J-V characteristic curves measured under simulated solar light illumination for conventional architecture P3HT:ICBA OPV cells based on PEDOT:PSS as a reference and different thickness of CuO_x processed from 2-methoxyethanol solvent.

The reference device using PEDOT:PSS as HTL shows a PCE of 3.38 %, an open-circuit voltage (V_{OC}) of 0.7 V, a short-circuit current density (J_{SC}) of 8.29 mA cm^{-2}, and a fill factor (FF) of 0.57. The thickness of CuO_x film significantly impacts the device performance. The optimal thickness for CuO_x film was found to be 17 nm as the fill factor of 21 nm thick film is considerably (~ 8%) lower than that of 17 nm film. This drop can be attributed to the higher series resistance (R_s) of the thick film. On the other hand, V_{OC} and J_{SC} of 10 nm CuO_x film are lower than that of 17 nm film. This can be ascribed to the presence of pinholes due to the non-uniformity of the very thin CuO_x film.

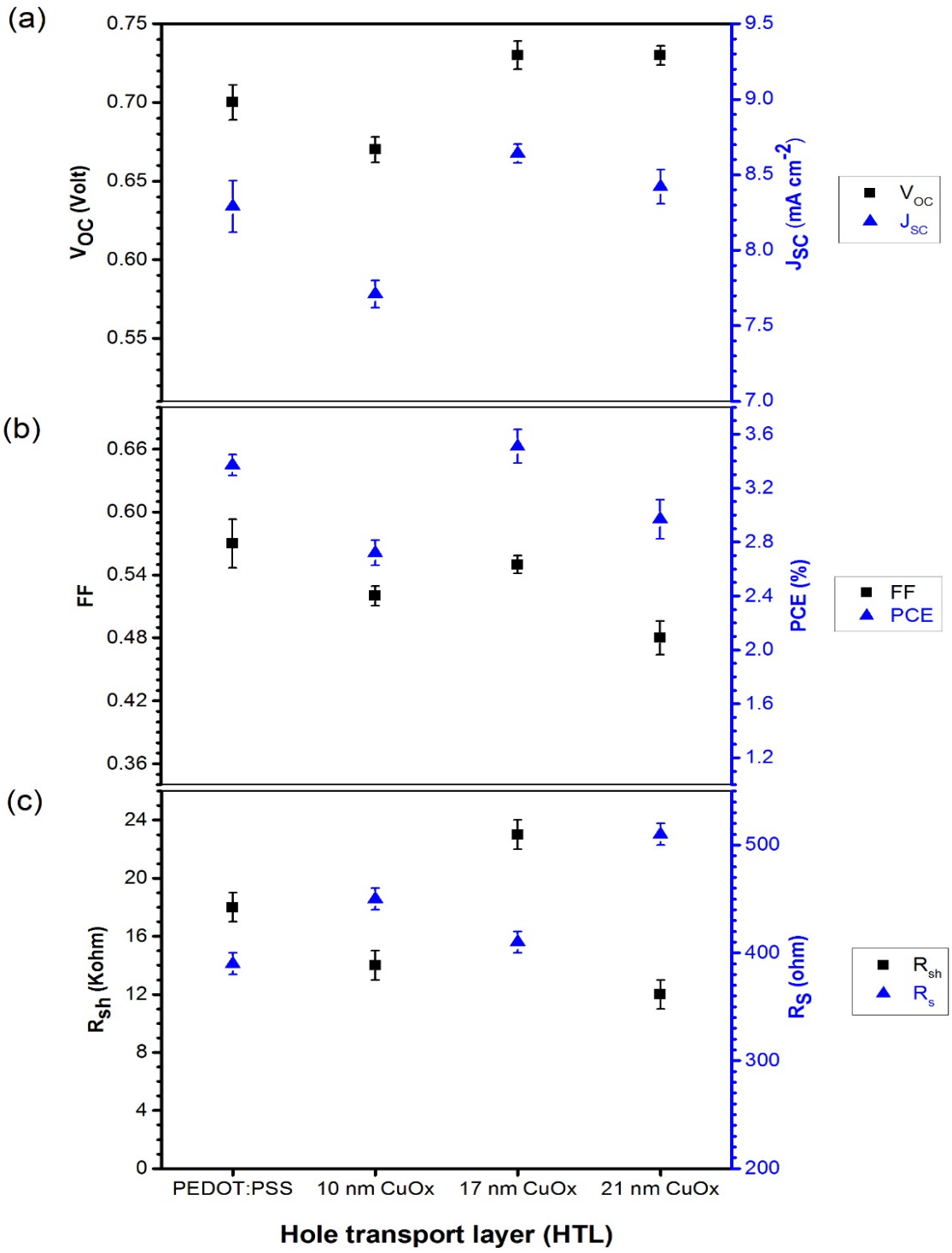

Figure 4.10 The measured device performance characteristics for P3HT:ICBA based devices fabricated with PEDOT:PSS and different thickness of CuO_x processed by 2-methoxyethanol as HTLs, measured under AM1.5 simulated solar illumination. (a) Open circuit voltage (V_{OC}) and short circuit current density (J_{SC}). (b) Fill factor (FF) and power conversion efficiency (PCE). (c) Shunt resistance (R_{sh}) and series resistance (R_S).

In conclusion, upon utilization of 17 nm of CuO_x as a hole transport layer (anode), the Voc and J_{sc} were enhanced to 0.73 V, 8.64 mA cm^{-2} respectively. Whereas the FF was slightly decreased to 0.55. Although the FF of CuO_x device is slightly smaller than that of PEDOT:PSS device, the PCE was further increased to 3.51 ± 0.05 %, which is 4 % higher than that of the reference device.

The enhanced J_{sc} of 17 nm of CuO_x device could arise from the increased hole collection at the CuO_x/active layer interface by decreasing series resistance which may originate from the high work function of CuO_x (~ 5.30 eV) [140], in addition to the higher transparency of CuO_x than that of PEDOT:PSS.

The higher V_{OC} of CuO_x based devices (17, 21 nm) than that of PEDOT:PSS is an indication of a favourable energy level alignment of the HTL with the photoactive layer which is mainly due to the well-matching work function values of CuO_x films. The enhanced V_{OC} of devices with a CuO_x buffer layer could result from the increase in R_{sh} as the photoactive layer is the same for all devices. Furthermore, the incorporation of copper oxide at the electrode reduces the charge carrier recombination through improving hole selectivity at the CuO_x/photoactive layer interface.

The FF shows variable values for devices fabricated with different thickness of CuO_x films. When the thickness increased from 10 to 17 nm, the FF increased from 0.52 to a maximum value of 0.55. However, as the thickness further increased to 21 nm, the FF decreased to 0.48. FF is determined by the number of charge carriers reaching the electrodes. Therefore, the better interfacial contact between CuO_x film and the active layer, the lower charge carrier recombination rate and this leads to a higher FF value [239]. Furthermore, the R_{sh} was changed with different thickness CuO_x films. For 17 nm CuO_x film, the higher R_{sh} results in higher FF which can reduce leakage current [239]. In brief, although the FF value (0.55) of CuO_x based device is slightly smaller than that of PEDOT:PSS device (0.57), the PCE of CuO_x device (3.51%) is higher than that of reference device (3.37%).

After the successful identification of the optimal thickness and annealing temperature for the CuO_x interlayer, the next step is to study the impact of solvent variation on the device performance. Therefore, CuO_x films were prepared again with the same concentration from but in this time, the precursor was dissolved in isopropanol (IPA) solvent instead of 2- methoxyethanol. Then the precursor solution was spin-coated on the substrates and annealed at the same conditions as used before giving similar films thickness (10,17, 21 nm).

The J–V characteristics curves of the devices prepared using IPA, are shown in Figure 4.11, and the device parameters are summarized in Figure 4.12

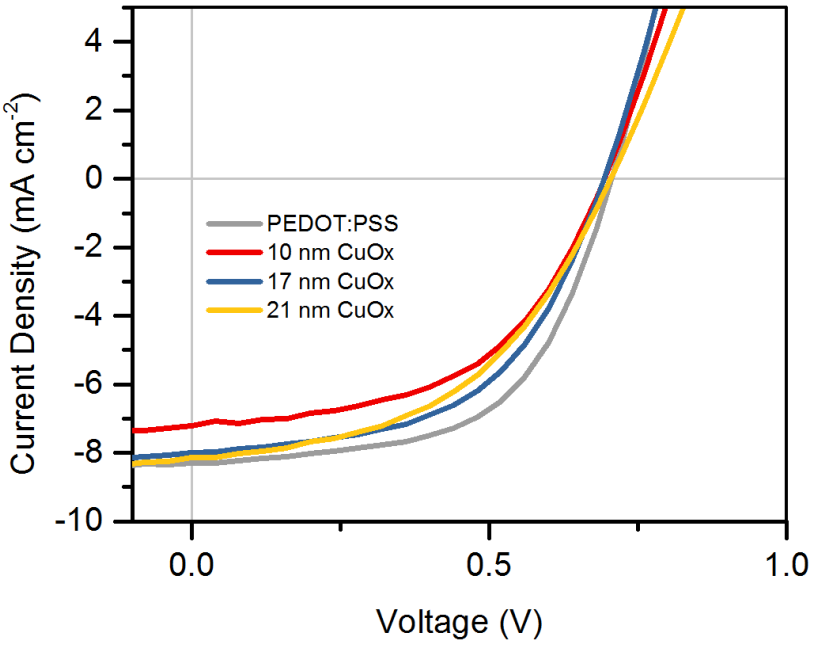

Figure 4.11 J-V characteristic curves measured under simulated solar light illumination for conventional architecture P3HT:ICBA OPV cells based on PEDOT:PSS as a reference and different thickness of CuO_x.

Upon insertion of CuO_x of different thickness (10, 17, 21 nm) processed from IPA solvent as a hole transport layer (anode), the V_{OC} values are approximately similar as that of films processed from 2-methoxyethanol. Furthermore, FF values show the same trend but with lower values than that of 2-methoxyethanol solvent. This is due to lower R_{sh} values which

reduce CuO_x/active layer interface quality and increase charge carrier recombination probability, and thus result in lower FF.

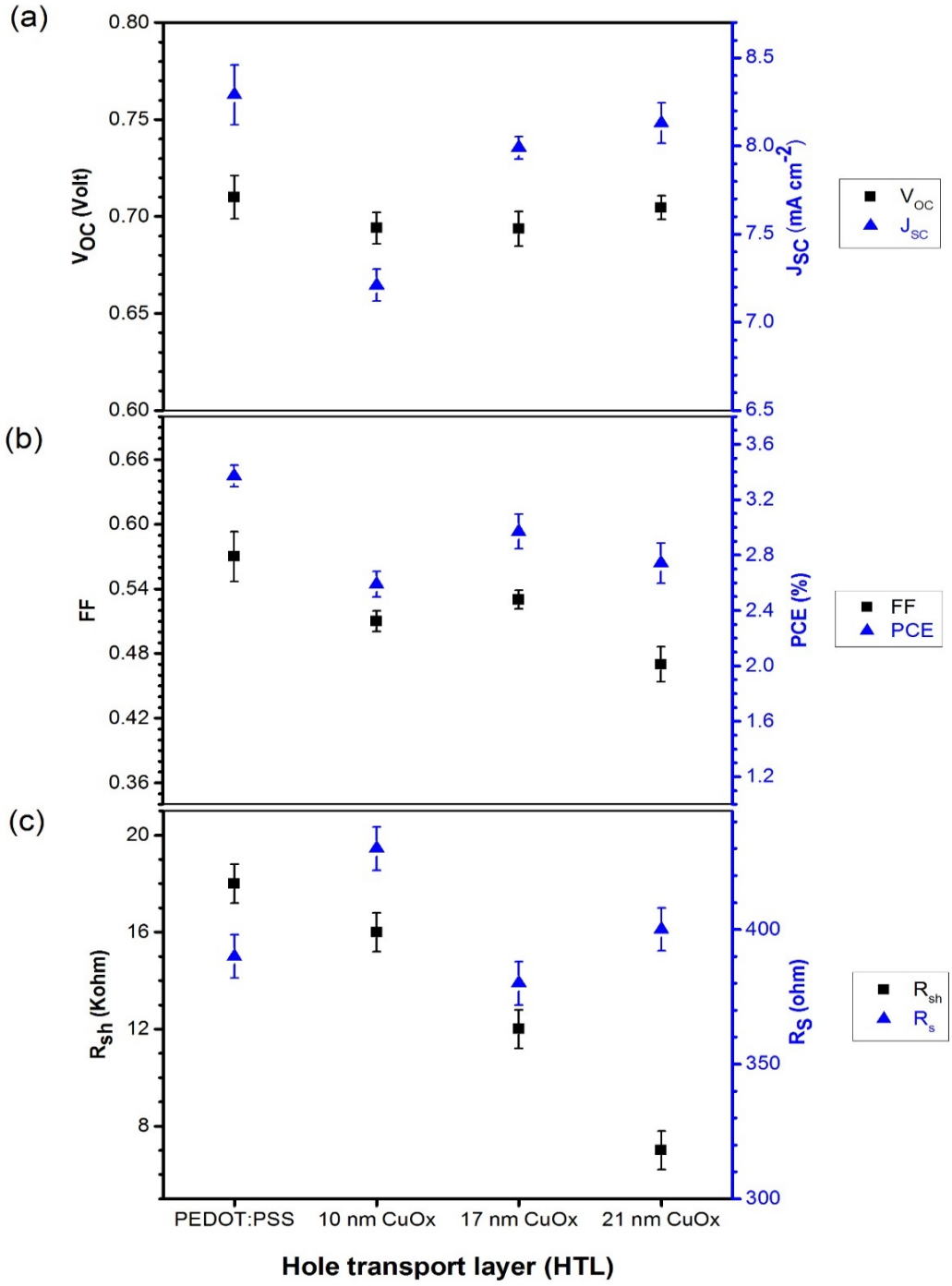

Figure 4.12 The measured device performance characteristics for P3HT:ICBA based photovoltaic devices fabricated with PEDOT:PSS and different thickness of CuO_x processed by IPA as HTLs, measured under AM1.5 simulated solar illumination. (a) Open circuit voltage (V_{OC}) and short circuit current density (J_{SC}). (b) Fill factor (FF) and power conversion efficiency (PCE). (c) Shunt resistance (R_{sh}) and series resistance (R_S).

The non-uniform interfacial contact between the CuO_x and the active layer contributes to lower R_S of the device and leads to a lower J_{SC} values. J_{sc} was decreased from 8.64 to 7.99 mA cm^{-2} for 17 nm CuO_x films processed by 2-methoxyethanol and IPA solvents respectively. The PCE was further decreased to 2.97 ± 0.05 %, which is 12 % lower than that of the reference device.

The results demonstrate that the utilization of CuO_x film of optimum thickness (17 nm) processed by 2-methoxyethanol is able to increase the R_{sh} and decrease the R_s of the device which enhance the J_{SC} and FF and result in higher PCE than that of reference device. However, CuO_x film fabricated by IPA result in lower PCE due to decreased J_{SC} and FF.

4.6.3 Surface morphology Analysis

The surface morphology was investigated by using tapping-mode atomic force microscopy (AFM) for two CuOx films of the same thickness (17 nm) processed from two different solvents (Isopropanol and 2-methoxyethanol) on glass substrates as shown in Figure 4.13.

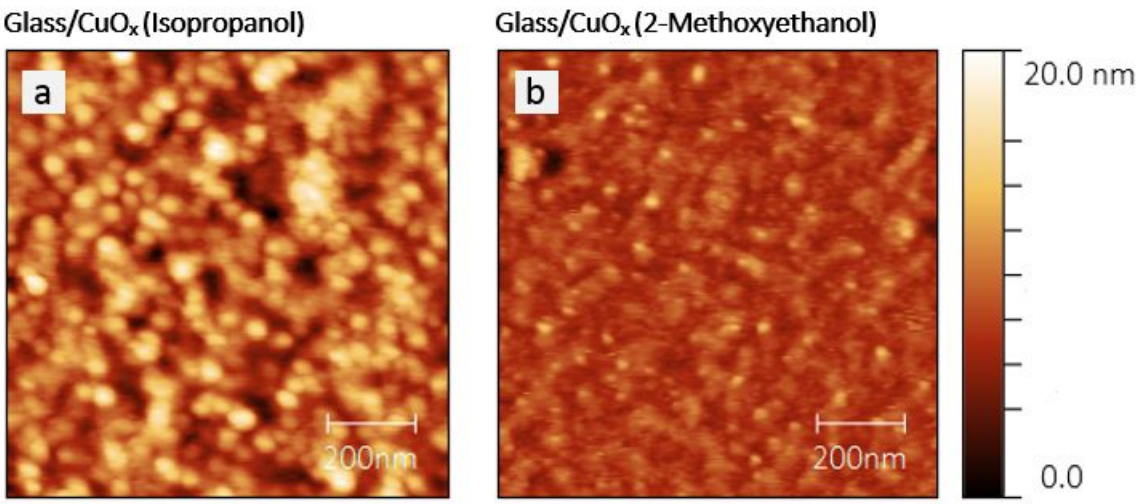

Figure 4.13 AFM surface topography images (scan area of 1 μm) of CuO_x films (17 nm) processed by two different solvents (Isopropanol and 2-methoxyethanol) on glass substrate and annealed at 275 °C.

The RMS roughness of CuO_x film formed by 2-methoxyethanol solvent is 1.5 nm, which is much smaller than that of the CuO_x prepared by Isopropanol (3 nm). This was attributed to the lower boiling point of IPA (82.5°C) than that of 2-methoxyethanol solvent (125 °C) [251]. The fast evaporation of solvent during spin coating process would result in rough thin film, while the gradual evaporation of the solvent with high boiling point would provide a smoother film.

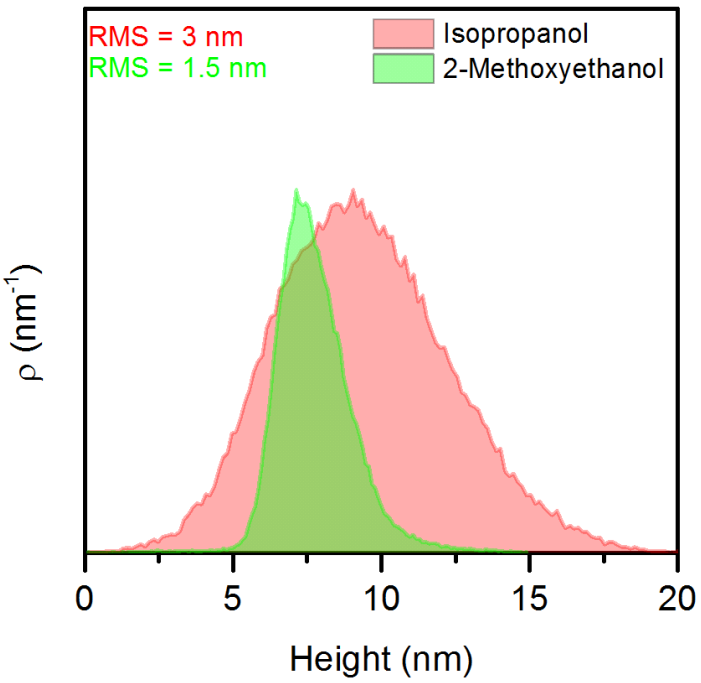

Figure 4.14 Surface height distributions extracted from AFM data in Figure 4.13.

It can be shown in *Figure 4.14* that CuO_x film processed by 2-methoxyethanol is more uniform than that prepared by IPA which is covered with particles. In addition, the surface height distributions show that CuO_x film processed by IPA produce features of dimensions spread over a wide range as shown in Figure 4.14. The device performance can be significantly affected by the poor morphology. The rough surface increases the number of interfacial areas so the scattered particles will act as recombination centres and could possibly cause pinholes in the active layer and decreases R_{sh} which affects the device performance.

4.7 Conclusions

In summary, we have successfully demonstrated solution-processed copper oxide (CuO_x) via a sol–gel route from copper (II) acetate monohydrate precursor with 2-methoxyethanol solvent and monoethanolamine (MEA) as chelating ligand. The temperature dependence of solution processed CuO_x properties is studied using XRD over a range 175 – 325 °C and 50 °C intervals. Two main diffraction peaks (43.5° and 50.1°) of the cubic phase of copper were obtained at 175 and 225 °C. At 275 °C, the film was oxidized to a mixture of CuO, Cu_2O, and Cu and when increasing annealing temperature to 325 °C, more Cu was oxidized, and the film is largely converted into pure CuO and peaks corresponding to Cu_2O disappeared.

Solution-processed CuO_x films with different thickness (10, 17, 21 nm) show strong absorption below 600 nm and 6% reflectance over visible wavelength with a broad absorption peak at 350 nm which seems to associate with the colour of CuO_x film (brownish appearance). The direct optical bandgap (E_g) of solution-processed CuO_x films were obtained from a linear fit of Tauc plot and found to be approximately 3.10, 2.70, and 2.65 eV for thin films of thickness 10, 17, and 21 nm respectively.

The Fermi level (E_F) of CuO_x of different thickness (10, 17, 21 nm) was measured as 4.77, 4.81, and 4.85 ± 0.02 eV respectively. The VBM was also found to be 5.06, 5.11, and 5.14 ± 0.05 eV respectively. The Fermi level (E_F) of CuO_x was found to be 0.30 eV above the valence band maximum (VBM) which indicates the p-type nature of deposited CuO_x. E_F and VBM values of the solution processed CuO_x match well with different HOMOs of donor materials and electrodes so CuO_x can be employed as efficient HTL material.

When an optimum thickness of CuO_x (17 nm) fabricated by 2-methoxyethanol was employed as a hole transport layer (anode), the V_{OC} and J_{SC} were enhanced to 0.73 V, 8.64 mA cm^{-2} respectively. Although the FF of CuO_x device (0.55) is slightly smaller than that of PEDOT:PSS device (0.57), the PCE was further increased from 3.38% for PEDOT:PSS to 3.51 ± 0.05 % for 17 nm CuO_x film.

When 17 nm CuO_x film processed by IPA was utilized as HTL, J_{SC} was decreased from 8.64 mA cm^{-2} to 7.99 mA cm^{-2} for CuO_x film processed by 2-methoxyethanol and IPA solvents respectively. The PCE was further decreased to 2.97 ± 0.05 %, which is lower than that of the reference device. This decline in J_{SC} could be attributed to the non-uniform interfacial contact between the CuOx and the active layer which contributes to lower R_s of the device and leads to a lower J_{SC} values.

The results demonstrate that the utilization of an optimum thickness CuO_x film (17 nm) processed by 2-methoxyethanol result in higher PCE than that of reference device. However, CuOx film fabricated by IPA result in lower PCE.

5 Low Temperature CuO_x via Novel Synthetic Route

5.1 Introduction

As proposed in Chapter 4, preliminary and promising results were obtained using a solution processing route for fabrication of CuO_x films, which can be a facile way to improve low- temperature processed transition metal oxides as interfacial layers in high performance OPVs. However, during studies of the impact of processing temperature on CuO_x formation, the optimum temperature was found to be 275 °C which still needs to be reduced in order to achieve the compatibility of CuO_x with low temperature processing techniques. To accomplish this goal, we need to replace copper (II) acetate precursor, which requires high annealing temperature in order to decompose and for the growth of high-quality CuO_x films.

Therefore, this chapter presents the development of low temperature solution-processed CuO_x layers prepared from copper (II) ethoxide precursor which is well known for preparation of different metal oxides such as tungsten oxide at low temperatures because of its lower decomposition temperature (120 °C).

First, optical characterization was carried out, and the optical band gap of solution-processed CuO_x is determined via Tauc plot analysis. With additional electrical characterisation, work function and valance band maximum are determined. Then X-ray photoelectron spectroscopy (XPS) helps to study the influence of annealing temperature on the deposited CuO_x films and confirms the presence of CuO_x. Moreover, solution- processed layers of CuO_x annealed at different temperatures are incorporated into bulk heterojunction OPVs and compared against control cells based on other commonly used HTL such as PEDOT:PSS. This work demonstrates the processing of CuO_x at low temperature from copper (II) ethoxide precursor and their potential as efficient hole transport layers for organic photovoltaic devices.

5.2 Growth of CuO_x Thin Film

In this work, a facile sol-gel route was utilized to obtain the solution-processed CuO_x film which was previously used for the preparation of tungsten oxide [173]. A 0.05 M of Cu (II) ethoxide (Alfa Aesar, $(Cu(OC_2H_5)_2)$ dissolved in ethanol (Aldrich, CH_3CH_2OH) with addition of a small amount of acetic acid (0.1 vol%) (Aldrich, CH_3COOH) as a stabilizer. Subsequently, the solution was first stirred at 60 °C for 1 hour then kept under constant stirring overnight at room temperature until a clear blue solution was formed. Afterwards, the precursor solution was spin-coated on the substrates at 4000 rpm for 40 sec with an acceleration of 4000 rpm/sec, followed by annealing at 150, 200, and 250 °C for 10 min on a hot plate in ambient air.

5.3 Thin Film Characterization

5.3.1 Optical Characterization

The UV-Vis-NIR transmission and reflectance spectra of solution-processed CuO_x films deposited on quartz substrates with approximate thickness (~10 ± 3nm) were investigated in 220–1200 nm wavelength range as a function of annealing temperature (150, 200, and 250 °C), against an air reference, as shown in Figure 5.1(a). Then the absorbance was calculated in order to determine the optical bandgap of deposited CuO_x films using Tauc analysis.

The transmittance spectra show a variation for different annealing temperature. All films show high transmittance over NIR region. Then, the transmission start to fall around 600 nm for all films agreeing with literature that explains the strong absorption of copper oxide film below 600nm [232]. The reflectance is also influenced by annealing temperature. The reflectance spectra for samples with different temperatures are almost same and indicates 7% reflectance over visible wavelength and the reflectance will increase slightly by increasing annealing temperature.

It is also noted that the absorbance for ultraviolet region is higher than visible region and NIR (600-1200 nm). Furthermore, the brownish colour of CuO_x films annealed at 200 and 250 ˚C is attributed to the broad absorption peak at 350 nm as the film absorbance depends on the corresponding wavelength. However, this colour was apparent for the film annealed at 150 ˚C as shown in **Figure 5.1**(b).

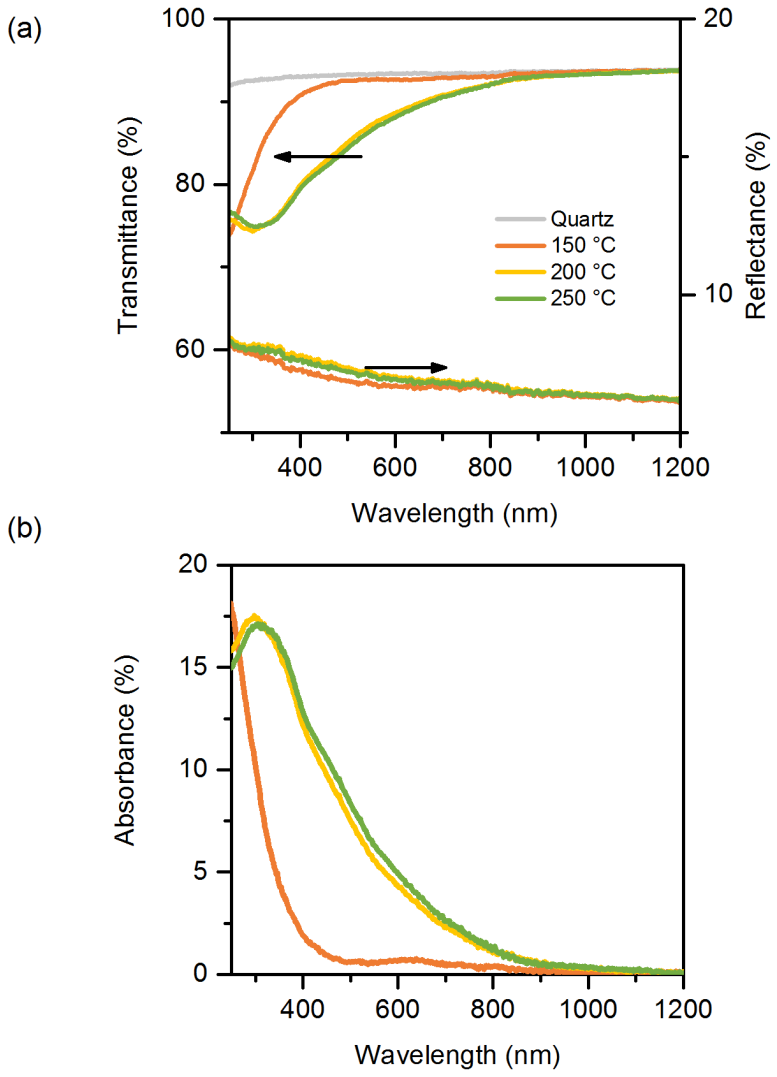

Figure 5.1 (a) Transmittance and reflectance spectra of CuO_x films annealed at different temperatures 150, 200, 250 ˚C, (b) Absorbance spectra of the deposited films on quartz substrate.

The direct optical band gap (E_g) of solution-processed CuO_x films was obtained from a linear fit of Tauc plot and found to be approximately 3.60, 2.70, and 2.62 eV for films annealed at 150, 200, and 250 °C respectively as shown in **Figure 5.2**. These results show that solution- processed CuO_x has a wide band gap. We observe larger band gap at 150 °C and the measured band gap for 200 and 250 °C are closer to the literature values (2.60 eV) [140]. This shows the transition from precursor to oxide as annealing temperature increases from 150 to 250 °C.

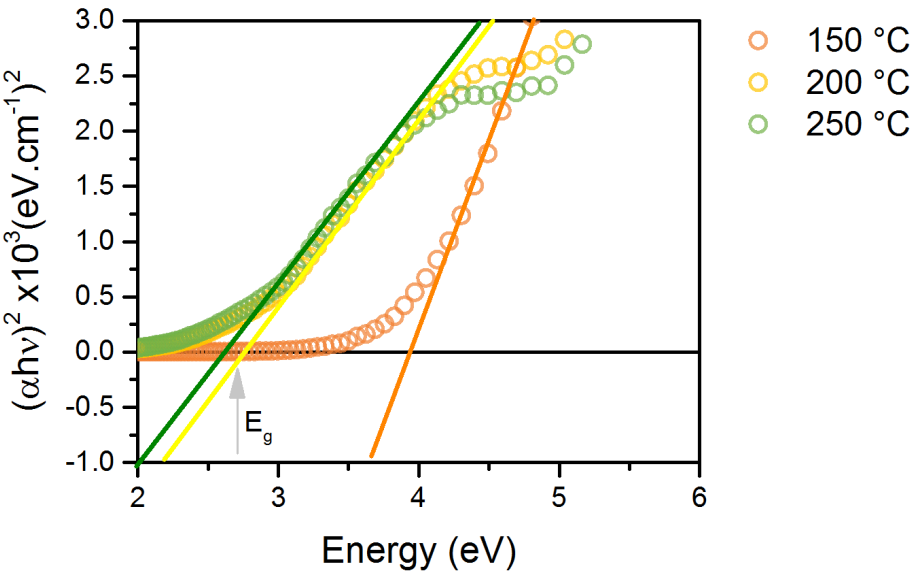

Figure 5.2 Tauc plot of solution-processed CuO_x films annealed at varying temperatures 150, 200, 250 ˚C. $(\alpha h\nu)^2$ is calculated from the absorption coefficients of the CuO_x films.

5.3.2 Electronic properties of CuO_x thin films

Kelvin Probe (KP) and Air Photoemission Spectroscopy (APS) measurements were used to determine the energetics of solution-processed CuO_x such as the Fermi level (E_F) and the valence band maximum (VBM) as shown in **Figure 5.3** Different sets of CuO_x films were spin- cast on ITO substrates and annealed at different temperatures, 150, 200, and 250 °C, in ambient air.

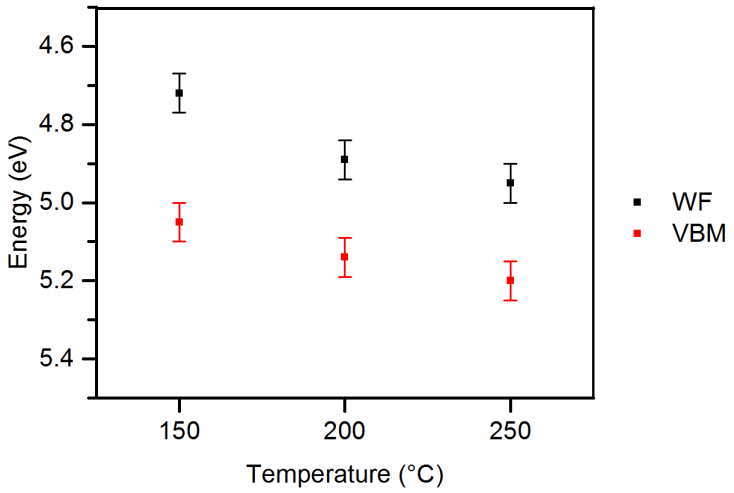

Figure 5.3 The work-function (WF) and the valance band maximum (VBM) measurements for CuO_x films annealed at different temperature (150, 200, 250 ˚C) for 10 minutes in air.

The Fermi level (E_F) of CuO_x was found to be 4.72, 4.89, and 4.95 (± 0.02) eV for CuO_x films annealed at 150, 200, and 250 °C respectively showing a significant dependence on the annealing temperature. The valence band maximum (VBM) values were extracted from the linear fit the photoemission spectra and was found to be 5.06, 5.14, and 5.20 (± 0.05) eV respectively. The Fermi level (E_F) of CuO_x was found to be 0.25 eV above the valence band maximum (VBM) which is in a good agreement with the literature [149].

By measuring the optical band gap (Eg) [2.62 – 2.70 (± 0.01) eV], VBM [5.14 – 5.20 (± 0.05) eV], and E_F which is estimated in the range [4.89 – 4.95 ± (0.02) eV] as lying ~ 0.25 eV above VBM, the energy levels diagram of solution-processed CuO_x can be constructed as shown in **Figure 5.4**.

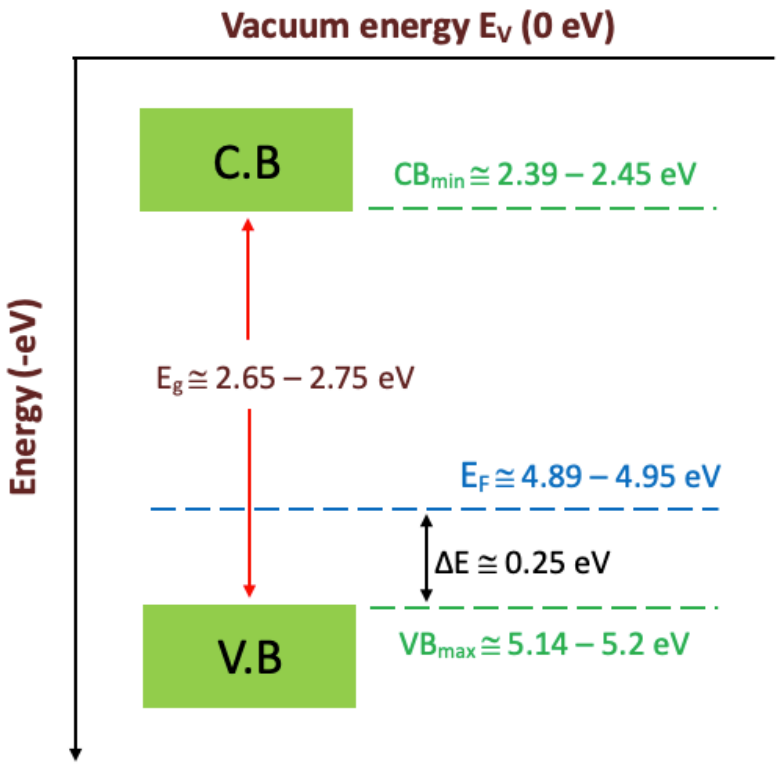

Figure 5.4 A schematic diagram of electronic energy levels of solution processed CuO_x including valence band maximum (VBM), optical band gap (E_g), and Fermi level (E_F).

The obtained results indicate the p-type nature of CuO_x film and show the potential and compatibility of the solution processed CuO_x to be employed as HTL material because its Fermi level (E_F) and valence band maximum (VBM) values match well with the work function (WF) of common electrodes materials and HOMO of different donor materials.

5.3.3 Microstructural Analysis of CuO_x thin Film

After the optoelectronic identification of the deposited CuO_x films, X-ray photoelectron spectroscopy (XPS) measurement was performed to further understand the impact of annealing temperature on the chemical composition of the CuO_x films. All XPS spectra are charge-corrected by the C 1s spectra, assuming an unchanged C-C single bond at peak position of 284.8 eV [252]. A survey scan is firstly taken to identify the overall chemical environment of the resulting sample. The characteristic peaks of the elements Cu, O, and C are indicated in the survey scan (Figure 5.5).

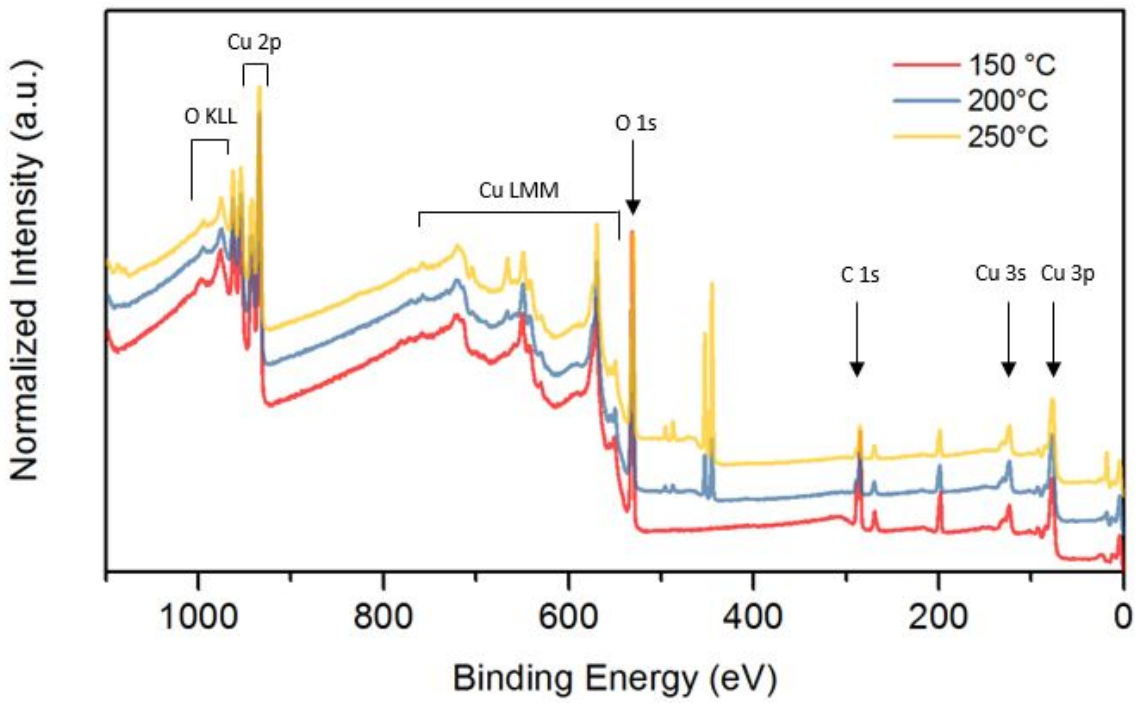

Figure 5.5 Survey spectra of CuO_x film annealed at different temperatures. Core levels and Auger lines of C, O, and Cu are labelled.

Regarding the relationship between sample geometry and spectral background signal, all spectra show a downward bending in background at binding energy higher than 1000 eV, which indicates a planer nature of the sample geometry. From a planar surface, electrons will less likely to be obstructed by the overhanging structure (inelastically scattered), and therefore a less proportion of electron signals will contribute to the background level.

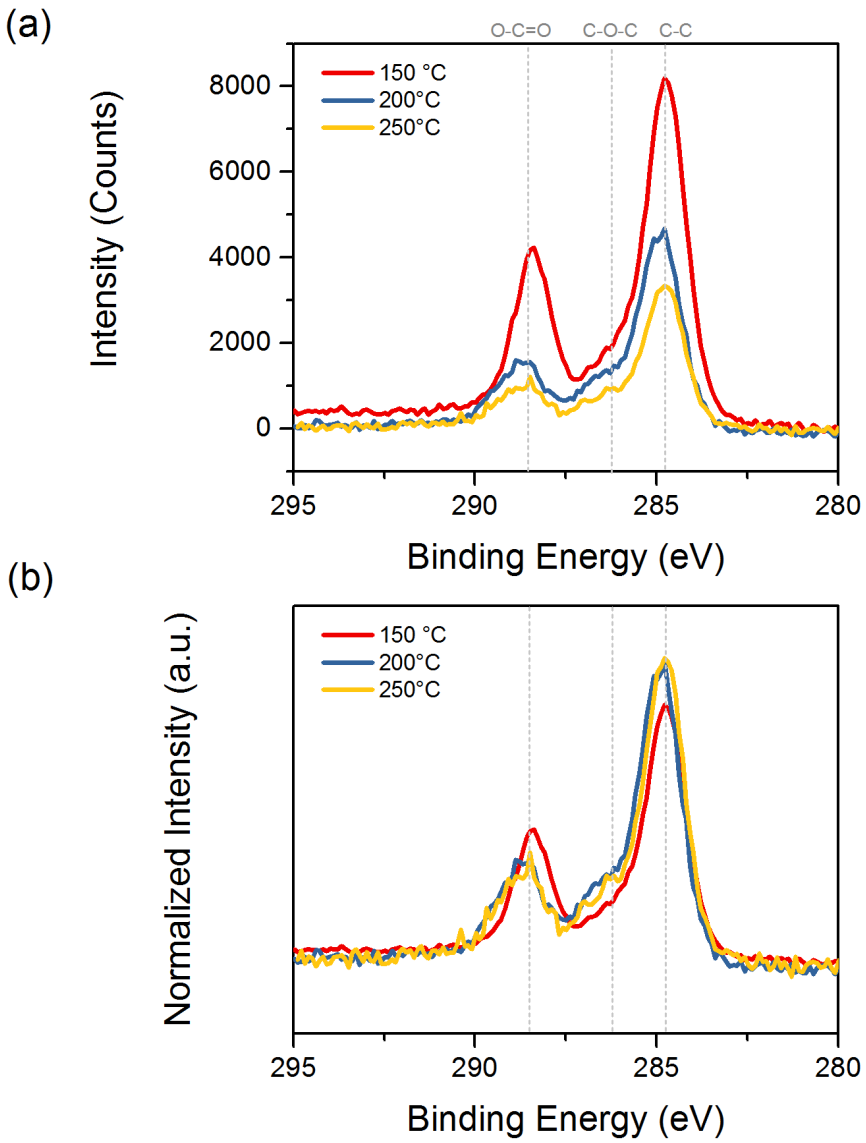

Figure 5.6 C 1s spectra of annealed CuO_x, a) raw data and b) normalised by area.

C 1s spectra are significantly influenced by the annealing temperature so to review the impact of annealing process, C 1s spectra before and after normalization are discussed. Before normalization, signal intensity between spectra is directly proportional to the number of carbon atoms escaped from the sample surface. If assuming all samples share the same probability of electrons escaping from the surface, a decline in C 1s peak intensity would indicate a decline in number of carbon atoms. In Figure 5.6 we observe a continuous decline in C 1s peak as annealing temperature increases from 150 to 250 °C, which shows the progress of evaporation of solvents and the thermal decomposition of precursor functional groups.

We can attribute all three species presented in C 1s spectra to the precursor, namely Cu(II) ethoxide ($Cu(OC_2H_5)_2$) and ethanol (CH_3CH_2OH) and acetic acid (CH_3COOH). According to the decomposition temperature of Alkoxide precursors (125 °C) [253], as the annealing temperature increases above 150 °C, the loss of the precursor functional group O-C=C corresponds to the decline of the higher binding energy term in C 1s spectra [254].

After normalization, the information with peak intensity is lost but the difference in peak shape reveals the difference in the ratio between the peak in the lower and higher binding energy. This implies that different carbon species (functional groups) are lost at different temperatures.

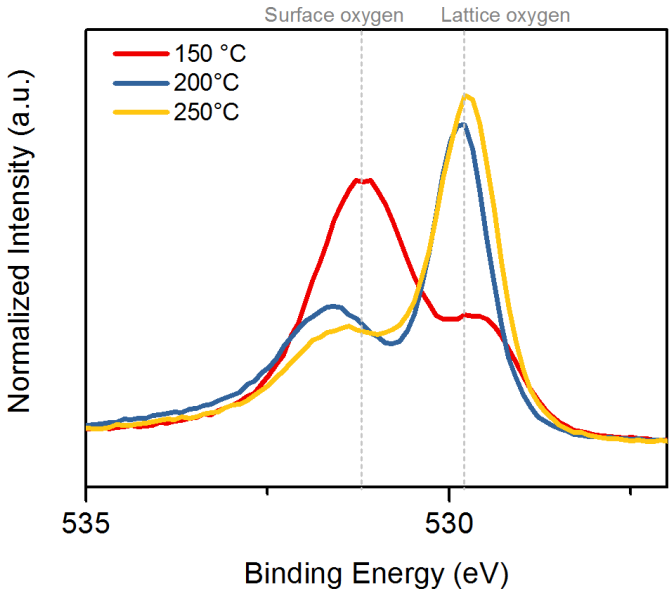

Figure 5.7 O 1s spectra of samples annealed at 150 – 250 °C.

As extensively discussed in the literature, the two peaks in O 1s spectrum can be attributed broadly to oxide lattice oxygen (the component at lower binding energy) and the surface oxygen (the component at higher binding energy) as shown in **Figure 5.7** .Typically, the surface oxygen peak involves species as surface hydroxide and water adsorbed to the surface. As annealing temperature increases, we see a significant development in the lattice oxygen component, an indicative of higher presence of copper oxide.

As annealing temperature increases from 150 to 250 °C, there is a systematic decline in the intensity of the surface oxygen, as well as a significant development of lattice oxygen. The decline in surface oxygen species shows the progress in the post annealing, where dehydration and thermal decomposition of the precursor takes place. This observation is in agreement with signal of C 1s peaks, in which the carbon content (predominantly from the precursor) continues to decline upon annealing.

It is also clearly noted that the oxide peaks shift 0.3 eV towards the higher binding energy as annealing temperature increases from 150 to 250 °C. This indicates a shift in the Fermi level position, which relates to the increase in the work function of CuO_x as annealing temperature increases [230].

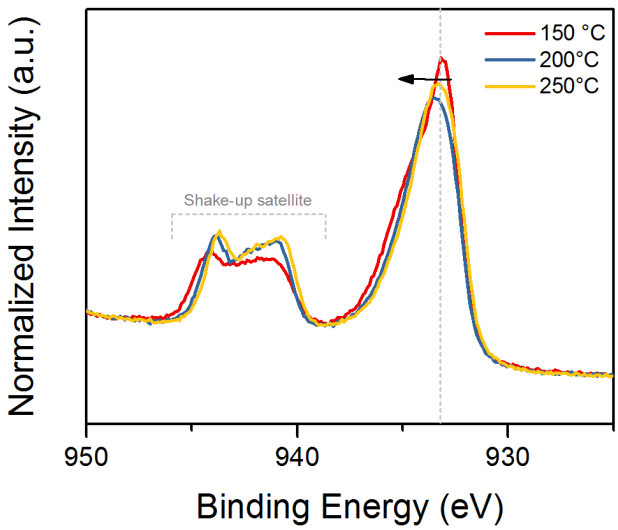

Figure 5.8 Cu $2p_{3/2}$ spectra of CuO_x sampels annealed at different temperatures.

When referring to cu $2P_{3/2}$ spectra in **Figure 5.8**, we observe similar peak shape in all annealing temperature. Judging from the change in electronic structure from 150 to 250 °C, it is more likely that the copper species at 150 °C is not CuO but it is evidently Cu^{+2} [255] which is correlated with the oxidation state of Cu in the alkoxide precursor. This is also consistent with the observation of a Cu 2p1/2 peak and its satellite at 953 and 960 eV respectively (data not shown).

For Auger spectra, it is more practical to compare the overall shape of peaks with respect to reference rather than peak fitting when interpreting for Cu species. Therefore, in this case we selected two reference peaks measured by Biesinger et al for both Cu_2O and CuO [256].

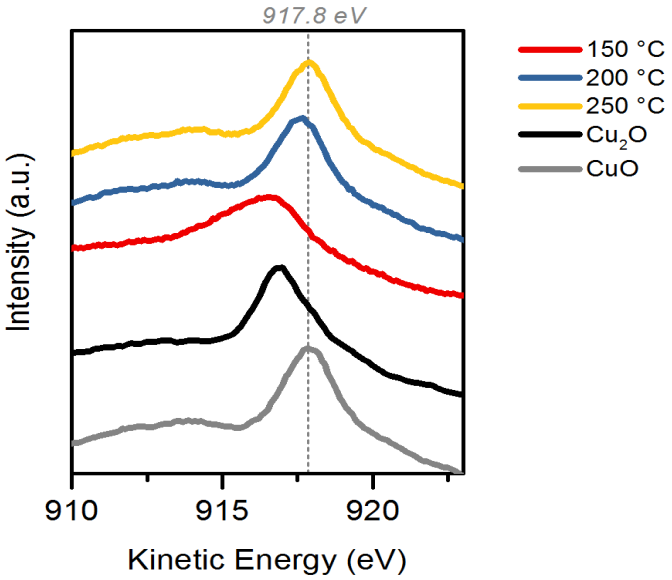

Figure 5.9 Cu LMM Auger spectra for CuO_x films annealed at various temperatures. A reference spectrum of CuO and Cu_2O are included for comparison.

Figure 5.9 presents a comparison between CuO_x samples annealed at different temperatures and CuO and Cu_2O references. From the figure we see an enhancement in the peak at 917.8 eV when annealed at 200 and 250 °C and this peak correspond well to the shape and position of CuO. The peak of 150 °C does not show a significant presence of CuO. On the other hand, Cu_2O shows a similar shape and position to 150 °C as at lower temperature, hence it is possible that Cu_2O was formed at 150 °C and became fully oxidized to CuO at higher temperatures.

5.4 OPV fabrication and characterization

In order to demonstrate the influence of annealing temperature of CuO_x films on device performance, organic solar cells were fabricated using CuO_x as anode buffer layers (HTLs) and compared with and PEDOT:PSS as a reference. OPVs based on P3HT:ICBA blend with a conventional device structure of ITO/CuO_x or PEDOT:PSS/ P3HT:ICBA /Ca/Al were fabricated as shown in **Figure 5.10**. PEDOT:PSS and BHJ blend (P3HT:ICBA) were processed as described in chapter 4 in addition to three CuO_x films were fabricated by spin coating of precursor solution on substrates at 4000 rpm for 40 sec with an acceleration of 4000 rpm/sec, followed by annealing at 150, 200, and 250 °C for 10 min on a hot plate in air.

All devices were completed by the thermal evaporation of a 10 nm thick layer of calcium at deposition rate of 0.5 $Å s^{-1}$ followed by evaporation of a 70-80 nm thick layer of aluminium electrode at rate of 1.5 $Å s^{-1}$, through shadow masks at a base pressure of 5×10^{-6} mbar. The device pixel area was determined by the spatial overlap of the ITO strip and aluminium electrodes (4.5 mm^2). The BHJ solar cell structure and energy levels of different materials used in fabrication of OPV are shown in **Figure 5.10**.

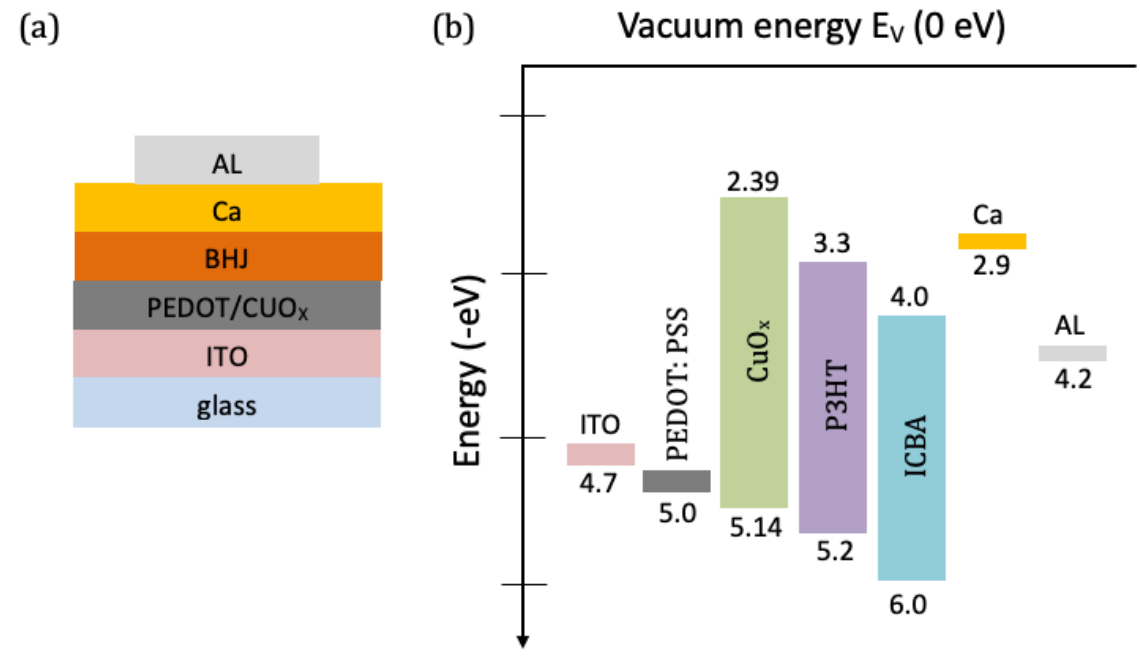

.

Figure 5.10 (a) A Schematic of conventional structure BHJ solar cell employed with CuO_x and PEDOT:PSS HTLs. (b) Energetics of the different materials used in OPV.

The typical J–V characteristics of the devices with PEDOT:PSS and CuO_x annealed at different temperature (150, 200, 250 °C) and tested under the illumination of AM 1.5G, are shown in **Figure 5.11**, and the device parameters (open circuit voltage (V_{OC}), short circuit current density (J_{SC}), fill factor (FF), series resistance (R_s) and shunt resistance (R_{sh}) are summarized in **Figure 5.12**.

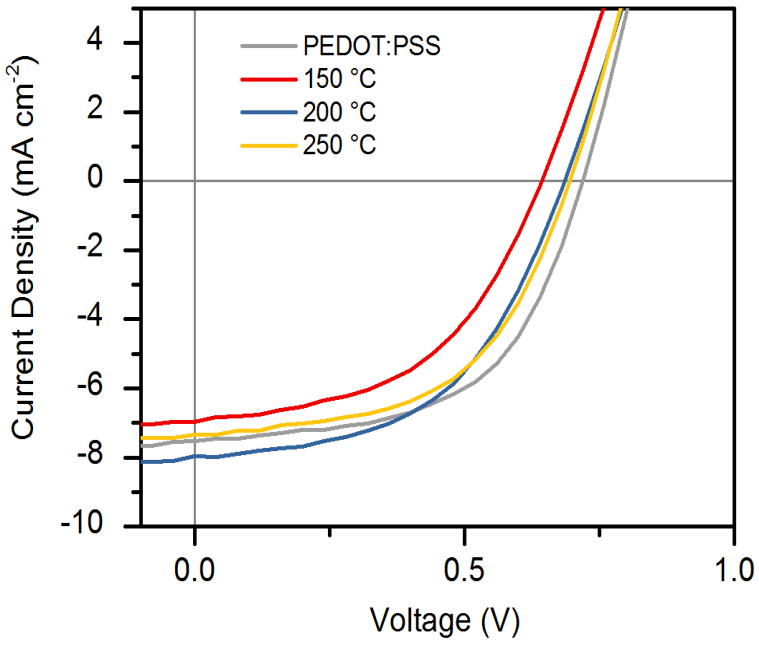

Figure 5.11 J-V curves measured under illumination of simulated solar light for conventional architecture P3HT:ICBA OPVs with PEDOT:PSS as a reference and CuO_x layers annealed at different temperatures 150, 200, 250 °C.

It is clear that the processing temperature of CuO_x plays an important role in device performance. The device based on CuO_x annealed at 150 °C has a poor PCE of 2.31%, V_{OC} of 0.64 V, J_{SC} of 6.96 mA cm^{-2} and FF of 0.48. When the annealing temperature was increased to 200 °C, PCE was significantly improved to 2.81%, with V_{OC} of 0.68 V, J_{SC} of 7.96 mA cm^{-2} and FF of 0.68. If the temperature was further increased to 250 °C, V_{OC} was slightly increased to 0.69 V and FF also increased to 0.53. However, J_{SC} was slightly decreased to 7.33 mA cm^{-2}, and thus the PCE of the device based on the CuO_x film annealed at 250 °C was marginally decreased to 2.74%. The PCE of the device based on the CuO_x annealed at 200 °C is comparable to that of the device with the PEDOT:PSS anode buffer layer (PCE of 3.02%).

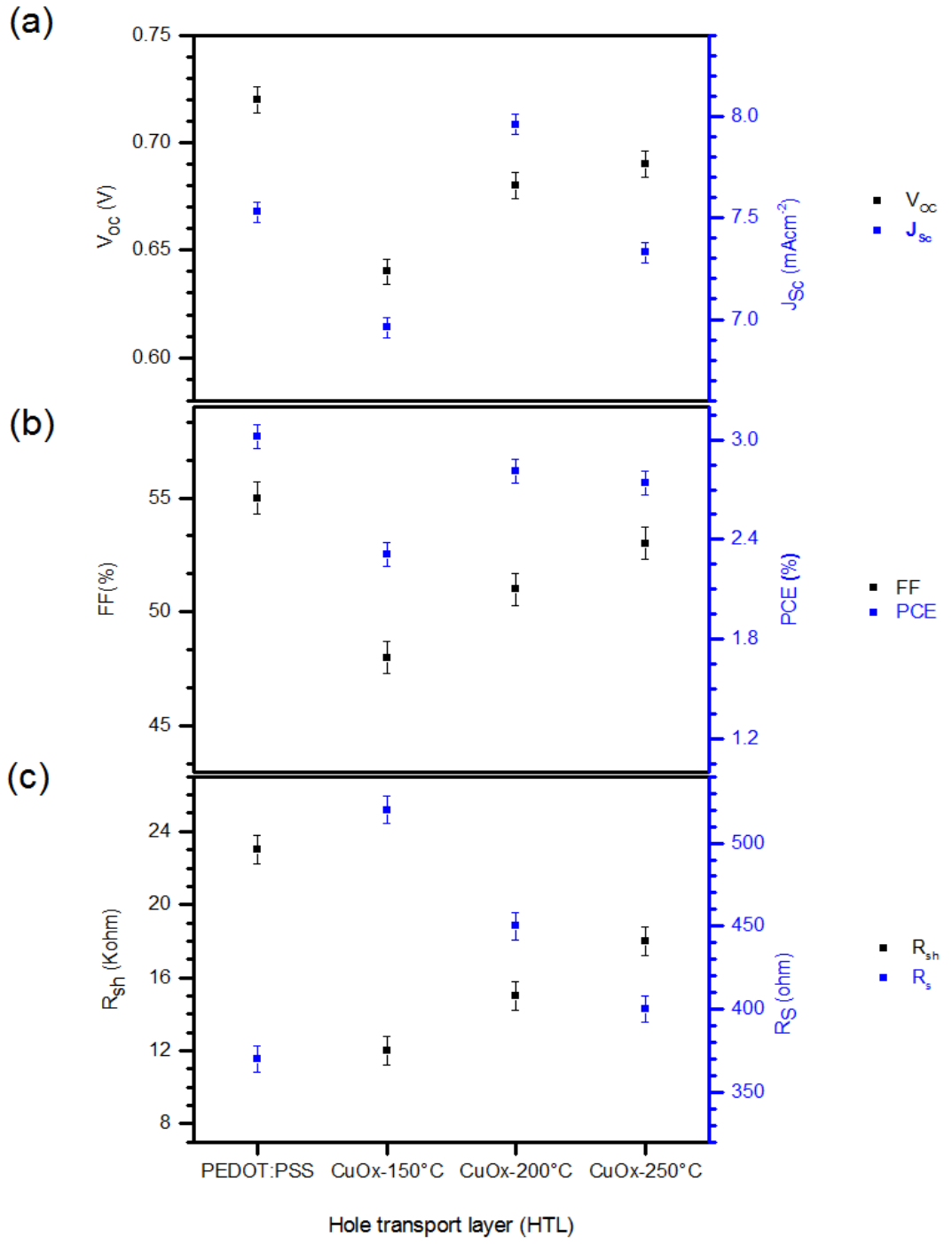

Figure 5.12 The measured device characteristics for OPVs (3 devices for each temperature) based on P3HT:ICBA as active layer with PEDOT:PSS and CuOx annealed at 150, 200, 250 °C as HTLs, measured under AM1.5 simulated solar illumination. (a) Open circuit voltage (VOC) and short circuit current density (J_{SC}). (b) Fill factor (FF) and power conversion efficiency (PCE). (c) Shunt resistance (R_{sh}) and series resistance (R_S).

The increased J_{SC} of the CuO_x devices can be attributed to the enhanced charge collection and transport at the CuO_x/P3HT interface, which benefits from the high WF of CuOx anode buffer layer and the formation of an Ohmic contact. In addition to the higher transparency of CuO_x than that of PEDOT:PSS. The increased FF of the CuO_x based devices as temperature increases could ascribed to the decrease in R_s and increased R_{sh} of CuO_x film which can reduce leakage current and result in higher FF [239].

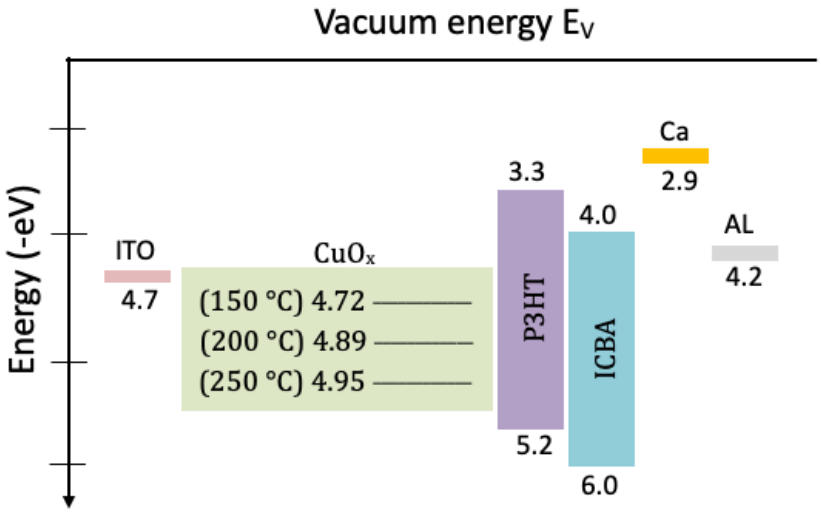

Figure 5.13 A schematic diagram showing the energy levels of various materials used in OPV device and the work function values of CuO_x films annealed at different temperatures (150, 200, 250 °C).

In order to understand the impact of processing temperature of CuO_x films on device performance **Figure 5.13** shows the band energy diagram of the substances used in OPV devices, in which the work function of CuO_x films measured by Kelvin probe. There is an increase in the measured WF of almost 0.2 eV as temperature increases. This enhances the built-in electric field across the device and improves movement of photo-generated electrons toward CuO_x, which consequently increases the V_{OC} slightly from 0.64 V (150 °C) to 0.68 V (250 °C). Therefore, the enhanced V_{OC} could be ascribed to the improved quality of CuO_x and decrease the contact resistance at the CuO_x/P3HT interface [257].

5.5 Conclusions

In summary, we have successfully demonstrated solution-processed copper oxide (CuO_x) via a facile sol-gel route at low temperature from a 0.05 M of Copper (II) ethoxide precursor dissolved in ethanol with addition of a small amount of acetic acid (0.1 %vol) as a stabilizer.

The optical properties of solution-processed CuO_x films (~10±3nm) were investigated as a function of annealing temperature (150, 200, and 250 °C). The direct optical bandgap (E_g) of CuO_x films were obtained from a linear fit of Tauc plot and found to be ~ 3.60, 2.70, and 2.62 eV for films annealed at 150, 200, and 250 °C respectively. The band gap calculated for CuO_x film annealed at 200, and 250 °C can be considered as Cu_2O phase but for 150 °C, the band gap 3.6 eV is larger than theoretical values. The Fermi level (E_F) of CuOx was found to be 4.72, 4.89, and 4.95 (± 0.02) eV for films annealed at 150, 200, and 250 °C respectively showing a significant dependence on the annealing temperature. The valence band maximum (VBM) values was found to be 5.06, 5.14, and 5.20 (± 0.05) eV respectively. The Fermi level (E_F) of CuO_x was found to be 0.25 eV above the valence band maximum (VBM) which is in a good agreement with the literature.

The impact of annealing temperature on the chemical composition of the CuO_x films was studied using X-ray photoelectron spectroscopy (XPS) measurements. The characteristic peaks of Cu, O, and C are indicated in the survey scan. We observe a continuous decline in C 1s peak as annealing temperature increases from 150 to 250 °C, which shows the progress of evaporation of solvents and the thermal decomposition of precursor functional groups. Furthermore, as annealing temperature increases, we see a significant development in the lattice oxygen component and a systematic decline in the intensity of the surface oxygen, an indicative of higher presence of copper oxide.

The position of oxide peaks shifts 0.30 eV from lower to higher binding energy upon annealing from 150 to 250 °C, which relates to the increase in the work function of CuO_x as annealing temperature increases. Auger spectra shows an enhancement in the peak at 917.8 eV when annealed at 200 and 250 °C which correspond well to the shape and position of CuO. The peak of 150 °C does not show a significant presence of CuO.

The device based on CuO_x annealed at 150 °C has a poor PCE of 2.31%, V_{OC} of 0.64 V, J_{SC} of 6.96 mA cm^{-2} and FF of 0.48. When temperature was increased to 200 °C, PCE was significantly improved to 2.81%, with V_{OC} of 0.68 V, J_{SC} of 7.96 mA cm^{-2} and FF of 0.68. If the temperature was further increased to 250 °C, V_{OC} was slightly increased to 0.69 V and FF also increased to 0.53. However, J_{SC} was slightly decreased to 7.33 mA cm^{-2}, and thus the PCE of the device based on the CuO_x film annealed at 250 °C was marginally decreased to 2.74%. The PCE of the device based on the CuO_x annealed at 200 °C is comparable to that of the device with the PEDOT:PSS anode buffer layer (PCE of 3.02%).

The enhanced V_{OC} and J_{SC} can be attributed to the increase in the measured WF of as temperature increases which forms an Ohmic contact and improves the charge collection at the CuO_x/P3HT interface. As temperature increases, R_s decreases and R_{sh} increases which can reduce leakage current and result in higher FF.

6 Conclusions and Outlook

In this work, we proposed different methodologies to address some of the current challenges limit the performance of organic photovoltaics based on fabrication of P-type metal oxides such as CuO_x and NiO_x, by solution processing at low-temperature in ambient or prepared by thermal evaporation in vacuum. The primary purpose of this chapter is to summarise the key results that have been reported in the previous chapters as well as to discuss the future prospects for research in this field.

6.1 Conclusions

Starting with Chapter 3, the thermal evaporation of controlled thickness, high optical quality NiO_x films was successfully demonstrated for the first time according to literature. It was anticipated that the films would exhibit p-type *i.e.* hole selective transport, however we show that those prepared are n-type in nature. Firstly, evaporated films of different thickness (5, 7, 10, 20 nm) were employed as electron transport layers (ETLs) in BHJ OPVs in order to determine the optimum thickness which was identified to be 10 nm. The device with the optimum ETL thickness showed PCE of 2.86 ± 0.05% with V_{OC} of 0.72 V, J_{SC} of 8.63 mA cm^{-2} and FF of 0.46. However, OPVs with ZnO ETL exhibited PCE of 3.29 ± 0.05% with V_{OC} of 0.77 V, J_{SC} of 10.3 mA cm^{-2} and FF of 0.43.

X-ray photoemission spectroscopy (XPS) measurements were carried out for NiO_x films of 10 nm thickness in order to investigate the elemental composition and to understand the reasons of n-type nature of the evaporated films. Ni and W both showed dominating peaks across the survey spectra. The ratio between nickel and tungsten is calculated and his existence of W- peaks explains the n-type nature of the evaporated films.

Subsequently, the impact of W:Ni ratio on the device performance was investigated by incorporation of 10 nm thick films of various W:Ni ratio (10, 13, 20, 25%). The device with the optimum (W:Ni ratio, 20 at%) ETL showed a PCE of 2.9 ± 0.05% with V_{OC} of 0.72 V, J_{SC} of 8.63 mA cm^{-2} and FF of 0.46. However, OPVs with ZnO ETL exhibited PCE of 3.3 ± 0.05% with V_{OC} of 0.76 V, J_{SC} of 10.2 mA cm^{-2} and FF of 0.43. The J_{SC} and V_{OC} of ZnO ETL are higher than that of evaporated film because of the better energy level alignment of ZnO with the active layer than that of evaporated film which improve the contact at ETL/BHJ interface.

However, the FF of evaporated film is higher than that of ZnO and this because thermal evaporation provides uniform layers with precise thickness.

The potential of thermally evaporated films of 10 nm and 20 at% W:Ni ratio as a universal ETL was investigated by fabrication of inverted BHJ OPVs with three different active layers, namely, (PTB7:$PC_{71}BM$), (PBDB-T:ITIC), and (PFBDB-T:C8-ITIC). Notably, J_{SC} of OPV devices based on both ZnO and evaporated W:Ni show approximately similar values. However, V_{OC} of evaporated films is lower than that of ZnO for the three devices and this indicates an unfavourable energy level alignment between the work function of evaporated film and LUMO of acceptors.

In chapter 4, solution-processed copper oxide (CuO_x) was successfully demonstrated via a sol–gel route from copper (II) acetate monohydrate precursor with 2-methoxyethanol or isopropanol (IPA) solvents and small amount of monoethanolamine (MEA) as a stabilizer. The primary focus of this chapter was to study the thermal decomposition of precursor using XRD over a range 175 – 325 °C and 50 °C intervals. Diffraction peaks of the cubic phase of copper (43.5° and 50.1°) were obtained at 175 and 225 °C. As temperature increased to 275 °C, the film was oxidized to a mixture of CuO, Cu_2O, and Cu and when temperature further increased to 325 °C, more Cu was oxidized, and the film is largely converted into pure CuO.

The direct optical bandgap (E_g) were found to be ~ 3.10, 2.70, and 2.65 eV for 10, 17, and 21 nm thick films respectively. The Fermi level (E_F) was measured as 4.77, 4.81, and 4.85 ± 0.02 eV and the valence band maximum (VBM) was found to be 5.06, 5.11, and 5.14 (± 0.05) eV for different thickness 10, 17, 21 nm respectively. E_F of CuO_x which was dependent on film thickness was found to be 0.3 eV above VBM which is in a good agreement with the literature. The obtained results indicate the potential of the processed CuOx to be employed as HTL material as its work function matches well with different HOMOs of donor materials.

Upon utilization an optimum thickness of CuO_x (17 nm) fabricated by 2-methoxyethanol as anode buffer layer, the Voc and Jsc were enhanced to 0.73 V and 8.64 mA cm^{-2} respectively. Although the FF of CuO_x device (0.55) was slightly smaller than that of PEDOT:PSS

device, the PCE was further increased to 3.51 ± 0.05 %, which is 4 % higher than that of the reference device. However, when CuO_x (17 nm) films were processed by IPA solvent, J_{sc} and PCE were decreased to 7.99 mA cm^{-2} and 2.97 ± 0.05 % respectively, which are lower than that of the reference device. This decline was ascribed to the non-uniform interfacial contact between the CuO_x processed by IPA and the active layer which contributes to lower Rs leading to lower J_{SC}. The results demonstrate that the integration of 17 nm CuO_x film processed by 2-methoxyethanol result in higher PCE than that of reference device. However, CuO_x film fabricated by IPA result in lower PCE.

Finally, the solution process of CuO_x films demonstrated in chapter 4 has been further explored in chapter 5 with introducing a novel synthetic route based on copper (II) ethoxide precursor instead of Copper (II) acetate. In this approach, a 0.05 M of Copper (II) ethoxide precursor dissolved in ethanol with addition of 0.1 %vol acetic acid as a stabilizer. The direct optical bandgap of CuO_x films was found to be ~ 3.60, 2.70, and 2.62 eV for films annealed at 150, 200, and 250 °C respectively. In addition, the Fermi level (E_F) of CuO_x was found to be ~ 4.72, 4.89, and 4.95 (± 0.02) eV for films annealed at 150, 200, and 250 °C respectively showing a significant dependence on the annealing temperature. The valence band maximum (VBM) values was found to be ~ 5.06, 5.14, and 5.20 (± 0.05) eV respectively. The Fermi level (E_F) of CuO_x was found to be 0.25 eV above the valence band maximum (VBM) which is in a good agreement with the literature.

The influence of annealing temperature on the chemical composition of the CuO_x films was investigated using XPS measurements. The characteristic peaks of the elements Cu, O, and C are found in the survey scan. C 1s peak shows a continuous decline as annealing temperature increases from 150 to 250 °C, which indicates the thermal decomposition of precursor's functional groups and the evaporation of solvents. Furthermore, as annealing temperature increases, there was a significant enhancement in the lattice oxygen and a systematic decline in the surface oxygen, an indicative of higher presence of copper oxide. It was also noted that the position of oxide peaks shifts 0.3 eV from lower to higher binding energy upon annealing from 150 to 250 °C. This indicates a shift in the Fermi level position. Auger spectra shows an enhancement in the peak at 917.8 eV when annealed at 200 and 250 °C which correspond well to the shape and position of CuO.

The device based on CuO_x annealed at 150 °C has a poor PCE of 2.31%, V_{OC} of 0.64 V, J_{SC} of 6.96 mA cm^{-2} and FF of 0.48. When the annealing temperature was increased to 200 °C, PCE was significantly improved to 2.81%, with V_{OC} of 0.68 V, J_{SC} of 7.96 mA cm^{-2} and FF of 0.68. When the temperature was further increased to 250 °C, V_{OC} and FF were slightly increased to 0.69 V and 0.53 respectively. However, J_{SC} and PCE were marginally decreased to 7.33 mA cm^{-2} and 2.74% respectively. The enhanced V_{OC} and J_{SC} can be attributed to the increase in the measured WF as temperature increases which forms an Ohmic contact and improves the charge collection at the CuO_x/P3HT interface. As temperature increases, R_s decreases and R_{sh} increases which can reduce leakage current and result in higher FF. The results demonstrate that the incorporation of CuOx annealed at 200 °C result in a comparable PCE (2.81%) to that of reference device with PEDOT:PSS anode buffer layer (PCE of 3.02%).

6.2 Outlook

Following to the work that has been carried out in this thesis, further characterization techniques can be considered to obtain a comprehensive study of the electronic structure of the thermally evaporated NiO_x films. Ultraviolet photoemission spectroscopy (UPS) and advanced measurements by x-ray photoemission spectroscopy (XPS) can be utilized in order to measure the valence band, conduction band and the work function of the evaporated film. These measurements will allow us to investigate the energy levels alignment at the interface between evaporated NiO_x films and BHJ and also to study the factors causing lower V_{OC} for devices fabricated from evaporated NiO_x compared with ZnO based devices.

Furthermore, extensive research has been focused on doping of NiO by other metals such as Li and Cu in order to improve its conductivity. In this work, we found that it likely to change the function of NiO from hole transport layer to electron transport layer by doping approach with other metals such as tungsten. Therefore, doping NiO by tungsten using different methodologies such as sputtering, or solution process can be considered with the appropriate concentrations and the suitable processing conditions. This study will give a comprehensive analysis of the obtained results.

The potential of solution processed CuO_x as a hole transport layer (HTL) was investigated by different precursors such as Cu(II) acetate and ethoxide. These precursors can be further optimized by replacing the solvent or annealing at different temperature in different environments. In addition, there are some novel precursors being used for preparation of other oxides such as MoO_3 and WO_3 but have not been used for CuO_x. Therefore, further studies are needed to understand the decomposition process of these novel precursors.

7 References

1. https://www.iea.org/reports/world-energy-outlook2019/renewables#abstract http://www.iea.org/textbase/npsum/weo2015sum.pdf, (accessed: February 2020), The International Energy Agency (IEA)'s Annual World Energy Outlook (2020).
2. https://en.wikipedia.org/wiki/Solar_energy, (accessed: February 2020).
3. https://www.bp.com/en/global/corporate/energy-economics/statistical-review-of-world-energy.html. BP Statistical Review of World Energy 2019 | 68th edition, (accessed: February 2020).
4. Praveen Kumar, M., Prabhakar, T. Solar Photovoltaic Technology—A Review. Advanced Science, Engineering and Medicine, 2020, 12(1), 5-10(6).
5. Becquerel, A. Memoire sur les effects d'electriques produits sous l'influence des rayons solaires. Comptes Rendus de l'Academie des Sciences, 1839, 9, 561–567.
6. Einstein, A. Über einen die Erzeugung und Verwandlung des Lichtes betreffenden heuristischen Gesichtspunkt. Annalen der Physik (in German), 1905, 17 (6): 132–148.
7. Chapin, D., Fuller, C., & Pearson, G. A new silicon p-n junction photocell for converting solar radiation into electrical power. Journal of Applied Physics, 1954, 25 (5), 676–677.
8. Green, M., Dunlop, E., Hohl-Ebinger, J., Yoshita, M., Kopidakis, N., & Ho-Baillie, A. Solar cell efficiency tables (Version 55), Progress in Photovoltaics: Res Appl., 2020, 28, 3–15.
9. Green, M. Commercial progress and challenges for photovoltaics. Nature Energy, 2016, 1.
10. Ansari, M., Qurashi, A., & Nazeeruddin, M. Frontiers, opportunities, and challenges in perovskite solar cells: A critical review. Journal of Photochemistry and Photobiology C: Photochemistry Reviews, 2018, 35, 1–24.
11. Smith, D., Cousins, P., Masad, A., Waldhauer, A., Westerberg, S., Johnson, M., Tu, X., Dennis, T., Harley, G., Solomon, G., Rim, S., Shepherd, M., Harrington, S., Defensor, M., Leygo, A., Tomada, P., Wu, J., Pass, T., Ann, L., Smith, L., Bergstrom, N., Nicdao, C., Tipones, P., Vicente, D. Generation III high efficiency lower cost technology: Transition to full scale manufacturing. 38th IEEE Photovoltaic Specialists Conference, IEEE, 2012, 1594–1597.
12. Shockley, W., & Queisser, H., Detailed Balance Limit of Efficiency of p-n Junction Solar Cells. Journal of Applied Physics. 1961, 32, 510.

13. Arora, N., R. Hauser, J., Roulston, D. Electron and hole mobilities in silicon as a function of concentration and temperature. IEEE Transactions on Electron Devices 1982, 29 (2), 292-295.
14. Green, M., & Bremner, S. Energy conversion approaches and materials for high-efficiency photovoltaics. Nature Materials, 2017, 16, 23-34.
15. Yan, C., Huang, J., Sun, K., Johnston, S., Zhang, Y., Sun, H., & et al. Cu2ZnSnS4 solar cells with over 10% power conversion efficiency enabled by heterojunction heat treatment, Nature Energy, 2018, 3, 764–772.
16. Grätzel, M. Photoelectrochemical cells. Nature, 2001, 414, 338-344.
17. Nazeeruddin, M., Key, A., Rodicio, I., Humphry-Baker, R., Mueller, E., Liska, P., Vlachopoulos, N., & Graetzel, M. Conversion of light to electricity by cis-x2bis(2,2'-bipyridyl-4,4'-dicarboxylate)ruthenium(II) charge-transfer sensitizers (X= Cl-, Br-, I-, CN-, and SCN-) on nanocrystalline titanium dioxide electrodes, Journal Of The American Chemical Society. 1993, 115, 6382-6390.
18. Huynh, W., Dittmer, J., & Alivisatos, A. Hybrid nanorodpolymer solar cells, Science, 2002, 295, 2425.
19. Gur, I., Fromer, N., Geier, M., & Alivisatos, A. Air-stable all-inorganic nanocrystal solar cells processed from solution. Science, 2005, 310, 462.
20. Lee, M., Teuscher, J., Miyasaka, T., Murakami, T., & Snaith, H. Efficient hybrid solar cells based on meso-superstructured organometal halide perovskites. Science, 2012, 338 (6107), 643-647.
21. Sariciftci, N., Smilowitz, L., Heeger, A., & Wudl, F. Photoinduced electron transfer from a conducting polymer to buckminsterfullerene. Science, 1992, 258 (5087), 1474-6.
22. O'Regan, B., & Grätzel, M. A low-cost, high-efficiency solar cell based on dye-sensitized colloidal TiO2 films. Nature, 1991, 353, 737-740.
23. Giri, D., Raut, S., & Patra, S. Diketopyrrolopyrrole/perylene-diimide and thiophene based D-π-A low bandgap polymer sensitizers for application in dye sensitized solar cells. Dyes and Pigments, 2020, 174, 108032.
24. https://www.nrel.gov/pv/cell-efficiency.html, NREL Photovoltaic Research - Best Research-Cell Efficiency Chart 2019, (accessed: February, 2020).
25. Brabec, C., & Durrant, J. Solution-Processed Organic Solar Cells. Mrs Bulletin, 2008, 33, 670-675.

26. Nielsen, T., Cruickshank, C., Søren, F., Thorsen, J., & Krebs, F. Business, market and intellectual property analysis of polymer solar cells. Sol Energ Mat Sol C, 2010, 94(10), 1553.
27. Shirakawa, H., Louis, E. J., MacDiarmid, A. G., Chiang, C. K., & Heeger, A. J. Synthesis of electrically conducting organic polymers: Halogen derivatives of polyacetylene, (CH)x. J. Chem. Soc. Chem. Commun. 1977, 578–580.
28. Tang, C. Two-layer organic photovoltaic cell. Appl. Phys. Lett. 1986, 48, 183.
29. Heeger, A., & Sariciftci, N. Patent US 1992/5331183 A.
30. Yu, G., Gao, J., Hummelen, J., Wudl, F., & Heeger, A. Polymer Photovoltaic Cells: Enhanced Efficiencies via a Network of Internal Donor-Acceptor Heterojunctions. Science, 1995, 270, 1789.
31. Halls, J., Walsh, C., Greenham, N., Marseglia, E., Friend, R., Moratti, S., & Holmes, A. Efficient photodiodes from interpenetrating polymer networks. Nature, 1995, 376, 498.
32. Hummelen, J., Knight, B., LePeq, F., Wudl, F., Yao, J., & Wilkins, C. Preparation and characterization of fulleroid and methanofullerene derivatives. J. Org. Chem., 1995, 60, 532–538.
33. Coakley, K., & Mcgehee, M. Conjugated Polymer Photovoltaic Cells. Chemistry of Materials, 2004, 16, 23, 4533 - 4542.
34. Marks, R., Halls, J., Bradley, D., Friend, R., & Holmes, A. The photovoltaic response in poly(p-phenylene vinylene) thin-film devices. Journal of Physics: Condensed Matter. 1994, 6 (7), 1379-1394.
35. Tamai, Y., Ohkita, H., Benten, H., & Ito, S. Exciton Diffusion in Conjugated Polymers: From Fundamental Understanding to Improvement in Photovoltaic Conversion Efficiency. The Journal of Physical Chemistry Letters, 2015, 6, 3417−3428.
36. Halls, J., Pichler, K., Friend, R., Moratti, S., & Holmes, A. Exciton diffusion and dissociation in a poly(p-phenylenevinylene)/C60 heterojunction photovoltaic cell, Applied Physics Letters, 1996, 68 (22), 3120.
37. Cusumano, P., Arnone, C., Giambra, M., & Parisi, A. Donor/Acceptor Heterojunction Organic Solar Cells. Electronics, 2020, 9, 70.
38. Li, Z., Ying, L., Zhu, P., Zhong, W., Li, N., Liu, F., Huang, F., & Cao, Y. A generic green solvent concept boosting the power conversion efficiency of all-polymer solar cells to 11%. Energy & Environmental Science, 2019, 12, 157-163.

39. Zhang, S., Qin, Y., Zhu, J., & Hou, J. Over 14% Efficiency in Polymer Solar Cells Enabled by a Chlorinated Polymer Donor. Advanced Materials, 2018, 30, 1800868.
40. Firdaus, Y., He, Q., Lin, Y., Nugroho, F., Le Corre, V., Yengel, E., Balawi, A., Seitkhan, Laquai, F., Langhammer, C., Liu, F., Heeney, M., & Anthopoulos, T. Novel wide-bandgap non-fullerene acceptors for efficient tandem organic solar cells. Journal of Materials Chemistry A, 2020, 8, 1164.
41. Fei, Z., Eisner, F., Jiao, X., Azzouzi, M., Röhr, J., Han, Y., Shahid, M., Chesman, A., Easton, C., McNeill, C., Anthopoulos, T., Nelson, J., & Heeney, M. An Alkylated Indacenodithieno [3,2-b]thiophene-Based Nonfullerene Acceptor with High Crystallinity Exhibiting Single Junction Solar Cell Efficiencies Greater than 13% with Low Voltage Losses. Advanced Materials, 2018, 30 (8), 30496–30502.
42. Liang, Y., & Yu, L. A new class of semiconducting polymers for bulk heterojunction solar cells with exceptionally high performance. Acc. Chem. Soc. 2010, 43 (9), 1227-36.
43. Li, Y. Molecular design of photovoltaic materials for polymer solar cells: toward suitable electronic energy levels and broad absorption. Acc. Chem. Res. 2012, 45 (5), 723-33.
44. Kim, J., Lee, K., Coater, N., Moses, D., Nguyen, T., Dante, M., & Heeger, A. Efficient tandem polymer solar cells fabricated by all-solution processing. Science, 2007, 317 (5835), 222-225.
45. He, Z., Zhong, C., Huang, X., Wong, W., Wu, H., Chen, L., Su, S., & Cao, Y. Simultaneous Enhancement of Open-Circuit Voltage, Short-Circuit Current Density, and Fill Factor in Polymer Solar Cells. Advanced Materials, 2011, 10, 296.
46. Ratcliff, E., Zacher, B., & Armstrong, N. Selective interlayers and contacts in organic photovoltaic cells. J. Phys. Chem. Lett., 2011, 2(11), 1337–1350.
47. Wang, J., Friedman, C., Cabrera, W., Tan, K., Lee, Y., Chabal, Y., & Hsu, J. Effect of metal/bulk-heterojunction interfacial properties on organic photovoltaic device performance. J. Mater. Chem. A, 2014, 2, 15288–15293.
48. Berger, P., & Kim, M. Polymer solar cells: P3HT:PCBM and beyond. Journal of Renewable and Sustainable Energy, 2018, 10 (1), 013508.
49. Li, G., Zhu, R., & Yang Y. Polymer solar cells. Nature Photonics, 2012, 6, 153–161.
50. Lu, L., Luo, Z., Xu, T., & Yu, L. Cooperative Plasmonic Effect of Ag and Au Nanoparticles on Enhancing Performance of Polymer Solar Cells. Nano Lett., 2013, 13, 59−64.

51. Feng, L., Niu, M., Wen, Z., & Hao, X. Recent Advances of Plasmonic Organic Solar Cells: Photophysical Investigations. Polymers, 2018, 10, 123.
52. Lai, T., Tsang, S., Manders, J., Chen, S., & So, F. Properties of interlayer for organic photovoltaics. Materials Today, 2013, 16 (11), 424-432.
53. Holliday, S., Li, Y., & Luscombe, C. Recent advances in high performance donor-acceptor polymers for organic photovoltaics. Progress in Polymer Science, 2017, 70, 34–51.
54. Pelzer, K., & Darling, S. Charge generation in organic photovoltaics: a review of theory and computation. Molecular Systems Design & Engineering, 2016, 1, 10-24
55. Wang, Q., Xie, Y., Soltani-Kordshuli, F., Eslamian, M. Progress in emerging solution-processed thin film solar cells – Part I: Polymer solar cells Qin. Renewable and Sustainable Energy Reviews, 2016, 56, 347-361.
56. Luo, G., Ren, X., Zhang, S., Wu, H., Choy, w., He, Z., & Cao, Y. Recent Advances in Organic Photovoltaics: Device Structure and Optical Engineering Optimization on the Nanoscale. Organic Photovoltaics, 2016, 12(12), 1547-71.
57. Qi, B., & Wang, J. Fill factor in organic solar cells. Phys. Chem. Chem. Phys., 2013, 15, 8972-8982.
58. Potscavage, W., Jr, Sharma, A., & Kippelen, B. Critical Interfaces in Organic Solar Cells and Their Influence on the Open-Circuit Voltage. Acc. Chem. Res., 2009, 42 (11), 1758–1767
59. Nelson, J. Polymer:fullerene bulk heterojunction solar cell. Materials today, 2011, 14 (10), 462- 470.
60. Yipa, H., & Jen, A. Recent advances in solution-processed interfacial materials for efficient and stable polymer solar cells. Energy Environ. Sci., 2012, 5, 5994–6011.
61. Heeger, A. 25th Anniversary Article: Bulk Heterojunction Solar Cells: Understanding the Mechanism of Operation. Advanced Materials, 2014, 26, 10–28.
62. Dennler, G., Scharber, M., & Brabec, C. Polymer-Fullerene bulk-heterojunction solar cells. Advanced Materials, 2009, 21, 1323–1338.
63. Jorgensen, M., Norrman, K., & Krebs, F. Stability/degradation of polymer solar cells. Sol. Energy Mater. Sol. Cells, 2008, 92, 686–714.
64. Dou, L., You, J., Hong, Z., Xu, Z., Li, G., Street, R., & Yang, Y. 25th Anniversary Article: A Decade of Organic/Polymeric Photovoltaic Research. Advanced Materials, 2013, 25, 6642–6671.

65. Sun, C., Wu, Z., Hu, Z., Xiao, J., Zhao, W., Li, H., Li, Q., Tsang, S., Xu, Y., Zhang, K., Yip, H., Hou, J., Huang, F. & Cao, Y. Interface Design for High-Efficiency Non-Fullerene Polymer Solar Cells. Energy & Environmental Science, 2017, 10, 1784-1791.
66. Yin, Z., Wei, J., & Zheng, Q. Interfacial Materials for Organic Solar Cells: Recent Advances and Perspectives. Advanced Science, 2016, 3 (8), 1500362.
67. Walker, B., Choib, H., & Kima, J. Interfacial Engineering for Highly Efficient Organic Solar Cells. Current Applied Physics, 2017, 17 (3), 370-391.
68. Steim, R., Kogler, F., & Brabec, C. Interface materials for organic solar cells. J. Mater. Chem. A, 2010, 20, 2499–2512.
69. Mingorance, A., Xie, H., Kim, H., Wang, Z., Balsells, M., Morales-Melgares, A., Domingo, N., Kazuteru, N., Tress, W., Fraxedas, J., Vlachopoulos, N., Hagfeldt, A., & Lira-Cantu, M. Interfacial Engineering of Metal Oxides for Highly Stable Halide Perovskite Solar Cells. Advanced Materials Interfaces, 2018, 5, 1800367.
70. Greiner, M., & Lu, Z. Thin-film metal oxides in organic semiconductor devices: Their electronic structures, work functions and interfaces. NPG Asia Mater. 2013, 5, e55.
71. https://www.sigmaaldrich.com/technical-documents/articles/materials-science/organic-electronics/agfa-opv.html, (accessed: February 2020).
72. Mai, C., Zhou, H., Zhang, Y., Henson, Z., Nguyen, T., Heeger, A., & Bazan, G. Facile Doping of Anionic Narrow-Band-Gap Conjugated Polyelectrolytes During Dialysis. Angew. Chem., Int. Ed., 2013, 52, 12874–12878.
73. Zhou, H., Zhang, Y., Mai, C., Collins, S., Nguyen, T., Bazan, G., & Heeger, A. A Highly Efficient Non-Fullerene Organic Solar Cell with a Fill Factor over 0.80 Enabled by a Fine-Tuned Hole-Transporting Layer. Advanced Materials, 2014, 26 (5), 780–785.
74. Carter, S., Angelopoulos, M., Karg, S., Brock, P., & Scott, J. Polymeric anodes for improved polymer light-emitting diode performance. Appl. Phys. Lett. 1997, 70, 2067–2069.
75. Kemerink, M., Timpanaro, S., de Kok, M., Meulenkamp, E., & Touwslager, F. Three-dimensional inhomogeneities in PEDOT:PSS films. J. Phys. Chem. B 2004, 108, 18820–18825.
76. Ionescu-Zanetti, C., Mechler, A., Carter, S., & Lal, R. Semiconductive polymer blends: Correlating structure with transport properties at the nanoscale. Advanced Materials, 2004, 16, 385–389.

77. Pingree, L., MacLeod, B., & Ginger, D. The Changing Face of PEDOT:PSS Films: Substrate, Bias, and Processing Effects on Vertical Charge Transport. J. Phys. Chem. C, 2008, 112, 7922–7927.

78. Dupont, S., Oliver, M., Krebs, F., & Dauskardt, R. Interlayer adhesion in roll-to-roll processed flexible inverted polymer solar cells. Sol. Energy Mater. Sol. Cells, 2012, 97, 171–175.

79. Xu, Z., Chen, L. M., Yang, G. W., Huang, C. H., Hou, J. H., Wu, Y., Li, G., Hsu, C. S., & Yang, Y. Vertical Phase Separation in Poly(3-hexylthiophene): Fullerene Derivative Blends and its Advantage for Inverted Structure Solar Cells. Advanced Functional Materials, 2009, 19 (8), 1227-1234.

80. Melendez, R., Moreno, K., Moggio, I., Arias, E., Ponce, A., Llanera, I., & Moya, S. On the Influence of Silver Nanoparticles Size in the Electrical Conductivity of PEDOT:PSS. Materials Science Forum, 2010, 644, 85-90.

81. Singh, J., Nirwal, V., Bhatnagar, P., & Peta, K. Effect of incorporation of silver nanoparticles in PEDOT:PSS layer on performance of organic solar cell. 2nd International Conference on Condensed Matter and Applied Physics, 2018, 030251-3.

82. Suh, Y., Park, S., Lee, T., Chung, W., Kim, K., & Kim, M. TEM Study of Stability of Inverted Photovoltaic (PV) Cells. Microsc. Microanal., 2010, 16, 1378–1379.

83. Peng, Y., Yaacobi-Gross, N., Perumal, A., Faber, H., Vourlias, G., Patsalas, P., Bradley, D., He, Z., & Anthopoulos, T. Efficient organic solar cells using copper (I) iodide (CuI) hole transport layers. Appl. Phys. Lett. 2015, 106, 243302.

84. Uthayaraj, S., Karunarathne, D., Kumara, G., Murugathas, T., Rasalingam, S., Rajapakse, R., Ravirajan, P., & Velauthapillai, D. Powder Pressed Cuprous Iodide (CuI) as A Hole Transporting Material for Perovskite Solar Cells. Materials, 2019, 12, 2037.

85. Yaacobi-Gross, N., Treat, N., Pattanasattayavong, P., Faber, H., Perumal, A., Stingelin, N., Bradley, D., Stavrinou, P., Heeney, M., & Anthopoulos, T. High-Efficiency Organic Photovoltaic Cells Based on the Solution-Processable Hole Transporting Interlayer Copper Thiocyanate (CuSCN) as a Replacement for PEDOT:PSS. Adv. Energy Mater. 2015, 5, 1401529.

86. Wijeyasinghe, N., Eisner, F., Tsetseris, L., Lin, Y., Seitkhan, A., Li, J., Yan, F., Solomeshch, O., Tessler, N., Patsalas, P., & Anthopoulos, T. p-Doping of Copper(I) Thiocyanate

(CuSCN) Hole-Transport Layers for High-Performance Transistors and Organic Solar Cells. Adv. Funct. Mater., 2018, 28, 1802055.

87. Li, S., Tu, K., Lin, C., Chen, C., & Chhowalla, M. Solution-processable graphene oxide as an efficient hole transport layer in polymer solar cells. ACS Nano, 2010, 4, 3169–3174.

88. Tu, K., Li, S., Li, W., Wang, D., Yang, J., & Chen, W. Solution processable nanocarbon platform for polymer solar cells. Energy Environ. Sci., 2011, 4, 3521–3526.

89. Liu, J., Xue, Y., Gao, Y., Yu, D., Durstock, M., & Dai, L. Hole and electron extraction layers based on graphene oxide derivatives for high-performance bulk heterojunction solar cells. Adv. Mater., 2012, 24, 2228–2233.

90. Liu, J., Durstock, M., & Dai, L. Graphene oxide derivatives as hole- and electron-extraction layers for high-performance polymer solar cells. Energy Environ. Sci., 2014, 7(4), 1297–1306.

91. Intemann, J., Yao, K., Li, Y., Yip, H., Xu, Y., Liang, P., Chueh, C., Ding, F., Yang, X., Li, X., Chen, Y., & Jen, A. Highly Efficient Inverted Organic Solar Cells Through Material and Interfacial Engineering of Indacenodithieno[3,2-b] thiophene- Based Polymers and Devices. Adv. Funct. Mater., 2014, 24, 1465.

92. https://dentagama.com/news/use-of-graphene-oxide-in-dentistry, (accessed: February 2020).

93. Gao, Y., Yip, H., Hau, S., Malley, K., Cho, N., Chen, H., & Jen, A. Anode modification of inverted polymer solar cells using graphene oxide. Appl. Phys. Lett., 2010, 97,203306.

94. Kim, H., Yusoff, A., Jang, J. Organic solar cells using a reduced graphene oxide anode buffer layer. Sol. Energy Mater. Sol. Cells, 2013, 110, 87-93.

95. Liu, X., Kim, H., &. Guo, L. Optimization of thermally reduced graphene oxide for an efficient hole transport layer in polymer solar cells. Organic Electronic, 2013, 14 (2), 591-598.

96. Stankovich, S., Dikin, D., Piner, R., Kohlhaas, K., Kleinhammes, A., Jia, Y., Wu, Y., Nguyen, S., & Ruoff, R. Synthesis of graphene-based nanosheets via chemical reduction of exfoliated graphite oxide. Carbon, 2007, 45, 1558-1565.

97. Mattevi, C., Eda, G. Agnoli, S. Miller, S. Mikhoyan, K. Celik, O. Matsrogiovanni, D. Granozzi, G., Garfunkel E., & Chhowalla, M. Evolution of Electrical, Chemical, and Structural Properties of Transparent and Conducting Chemically Derived Graphene Thin Films. Advanced Functional Materials, 2009, 19(16), 2577.

98. Gengler, R., Badali, D., Zhang, D., Dimos, K., Spyrou, K., Gournis, D., & Miller, J. Revealing the ultrafast process behind the photoreduction of graphene oxide. Nature Communications, 2013, 4, 2560.
99. Petridis, C., Konios, D., Stylianakis, M. Kakavelakis, G., Sygletou, M., Savva, K., Tzourmpakis, P., Krassas, M., Vaenas, N., Stratakis, E., & Kymakisa, E. Solution processed reduced graphene oxide electrodes for organic photovoltaics. Nanoscale Horizons, 2016, 1, 375-382.
100. Balis, N., Stratakis, E., Kymakis, E. Graphene and transition metal dichalcogenide nanosheets as charge transport layers for solution processed solar cells. Materials Today, 2016.
101. Mao, S., Pu, H., & Chen, J. Graphene oxide and its reduction: modeling and experimental progress. J. RSC Adv., 2012, 2 (7), 2643–2662.
102. Acik, M., & Darling, S. Graphene in perovskite solar cells: Device design, characterization and implementation. Journal of Materials Chemistry A, 2016, ,4 (17), 6185-6235.
103. Yang, D., Zhou, L., Chen, L., Zhao, B., Zhang, J., & Li, C. Chemically modified graphene oxides as a hole transport layer in organic solar cells. Chemical Communications, 2012, 48 (62), 8078–8080.
104. Yang, D., Zhou, L., Yu, W., Zhang, J., & Li, C. Work-Function-Tunable Chlorinated Graphene Oxide as an Anode Interface Layer in High-Efficiency Polymer Solar Cells. Advanced Energy Materials, 2014, 4 (15), 1400591.
105. Ryu, M., & Jang, J. Effect of solution processed graphene oxide/nickel oxide bi-layer on cell performance of bulk-heterojunction organic photovoltaic. Solar Energy Materials and Solar Cells, 2011, 95(10), 2893–2896.
106. Fan, G., Zhuo, Q., Zhu, J., Xu, Z., Cheng, P., Li, Y., Sun, X., Lee, S., & Tang, J. Plasmonic-enhanced polymer solar cells incorporating solution-processable Au nanoparticle-adhered graphene oxide. Journal of Materials Chemistry, 2012, 22 (31), 15614–15619.
107. Yang, Q., Li, J., Cheng, Y., Li, H., Guan, Z., Yu, B., & Tsang, S. Graphene oxide as an efficient hole-transporting material for high-performance perovskite solar cells with enhanced stability. Journal of Materials Chemistry A, 2017, 5, 9852–9858.
108. Liu, Q., Leng, C., & Yuan, J. A Planar Heterojunction Perovskite Solar Cell Modified by Graphene Oxide. Materials Science and Engineering, 2018, 452, 022135.

109. Tokito, S., Noda, K. & Taga, Y. Metal oxides as a hole-injecting layer for an organic electroluminescent device. Journal of Physics D: Applied Physics, 1996, 29, 2750–2753.
110. Meyer, J., Hamwi, S., Kröger, M., Kowalsky, W., Riedl, T., & Kahn, A. Transition Metal Oxides for Organic Electronics: Energetics, Device Physics and Applications. Advanced Materials, 2012, 24 (40), 5408–5427.
111. Chen, S., Manders, J., Tsang, S., & So, F. Metal oxides for interface engineering in polymer solar cells. Journal of Materials Chemistry, 2012, 22 (46), 24202-24212.
112. Greiner, M., Chai, L., Helander, M., Tang, W., & Lu, Z. Transition metal oxide work functions: the influence of cation oxidation state and oxygen vacancies. Advanced Functional Materials, 2012, 22 (21), 4557.
113. Irfan, I., Ding, H., Gao, Y., Small, C., Kim, D. Y., Subbiah, J. & So, F. Energy level evolution of air and oxygen exposed molybdenum trioxide films. Appl. Phys. Lett., 2010, 96, 243307.
114. Kroger, M., Hamwi, S., Meyer, J., Riedl, T., Kowalsky, W. & Kahn, A. Role of the deeplying electronic states of MoO3 in the enhancement of hole-injection in organic thin films. Appl. Phys. Lett., 2009, 95, 123301.
115. Shrotriya, V., Li, G., Yao, Y., Chu, C. W. & Yang, Y. Transition metal oxides as the buffer layer for polymer photovoltaic cells. Appl. Phys. Lett., 2006, 88, 073508.
116. Zilberberg, K., Meyer, J., & Riedl, T. Solution processed metal-oxides for organic electronic Devices. Journal of Materials Chemistry C, 2013, 1(32), 4796–4815.
117. Wang, F., Tan, Z., & Li, Y. Solution-processable metal oxides/chelates as electrode buffer layers for efficient and stable polymer solar cells. Energy Environ. Sci., 2015, 8, 1059-1091.
118. Li, Y., Wang, Q., Ou Q., & Tang, J. Interface energetics and engineering of organic heterostructures in organic photovoltaic cells. Science China Chemistry, 2016, 59, 422–435.
119. Schulz, p., Tiepelt, J., Christians, J., Levine, I., Edri, E., Sanehira, E., Hodes, G., Cahen, D., & Kahn, A. High-Work-Function Molybdenum Oxide Hole Extraction Contacts in Hybrid Organic–Inorganic Perovskite Solar Cells. ACS Applied Materials & Interfaces, 2016, 8, 31491−31499.
120. Raebiger, H., Lany, S. & Zunger, A. Origins of the p-type nature and cation deficiency in cu2o and related materials. Phys. Rev. B, 2007, 76, 045209.

121. Greiner, M., Helander, M., Tang, W., Wang, Z., Qiu, J., & Lu, Z. Universal energy-level alignment of molecules on metal oxides. Nat. Mater., 2012, 11, 76–81.
122. Greiner, M., Helander, M., Wang, Z., Tang, W., & Lu, Z. Effects of processing conditions on the work function and energy-level alignment of Nio thin films. The Journal of Physical Chemistry C, 2010, 114, 19777–19781.
123. Lany, S., Osorio-Guillen, J. & Zunger, A. Origins of the doping asymmetry in oxides: hole doping in NiO versus electron doping in ZnO. Phys. Rev. B, 2007, 75, 241203.
124. Tao, C., Ruan, S., Xie, G., Kong, X., Shen, L., Meng, F., Liu, C., Zhang, X., Dong, W. & Chen, W. Role of tungsten oxide in inverted polymer solar cells. Appl. Phys. Lett., 2009, 94, 043311.
125. Stubhan, T., Ameri, T., Salinas, M., Krantz, J., Machui, F., Halik, M. & Brabec, C. J. High shunt resistance in polymer solar cells comprising a MoO3 hole extraction layer processed from nanoparticle suspension. Appl. Phys. Lett., 2011, 98, 253308.
126. Waldauf, C., Morana, M., Denk, P., Schilinsky, P., Coakley, K., Choulis, S. & Brabec, C. Highly efficient inverted organic photovoltaics using solution-based titanium oxide as electron selective contact. Appl. Phys. Lett., 2006, 89, 233517.
127. Wong, K. H., Ananthanarayanan, K., Luther, J. & Balaya, P. Origin of hole selectivity and the role of defects in low-temperature solution-processed molybdenum oxide interfacial layer for organic solar cells. The Journal of Physical Chemistry C, 2012, 116, 16346–16351.
128. Kyaw, A., Sun, X., Jiang, C., Lo, G., Zhao, D., & Kwong, D. An inverted organic solar cell employing a sol-gel derived ZnO electron selective layer and thermal evaporated moo3 hole selective layer. Appl. Phys. Lett., 2008, 93, 221107.
129. Steirer, K., Chesin, J., Widjonarko, N., Berry, J., Miedaner, A., Ginley, D., & Olson, D. Solution deposited nio thin films as hole transport layers in organic photovoltaics. Org. Electron, 2010, 11, 1414–1418.
130. Steirer, K., Ndione, P., Widjonarko, N., Lloyd, M., Meyer, J., Ratcliff, E., Kahn, A., Armstrong, N., Curtis, C., Ginley, D., Berry, J. & Olson, D. Enhanced efficiency in plastic solar cells via energy matched solution processed NiOx interlayers. Adv. Energy Mater., 2011, 1, 813–820.
131. Steim, R., Choulis, S., Schilinsky, P. & Brabec, C. Interface modification for highly efficient organic photovoltaics. Appl. Phys. Lett., 2008, 92, 093303 (2008).

132. Henrich, V., & Cox, P. The Surface Science of Metal Oxides. Cambridge University Press, Cambridge 1994, XIV, 464 pp.
133. Hammond, S., Meyer, J., Widjonarko, N., Ndione, P., Sigdel, A., Garcia, A., Miedaner, A., Lloyd, M., Kahn, A., Ginley, D., Berry J., & Olson, D. Low-temperature, solution-processed molybdenum oxide hole-collection layer for organic photovoltaics. J. Mater. Chem. A, 2012, 22, 3249–3254.
134. Stubhan, T., Li, N., Luechinger, N., Halim, S., Matt, G., & Brabec, C. High fill factor polymer solar cells incorporating a low temperature solution processed WO3 hole extraction layer. Adv. Energy Mater., 2012, 2, 1433–1438.
135. Zilberberg, K., Trost, S., Schmidt H., & Riedl, T. Solution Processed Vanadium Pentoxide as Charge Extraction Layer for Organic Solar Cells. Adv. Energy Mater., 2011, 1, 377–381.
136. Meyer, B., Polity, A., Reppin, D., Becker, M., Hering, P., Klar, P., Sander, T., Reindl, C., et al. Binary copper oxide semiconductors: From materials towards devices. Phys. Status Solidi B, 2012, 249 (8), 1487–1509.
137. Meyer, J., Shu, A., Kroger, M. & Kahn, A. Effect of contamination on the electronic structure and hole-injection properties of MoO3/organic semiconductor interfaces. Appl. Phys. Lett., 2010, 96, 133308.
138. Scanlon, D., Morgan, B., Watson, G., & Walsh, A. Acceptor levels in p-type Cu2O: rationalizing theory and experiment. Phys. Rev. Lett., 2009, 103, 096405.
139. Nolan, M., & Elliott, S. The p-type conduction mechanism in cu2o: a first principles study. Phys. Chem. Chem. Phys., 2006, 8, 5350–5358.
140. Green, M. The nature of quantum dot capping ligands. Journal of Materials Chemistry, 2010, 20(28), 5797–5809
141. Richter, T., Stelzl, F., Schulz-Gericke, J., Kerscher, B., Wurfel, U., Niggemann, M., & Ludwigs, S. Room temperature vacuum-induced ligand removal and patterning of ZnOnanoparticles: from semiconducting films towards printed electronics. Journal of Materials Chemistry, 2010, 20(5), 874–879.
142. Li, S., Chang, C. Lin, C., Lin, Y., Chang, C., Yang, J., Chu, M., & Chen, C. Interplay of Three-Dimensional Morphologies and Photocarrier Dynamics of Polymer/TiO2 Bulk Heterojunction Solar Cells. Journal of American Chemical Society, 2011, 133 (30), 11614–11620.

143. Choy, W., & Zhang, D. Solution-Processed Metal Oxides as Efficient Carrier Transport Layers for Organic Photovoltaics. Small, 2016, 12 (4).
144. Niederberger, M. Nonaqueous Sol–Gel Routes to Metal Oxide Nanoparticles. Accounts of chemical research, 2007, 40 (9), 793–800.
145. Bradley, D., Metal alkoxides as precursors for electronic and ceramic materials. Chemical Reviews, 1989, 89 (6), 1317–1322.
146. Pasquarelli, R., Ginley, D., & O'Hayre, R. Solution processing of transparent conductors: from flask to film. Chemical Society Reviews, 2011, 40 (11), 5406–5441.
147. Qin, P., He, Q., Ouyang, D., Fang, G., Choy, W., & Li, G. Transition metal oxides as hole-transporting materials in organic semiconductor and hybrid perovskite based solar cells. Science China Chemistry, 2017, 60, 472–489.
148. Kim, M., Kanatzidis, M., Facchetti, A., & Marks, T. Low-temperature fabrication of high-performance metal oxide thin-film electronics via combustion processing. Nat. Mater., 2011, 10, 382–388.
149. Fortunato, E., Barquinha, P., & Martins, R. Oxide Semiconductor Thin-Film Transistors: A Review of Recent Advances. Adv. Mater. 2012, 24, 2945–2986.
150. Kundu, S., Gollu, S., Sharma, R., Srinivas, G., Ashok, A., Kulkarni, A., & Gupta, D. Device stability of inverted and conventional bulk heterojunction solar cells with MoO3 and ZnO nanoparticles as charge transport layers. Organic Electronics, 2013, 14(11), 3083–3088.
151. Kroger, M., Hamwi, S., Meyer, J., Riedl, T., Kowalsky, W., & Kahn, A. Role of the deep-lying electronic states of MoO3 in the enhancement of hole-injection in organic thin films. Applied Physics Letters, 2009, 95, 123301.
152. Liu, F., Shao, S., Guo, X., Zhao Y., & Xie, Z. Efficient polymer photovoltaic cells using solution-processed MoO3 as anode buffer layer. Sol. Energy Mater. Sol. Cells, 2010, 94 (5), 842–845.
153. Murase, S., & Yang, Y. Solution Processed MoO3 Interfacial Layer for Organic Photovoltaics Prepared by a Facile Synthesis Method. Advanced materials, 2012, 24 (18), 2459–2462.
154. Yang, T., Wang, M., Cao, Y., Huang, F., Huang, L., Peng, J., Gong, X., Cheng, S., & Cao, Y. Inverted polymer solar cells with 8.4% efficiency by conjugated polyelectrolyte. Adv. Energy Mater., 2012, 2, 523–527.

155. Girotto, C., Voroshazi, E., Cheyns, D., Heremans P., & Rand, B. Solution-Processed MoO3 Thin Films as a Hole-Injection Layer for Organic Solar Cells. ACS Appl. Mater. Interfaces, 2011, 3, 3244–3247

156. Meyer, J., Khalandovsky, R., Görrn P., & Kahn, A. MoO3 Films Spin-Coated from a Nanoparticle Suspension for Efficient Hole-Injection in Organic Electronics. Adv. Mater., 2011, 23 (1), 70–73.

157. Jasieniak, J., Seifter, J., Jo, J., Mates, T., & Heeger, A. A Solution-Processed MoOx Anode Interlayer for Use within Organic Photovoltaic Devices. Adv. Funct. Mater., 2012, 22 (12), 2594– 2605.

158. Zilberberg, K., Gharbi, H., Behrendt, A., Trost, S., & Riedl, T. Low-Temperature, Solution-Processed MoOx for Efficient and Stable Organic Solar Cells. ACS Applied materials & interfaces, 2012, 4, 1164–1168.

159. Tan, Z., Qian, D., Zhan, X., Li, L., Ding, Y., Xu, Q., Wang, F., & Li, Y. Efficient and stable polymer solar cells with solution-processed molybdenum oxide interfacial layer. J. Mater. Chem. A, 2013, 1, 657–664.

160. Xie, F., Choy, W., Wang, C., Li, X., Zhang, S., & Hou, J. Low-Temperature Solution-Processed Hydrogen Molybdenum and Vanadium Bronzes for an Efficient Hole-Transport Layer in Organic Electronics. Adv. Mater. 2013, 25 (14), 2051–2055.

161. Soultati, A., Douvas , A., Georgiadou, D., Palilis, L., Bein, T., Feckl, J., Gardelis, S., Fakis, M., Kennou, S., Falaras, P., Stergiopoulos, T., Stathopoulos, N., Davazoglou, D., Argitis, P., & Vasilopoulou, M. Solution-Processed Hydrogen Molybdenum Bronzes as Highly Conductive Anode Interlayers in Efficient Organic Photovoltaics. Advanced Energy Materials, 2014, 4(3).

162. Li, X., Choy, W., Xie, F., Zhang, S., & Hou, J. Room-temperature solution-processed molybdenum oxide as a hole transport layer with Ag nanoparticles for highly efficient inverted organic solar cells. Journal of Materials Chemistry A. 2013, 1(22), 6614- 6621.

163. Shamjid, p., Abhijith, T., Vivek, P., Joel, C., & Reddy, V. Plasmonic effects of Ag nanoparticles for absorption enhancement in polymer solar cells with MoO3 passivation layer. Physica B: Condensed Matter, 2019, 560, 174–184.

164. Höfle, S., Do, H., Mankel, E., Pfaff, M., Zhang, Z., Bahro, D., Mayer, T., Jaegermann, W., Gerthsen, D., Feldmann, C., Lemmer, U., & Colsmann, A. Molybdenum oxide anode

buffer layers for solution processed, blue phosphorescent small molecule organic light emitting diodes. Organic Electronics, 2013, 14, 1820–1824.

165. Yao, C., Xu, X., Wang, J., Shi L., & Li, L. Low-Temperature, Solution-Processed Hole Selective Layers for Polymer Solar Cells. ACS Appl. Mater. Interfaces, 2013, 5 (3), 1100–1107.
166. Dang, Y., Wang, Y., Shen, S., Huang, S., Qu, X., Pang, Y., Silva, S., Kanga, K., & Lu, G. Solution processed hybrid Graphene-MoO3 hole transport layers for improved performance of organic solar cells. Organic Electronics, 2019, 67, 95–100.
167. Aatif, M., Patel, J., Sharma, C., Chauhan, M., Kumar, G., Pal, P., Chand, S., Tripathi, B., Pandey, M., & Tiwari1, J. Graphene oxide-molybdenum oxide composite with improved hole transport in bulk heterojunction solar cells. AIP Advances, 2019, 075215.
168. Bai, Y., Zhao, C., Guo, Q., Zhang, J., Hu, S., Liu, J., Hayat, T., Alsaedi, A., & Tan, Z. Enhancing the electron blocking ability of n-type MoO3 by doping with p-type NiOx for efficient nonfullerene polymer solar cells. Organic Electronics, 2019 68, 168–175.
169. Cai, P., Ren, P., Huang, X., Zhang, X., Zhan, T., Xiong, J., Xue, X., Wang, Z., Zhang, J., & Chen, J. An Ultraviolet-Deposited MoO3 Film as Anode Interlayer for High-Performance Polymer Solar Cells. Advanced Materials Interfaces, 2020, 1901912.
170. Tan, Z., Li, L., Cui, C., Ding, Y., Xu, Q., Li, S., Qian, D., & Li, Y. Solution-Processed Tungsten Oxide as an Effective Anode Buffer Layer for High-Performance Polymer Solar Cells. J. Phys. Chem. C, 2012, 116 (35), 18626– 18632.
171. Hochst, H., & Bringans, R. Electronic structure of evaporated and annealed tungsten oxide films studied with UPS Appl. Surf. Sci., 1982, 11(2), 768–773.
172. Meyer, J., Kröger, M., Hamwi, S., Gnam, F., Riedl, T., Kowalsky, W., & Kahn, A. Charge generation layers comprising transition metal-oxide/organic interfaces: Electronic structure and charge generation mechanism. Appl. Phys. Lett., 2010, 96, 193302.
173. Choi, H., Kim, B., Ko, M., Lee, D., Kim, H., Kim, S., & Kim, K. Solution processed WO 3 layer for the replacement of PEDOT: PSS layer in organic photovoltaic cells. Org. Electron., 2012, 13, 959–968.
174. Özer, N. comparison. Thin Solid Films, 1997, 304, 310–314.
175. Pyper, O., Schollhorn, R., Donkers, J., & Krings, L. Nanocrystalline structure of WO3 thin films prepared by the sol-gel technique. Materials Research Bulletin, 1998, 33 (7), 1095–1101.

176. Huang, J, Chou, C., Lin, C. Efficient and air-stable polymer photovoltaic devices with WO3-V2O5 mixed oxides as anodic modification. IEEE Electron Device Lett. 2010, 31, 332–334.

177. Ji, R., Zheng, D., Zhou, C., Cheng, J., Yu, J., & Li, L. Low-Temperature Preparation of Tungsten Oxide Anode Buffer Layer via Ultrasonic Spray Pyrolysis Method for Large-Area Organic Solar Cells. Materials, 2017, 10(7), 820.

178. Prakash, O., Saxena, V., Choudhury, S., Tanvi, Singh, A., Debnath, A., Mahajan, A., Muthe, K., & Aswal, D. Low temperature processable ultra-thin WO3 Langmuir-Blodgett film as excellent hole blocking layer for enhanced performance in dye sensitized solar cell. Electrochimica Acta, 2019, 318, 405-412.

179. Benmouss, M., Outzourhit, A., Jourdani, R., Bennouna, A., & Ameziane, E. Structural, Optical and Electrochromic properties of Sol–gel V2O5 thin films. Act. Passive Electron. Compon., 2003, 26, 245–256.

180. Huang, J., Chou, C., Liu, M., Tsai K., Lin, W., & Lin, C. Solution-processed vanadium oxide as an anode interlayer for inverted polymer solar cells hybridized with ZnO nanorods. Org. Electron. 2009, 10 (6), 1060– 1065.

181. Zilberberg, K., Trost, S., Meyer, J., Kahn, A. Behrendt, A. Lützenkirchen-Hecht, D., Frahm, R., & Riedl, T. Inverted Organic Solar Cells with Sol–Gel Processed High Work-Function Vanadium Oxide Hole-Extraction Layers. Advanced Functional Materials, 2011, 21 (24), 4776.

182. Tan, Z., Zhang, W., Cui, C., Ding, Y., Qian, D., Xu, Q., Li, L., Li, S., & Li, Y. Solution-processed vanadium oxide as a hole collection layer on an ITO electrode for high-performance polymer solar cells. Phys. Chem. Chem. Phys., 2012, 14, 14589–14595.

183. Escobar, G., Pampel, J., Caicedo, J., &. Cantu, M. Low-temperature, solution-processed, layered V2O5 hydrate as the hole-transport layer for stable OSCs. Energy Environ. Sci., 2013, 6, 3088–3098.

184. Rafique, S., Abdullah, S., Mahmoud, W., Al-Ghamdi, A., & Sulaiman, K. Stability enhancement in organic solar cells by incorporating V2O5 nanoparticles in the hole transport layer. RSC Advances, 2016, 6 (55), 50043-50052

185. Jiang, Y., Xiao, S., Xu, B., Zhan, C., Mai, L., Lu, X., & You, W. Enhancement of Photovoltaic Performance by Utilizing Readily Accessible Hole Transporting Layer of Vanadium (V)

Oxide Hydrate in a Polymer–Fullerene Blend Solar Cell. ACS applied materials, 2016, 18, 11658-11666.

186. Zafar, M., Yun, J., & Kim, D. Highly stable inverted organic photovoltaic cells with a V2O5 hole transport layer. Korean Journal of Chemical Engineering, 2017, 34, 1504–1508.
187. Lampande, R., Kim, G., Boizot, J., Kim, Y., Pode, R., & Kwon, J. A highly efficient transition metal oxide layer for hole extraction and transport in inverted polymer bulk heterojunction solar cells. J. Mater. Chem. A, 2013, 1, 6895–6900.
188. Dong, J., Wu, J., Jia, J., He, X., Lan, Z., Fan, L., Lin, J., & Huang, M. Annealing-Free Cr2O3 Electron-Selective Layer for Efficient Hybrid Perovskite Solar Cells. ChemSusChem, 2017, 11 (3).
189. Zheng, S., Li, W., Su, T., Xie, F, Chen, J., Yang, Z., Zheng, Y., Liu, S., Aldred, M., Wong, K., & Chi, Z. Metal Oxide CrOx as a Promising Bilayer Electron Transport Material for Enhancing the Performance Stability of Planar Perovskite Solar Cells. Solar RRL, 2018, 2 (6).
190. Tu, X., Wang, F., Li, C., Tan Z., & Li, Y. Solution-Processed and Low-Temperature Annealed CrOx as Anode Buffer Layer for Efficient Polymer Solar Cells J. Phys. Chem. C, 2014, 118, 9309–9317.
191. Wang, F., Xu, Q., Tan, Z., Li, L., Li, S., Sun, G., Tu, X., Hou, J., & Li, Y. Efficient polymer solar cells with a solution-processed and thermal annealing-free RuO_2 anode buffer layer. J. Mater. Chem. A, 2014, 2, 1318–1324.
192. Baikie, I., Peterman, U., L¨agel, B., & Dirscherl, K. Study of high- and low-work-function surfaces for hyperthermal surface ionization using an absolute Kelvin probe. Journal of Vacuum Science & Technology A, 2001, 19, 1460–1466.
193. Tan, Z., Li, L., Wang, F., Xu, Q., Li, S., Sun, G., Tu, X., Hou, X., Hou, J., and Y. Li, Solution-Processed and Low-Temperature Annealed CrOx as Anode Buffer Layer for Efficient Polymer Solar Cells, Adv. Energy Mater., 2014, 4, 1300884.
194. Melorose, J., Perroy, R., Careas, S. Statewide Agricultural Land Use Baseline, 2015, 1.
195. https://www.ossila.com/pages/spin-coating, (accessed: February 2020).
196. Ying, Y., Ping, Z., Shang-Xiong, Z., Xiao-Guang, G., & Dong-Ming, G. Effect of substrate curvature on thickness distribution of polydimethylsiloxane thin film in spin coating process. Chinese Physics B, 2018, 27(6).

197. Park, S., Quan, Y., Kim, S., Kim, H., Kim, S., Chun, D., Lee, C., Taya, M., Chu, W., & Ahn, S. A review on fabrication processes for electrochromic devices. International Journal of Precision Engineering and Manufacturing-Green Technology, 2016, 3.
198. https://commons.wikimedia.org/wiki/File:XPS_PHYSICS.png, (accessed: February 2020).
199. Nasir, S., Hussein, M., Zainal, Z., Yusof, N., Zobir, S., & Alibe, I. Potential Valorization of By-product Materials from Oil Palm: A review of Alternative and Sustainable Carbon Sources for Carbon-based Nanomaterials Synthesis. BioResourses, 2019, 14 (1), 2352-2388.
200. https://commons.wikimedia.org/wiki/File:AFMsetup.jpg, (accessed: February 2020).
201. Tauc, J., Grigorovici, R., & Vancu, A. Optical properties and electronic structure of amorphous germanium. physica status solidi (b), 1966. 15(2): p. 627-637.
202. http://www.airphotoemission.com/airphotoemission.html, (accessed: February 2020).
203. Gualtieri, D. Graphene from Nickel. 2014, (accessed: February, 2020), http://www.tikalon.com/blog/blog.php?article=2014/Ni_graphene_process.
204. Yu, W., Shen, L., Ruan, S., Meng, F., Wang, J., Zhang, E., & Chen, W. Performance improvement of inverted polymer solar cells thermally evaporating nickel oxide as an anode buffer layer. Sol. Energy Mater. Sol. Cells, 2012, 98, 212–215.
205. Islam, R., Chen, G., Ramesh, P., Suh, J., Fuchigami, N., Lee, D., Karl A. Littau, K., Weiner, K., Collins, R., & Saraswat, K. Investigation of the Changes in Electronic Properties of Nickel Oxide (NiOx) Due to UV/Ozone Treatment. Applied materials & Interfaces, 2017, 9, 20, 17201-17207.
206. Mashford, B., Nguyen, T., Wilson, G., & Mulvaney, P. All-inorganic quantum-dot light-emitting devices formed via low-cost, wet-chemical processing. J. Mater. Chem., 2010, 20, 167–172.
207. Garcia, A., Welch, G., Ratcliff, E., Ginley, D., Bazan G., & Olson, D. Improvement of Interfacial Contacts for New Small-Molecule Bulk-Heterojunction Organic Photovoltaics. Advanced Materials, 2012, 24, 5368–5373.
208. Manders, J., Tsang, S., Hartel, M., Lai, T., Chen, S., Amb, C., Reynolds, J., & So, F., 2013. Solution-processed nickel oxide hole transport layers in high efficiency polymer photovoltaic cells. Advanced Functional Materials, 2013, 23 (23), 2993–3001.

209. Zhai, Z., Huang, X., Xu, M., Yuan, J., Peng, J. & Ma, W. Greatly Reduced Processing Temperature for a Solution-Processed NiOx Buffer Layer in Polymer Solar Cells. Adv. Energy Mater., 2013, 3, 1614–1622.
210. Bai, S., Cao, M., Jin, Y., Dai, X., Liang, X., Ye, Z., Li, M., Cheng, J., Xiao, X., Wu, Xia, Z., Sun, B., Wang, E., Mo, Y., Gao, F., & Zhang, F. Optoelectronic Devices: Low-Temperature Combustion-Synthesized Nickel Oxide Thin Films as Hole-Transport Interlayers for Solution-Processed, Optoelectronic Devices. Adv. Energy Mater. 2014, 4 (6), 1301460.
211. Zhang, J., Wang, J., Fu, Y., Zhang, B., & Xie, Z. Efficient and stable polymer solar cells with annealing-free solution-processible NiO nanoparticles as anode buffer layers. Journal of Materials Chemistry C, 2014, 2, 8295–8302.
212. Jiang, F., Choy, W., Li, X., Zhang, D., & Cheng, J. Post-treatment-Free Solution-Processed Non-stoichiometric NiOx Nanoparticles for Efficient Hole-Transport Layers of Organic Optoelectronic Devices. Adv. Mater. 2015, 27, 2930.
213. Eperon, G., Moerman, D., & Ginger, D. Anticorrelation between Local Photoluminescence and Photocurrent Suggests Variability in Contact to Active Layer in Perovskite Solar Cells. ACS Nano 2016, 10, 11, 10258-10266.
214. Lin, Y., Liao, y., Hsiao, H., & Chen, C. Two-step annealing of NiOx enhances the NiOx–perovskite interface for high-performance ambient-stable p–i–n perovskite solar cells. Applied Surface Science, 2020, 504, 144478.
215. Tang, J., Jiao, D., Zhang, L., Zhang, X., Xu, X., Yao, c., Wu, J., & Lan, Z. High-performance inverted planar perovskite solar cells based on efficient hole-transporting layers from well-crystalline NiO nanocrystals. Solar Energy, 2018, 161, 100-108.
216. Chowdhury, T., Kaneko, R., Kayesh, M., Akhtaruzzaman, M., Sopian, K., Lee, J., & Islam, A. Nanostructured NiOx as hole transport material for low temperature processed stable perovskite solar cells. Materials Letters, 2018, 223, 109-111.
217. Hodgkinson, J., & Yates, H. NiOx via Flame Assisted CVD as a Route to Stable, Low Cost, Large Area, Hole Transport Layers for Perovskite Solar Cells. Proc. PVSAT 14, 2018.
218. Yates, H., Hodgkinson, J., Meroni, S., Richards, D., & Watson, T. Flame Assisted Chemical Vapour Deposition of NiO hole transport layers for planar perovskite cells. Surface and Coatings Technology, 2020, 385, 125423.

219. Koshtyal, Y., Nazarov, D., Ezhov, I., Mitrofanov, I., Kim, A., Rymyantsev, A., Lyutakov, O., Popovich, A., & Maximov, M. Atomic layer deposition of nio to produce active material for thin-film lithium-ion batteries. Coatings, 2019, 9 (5).

220. Ros, C., Andreu, T., David, J., Arbiol, J., & Morante, J., Degradation and regeneration mechanisms of NiO protective layers deposited by ALD on photoanodes. Journal of Materials Chemistry A, 2019, 7 (38), 21892-21902.

221. Qiu, Z., Gong, H., Zheng, G., Yuan, S., Zhang, H., Zhu, X., Zhou, H., & Cao, B. Enhanced physical properties of pulsed laser deposited NiO films via annealing and lithium doping for improving perovskite solar cell efficiency. Journal of Materials Chemistry C, 2017, 5 (28), 7084-7094.

222. Lin, C., Chung, W., Zhang, Z., & Hsu, M. P-channel transparent thin-film transistor using physical-vapor-deposited NiO layer. Japanese Journal of Applied Physics, 2017, 57 (1S).

223. Yan, X., Zheng, J., Zheng, L., Lin, G., Lin, H., Chen, G., Du, B., & Zhang, F. Optimization of sputtering NiOx films for perovskite solar cell applications. Materials Research Bulletin, 2018, 103, 150-157.

224. Pant, N., Kulkarni, A., Yanagida, M., Shirai, Y., Miyasaka, T., & Miyano, K. Investigating the Growth of CH3NH3PbI3 Thin Films on RF-Sputtered NiOx for Inverted Planar Perovskite Solar Cells: Effect of CH3NH3+ Halide Additives versus CH3NH3+ Halide Vapor Annealing. Advanced Materials, 2020, 7 (3).

225. Pant, N., Yanagida, M., Shirai, Y., & Miyano, K. Effect of different surface treatments of sputtered NiO X on the photovoltaic parameters of perovskite solar cells: a correlation study. Applied Physics Express, 2020, 13 (2).

226. https://www.lesker.com/newweb/evaporation_sources/alumina-coated-evaporation-sources.cfm, (accessed: February 2020).

227. Wijeyasinghe, N., Regoutz, A., Eisner, F., Du, T., Tsetseris, L., Lin, Y., Faber, H., Pattanasattayavong, P., Li, J., Yan, F., McLachlan, M., Payne, D., Heeney, M., & Anthopoulos, T.Copper(I) Thiocyanate (CuSCN) Hole-Transport Layers Processed from Aqueous Precursor Solutions and Their Application in Thin-Film Transistors and Highly Efficient Organic and Organometal Halide Perovskite Solar Cells. Advanced Functional Materials, 2017, 1701818.

228. https://xpssimplified.com/elements/nickel.php, (accessed: February 2020).

229. Dongyoon, K., Yen-Hung, L., Nam, S., Faber, H., Tetzner, K., Li, R., Zhang, Q., Z., Li, J., Zhang, & Anthopoulos, T. Modulation-Doped In2O3/ZnO Heterojunction Transistors Processed from Solution. Advanced Materials, 2017, 1605837.
230. Zhang, J., Morbidoni, M., Burgess, C., Wu, J., Du, T., Harrabi, K., Payne, D., Durrant, J., & McLachlan, M. Nanoscale Structure–Property Relationships in Low-Temperature Solution-Processed Electron Transport Layers for Organic Photovoltaics. Crystal Growth Design, 2017, 17, 12, 6559-6564.
231. Pattanasattayavong, P., Thomas, S., Adamopoulos, G., McLachlan, M., & Anthopoulos T. p-channel thin-film transistors based on spray-coated Cu2O films. Appl. Phys. Lett., 2013, 102, 163505.
232. Lien, H., Wong, D., Tsao, N., Huang, C., Su, C., Chen, K., & Chen, L. Effect of Copper Oxide Oxidation State on the Polymer-Based Solar Cell Buffer Layers. ACS Appl. Mater. Interfaces, 2014, 6, 22445−22450.
233. Zhang, J., Wang, J., Fu, Y., Zhang, B., & Xie, Z. Sonochemistry-synthesized CuO nanoparticles as an anode interfacial material for efficient and stable polymer solar cells. RSC Adv., 2015, 5, 28786–28793.
234. Yu, Z., Liu, W., Fu, W., Zhang, Z., Yang, W., Wang, S., Li, H., Xu, M., & Chen, H. An aqueous solution-processed CuOX film as an anode buffer layer for efficient and stable organic solar cells. J. Mater. Chem. A, 2016.
235. Xu, Q., Wang, F., Tan, Z., Li, L., Li, S., Hou, X., Sun, G., Tu, X., Hou, J., & Li, Y. High-Performance Polymer Solar Cells with Solution-Processed and Environmentally Friendly CuOx Anode Buffer Layer. ACS Appl. Mater. Interfaces, 2013, 5, 10658−10664.
236. Kim, S. Y., Ahn, C. H., Lee, J. H., Kwon, Y. H., Hwang, S., Lee, J. Y., & Cho, H. K. p‑Channel Oxide Thin Film Transistors Using Solution-Processed Copper Oxide. ACS Appl. Mater. Interfaces, 2013, 5, 2417−2421.
237. Yu, J., Liu, G., Liu, A., Meng, Y., Shin, B., & Shan, F. Solution-processed p-type copper oxide thin-film transistors fabricated by using a one-step vacuum annealing technique. J. Mater. Chem. C, 2015, 3, 9509-9513.
238. Lin, M. Y., Lee, C. Y., Shu-Chia Shiu, S., C., Wang, I. J., Sun, J. Y., Wu, W. H., Lin, Y. H., Huang, J. S., & Lin, C. F. Sol–gel processed CuOx thin film as an anode interlayer for inverted polymer solar cells. Organic Electronics, 2010, 11, 1828–1834.

239. Shen, W., Yanga, C., Bao, X., Suna, L., Wanga, N., Tangb, J., Chena, W., & Yang, R. Simple solution-processed CuOX as anode buffer layer for efficient organic solar cells. Materials Science and Engineering B, 2015, 200, 1–8.

240. Bu, L., Fu, Y., Li, J., & Guo, T. Large-area electrospray-deposited nanocrystalline CuXO hole transport layer for perovskite solar cells. RSC Advanced, 2017, 74.

241. Lee, S. Lee, W. Jang, B. Kim, T. Bae, J. Cho, K. Kim, S. & Jang, J. Sol-Gel Processed p-Type CuO Phototransistor for a Near-Infrared Sensor. IEEE Electron Device Letters, 2017, 39 (1), 47-50.

242. Siddiqui, H., Parra, M., Pandey, P., Qureshi, M., & Haque, F. Utility of copper oxide nanoparticles (CuO-NPs) as efficient electron donor material in bulk-heterojunction solar cells with enhanced power conversion efficiency. Journal of Science: Advanced Materials and Devices, 2020,

243. Mitzi, B. Solution Processing of Inorganic Materials. (John Wiley & Sons, Inc., 2008)

244. Liu, S., Ho, S., Chen, Y. & So, F. Passivation of Metal Oxide Surfaces for High-Performance Organic and Hybrid Optoelectronic Devices. Chem. Mater. 27, 2532–2539 (2015).

245. Lin, Z., Han, D. & Li, S. Study on thermal decomposition of copper(II) acetate monohydrate in air. J. Therm. Anal. Calorim., 2011, 107, 471–475.

246. Jang, J., Chung, S., Kang, H., & Subramaniana, V. P-type CuO and Cu_2O transistors derived from a sol–gel copper (II) acetate monohydrate precursor. Thin Solid Films, 2016. 600, 157-161.

247. Valladares, L., Salinas, D., Dominguez, A., Najarro, D., Khondaker, S., Mitreliasa, T., Barnes, C., Aguiar, J., & Majima, Y. Crystallization and electrical resistivity of Cu2O and CuO obtained by thermal oxidation of Cu thin films on SiO2/Si substrates. Thin Solid Films, 2012, 520 (20), 6368-6374.

248. Richardson, T., Slack, J., & Rubin, M. Electrochromism in copper oxide thin films. Electrochimica Acta, 2001, 46 (13) 2281-2284.

249. Bannock, J, Krishnadasan, S., Nightingale, A., Yau, C., Khaw, K., Burkitt, D., Halls, J., Heeney, M., & Mello, J. Continuous synthesis of device-grade semiconducting polymers in droplet-based microreactors. Advanced Functional Materials, 2013, 23 (17), 2123–2129.

250. Yaacobi-Gross, N., Treat, N., Pattanasattayavong, P., Faber, H., Perumal, A., Stingelin, N., Bradley, D., Stavrinou, P., Heeney, M., & Anthopoulos, T. High-Efficiency Organic

Photovoltaic Cells Based on the Solution-Processable Hole Transporting Interlayer Copper Thiocyanate (CuSCN) as a Replacement for PEDOT:PSS. Advanced Energy Materials, 2014, 5 (3).

251. https://www.organicdivision.org/wp-content/uploads/2016/12/organic solvents.Html, (accessed: February, 2020).
252. https://xpssimplified.com/elements/carbon.php, (accessed: February 2020).
253. https://www.americanelements.com/copper-ii-ethoxide-2850-65-9, (accessed: February 2020).
254. Liu, Z. Duchoň, T., Wang, H., Grinter, D., Waluyo, I., Zhou, J., Liu, Q., Jeong, B., Ethan J. Crumlin, E., Matolín, V., Stacchiola, D., Rodriguez, J., & Senanayake, S. Ambient pressure XPS and IRRAS investigation of ethanol steam reforming on Ni-CeO2(111) catalysts: an in situ study of C-C and O-H bond scission. Phys. Chem. Chem. Phys. 18, 16621–16628 (2016).
255. https://xpssimplified.com/elements/copper.php, (accessed: February 2020).
256. Biesinger, M. Advanced analysis of copper X-ray photoelectron spectra. Surface and Interface Analysis, 2017, 49 (13).
257. Servaites, J., Ratner, M., & Marks, T.,Organic solar cells: A new look at traditional models. The Journal of Energy & Environmental Science, 2011, 11.

8 Appendix

In chapter 3, alumina-coated tungsten boat (EVS9BAOW) was used to evaporate NiO powder. Figure 8.1 shows the employed boat after evaporation process with a residue of NiO liquid (blue). To confirm the colour of NiO liquid, a survey has been done for all materials may be involved in the evaporation and are summarised in Table 8.1.

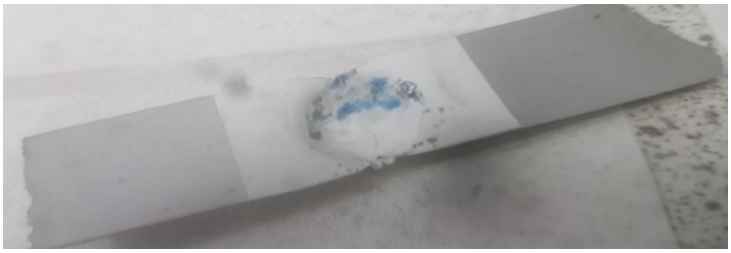

Figure 8.1 Photograph of alumina-coated tungsten boat after evaporation.

Table 8.1 A Summary of materials' properties involved in the thermal evaporation process of NiO powder.

Material	**Density (g/cm^3)**	**Colour**	**Melting point**	**Melting point at 10^{-4} Torr**
Tungsten (W)	19.25	Greyish-white	3,410°C	2,757°C
Tungsten Oxide (WO_3)	7.16	Lemon Yellow	1,473°C	980°C
Aluminium oxide (Al_2O_3)	3.97	White	2,072°C	1,550°C
Nickel (Ni)	8.91	Silvery-white	1,453°C	1,262°C
Nickel oxide (NiO)	6.67	Green	1994°C	1470°C

A complementary XPS data is shown in **Figure 8.2** indicating the survey spectrum of 10 nm NiO_x evaporated film of atomic ratio 80:20. A survey spectrum scans the energy range of interest, in this study 0 – 1300 eV. Atomic ratio Ni:W of 80:20 was selected to investigate in further details.

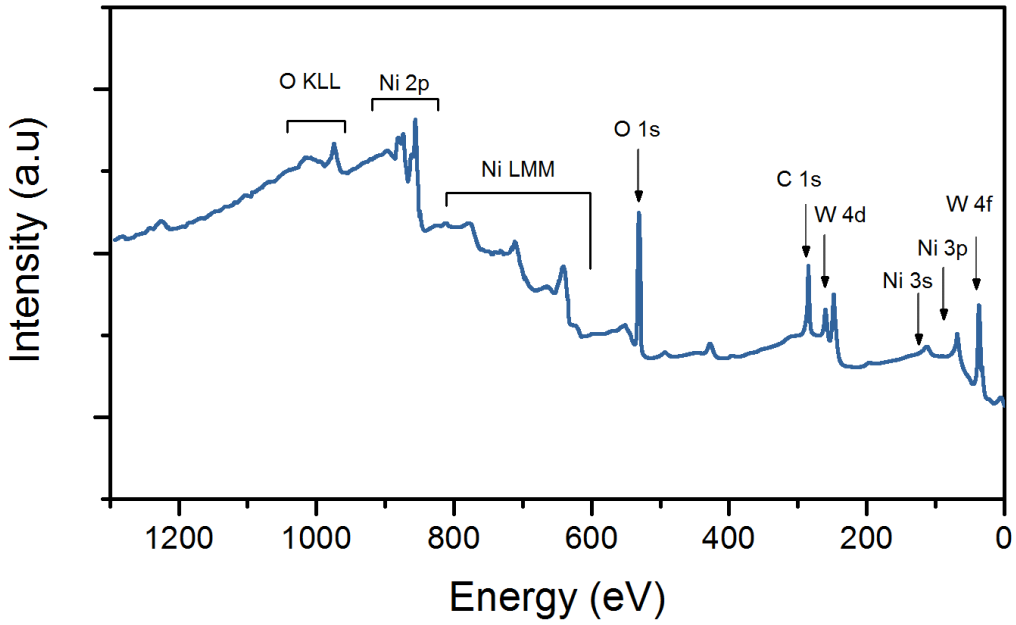

Figure 8.2 Survey spectrum of 10 nm NiO_x film of atomic ratio 80:20, indicating core levels and Auger lines.

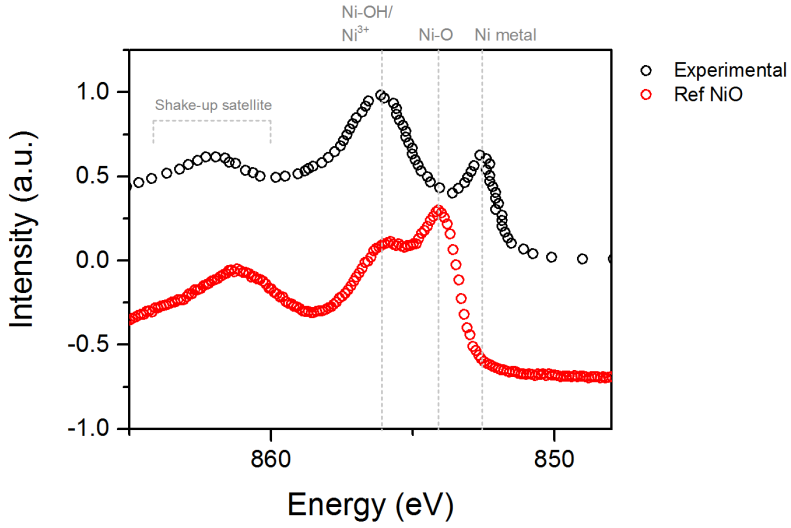

Figure 8.3 Ni $2p_{3/2}$ spectra of 10 nm NiO_x sample of atomic ratio 80:20, a reference spectrum of NiO is included for comparison.

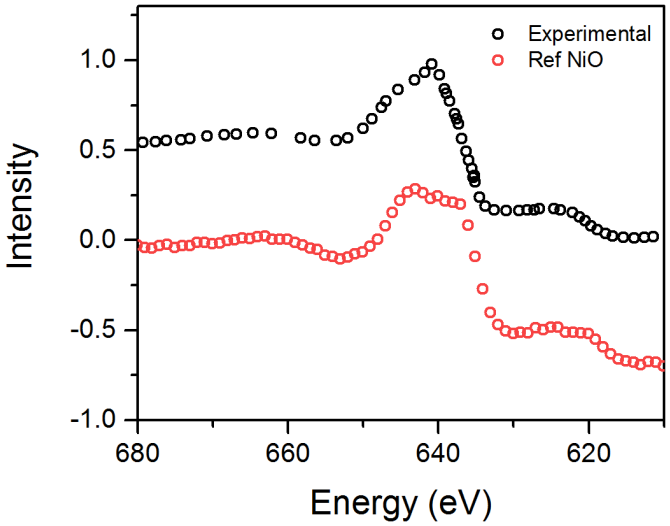

Figure 8.4 Ni LMM Auger spectrum for 10 nm NiO_x film of atomic ratio 80:20, A reference spectrum of NiO is included for comparison.

The potential of thermally evaporated films of 10 nm and 20 at% W:Ni ratio as a universal ETL was investigated by fabrication perovskite solar cell. The devices were fabricated with inverted architecture as shown in **Figure 8.5** (a), and (b) shows the energetics of the materials used in the solar cell fabrication.

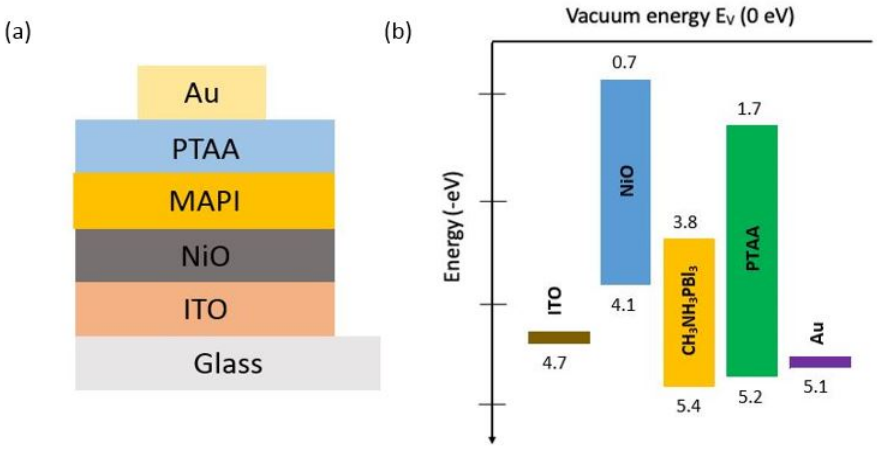

Figure 8.5 (a) Schematic diagram of perovskite solar cell employed. (b) Energetics of the different materials used.

The J–V characteristic curve is shown in **Figure 8.6** .It can be seen that the evaporated film seems to perform well as a universal ETL for different solar cells.

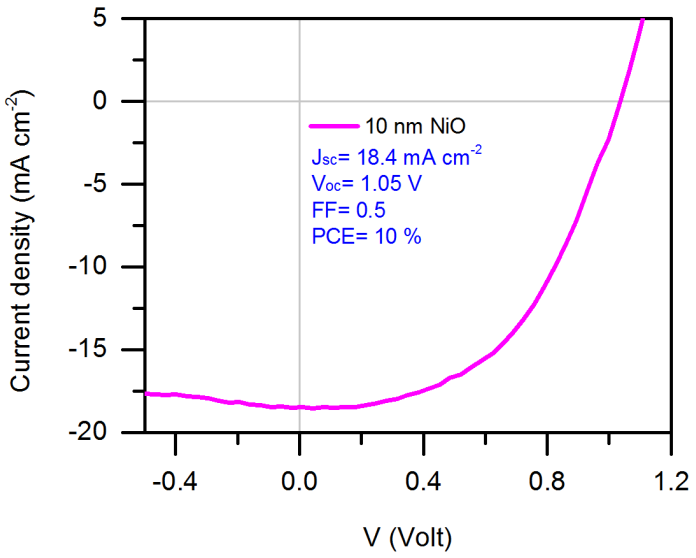

Figure 8.6 J-V curve measured under AM1.5G illumination for perovskite solar cell based on 10 nm evaporated film of NiO_x with 20 at% W:Ni ratio as ETL.

TFT measurements were carried out for 20 nm evaporated film of NiO, deposited on Si/SiO_2 (100nm) with 50 nm gold contacts, at different conditions as shown in **Figure 8.7**. The film seems to be conductive and didn't change this behaviour even after different treatment.

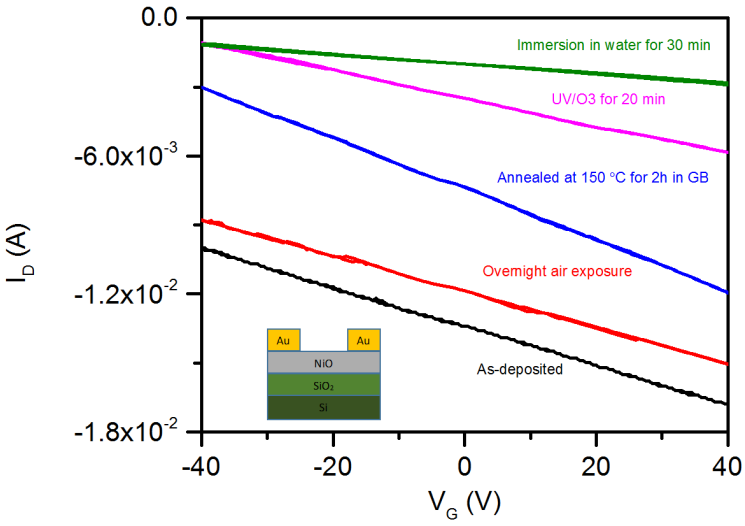

Figure 8.7 transfer characteristics of evaporated NiO_x (20 nm) transistor, at different conditions

In chapter 4, the influence of CuO_x film thickness on its crystallinity was also obtained by changing the precursor concentration, as shown in **Figure 8.8**. The film processed from 0.5M solution concentration shows strong peaks of the mixture of Cu2O, CuO, and Cu.

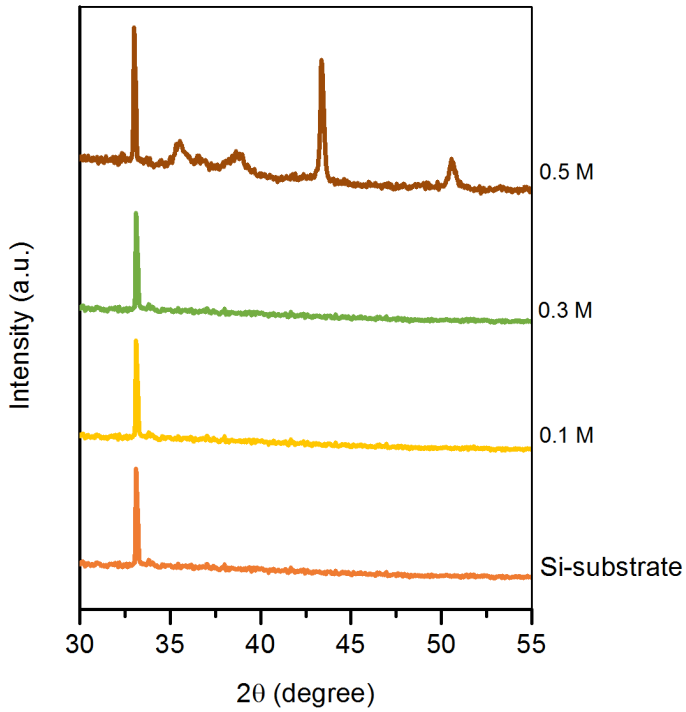

Figure 8.8 XRD patterns for Si-substrate and CuO_x processed from different precursor concentrations, all films annealed at 275°C.

X-ray photoelectron spectroscopy (XPS) measurements were performed to further compare the CuO_x film's composition when processed by two different solvents (2-methoxyethanol and Isopropanol). The characteristic peaks of the elements Cu, O, and C are indicated in the survey scan (**Figure 8.9**).

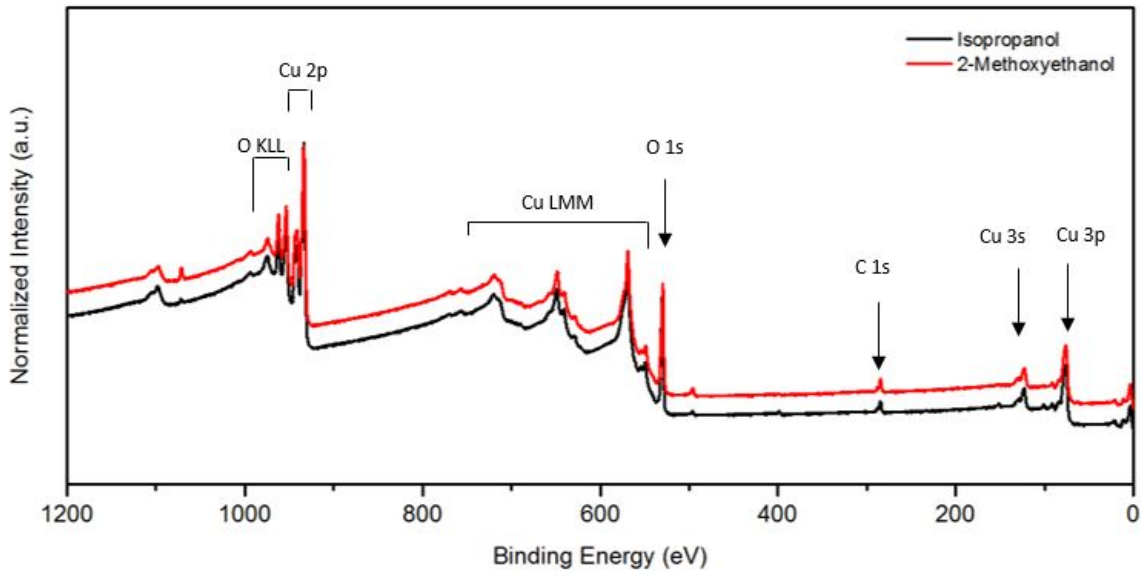

Figure 8.9 Survey spectra of CuOx film processed by different solvents. Core levels and Auger lines of C, O, and Cu are labelled.

From **Figure 8.10**, it was found that the ratio between surface and lattice oxygen in film processed by 2-methoxyrthanol is higher that of film processed by isopropanol. This indicates more copper oxide content produced from 2-methoxyethanol than that of Isopropanol.

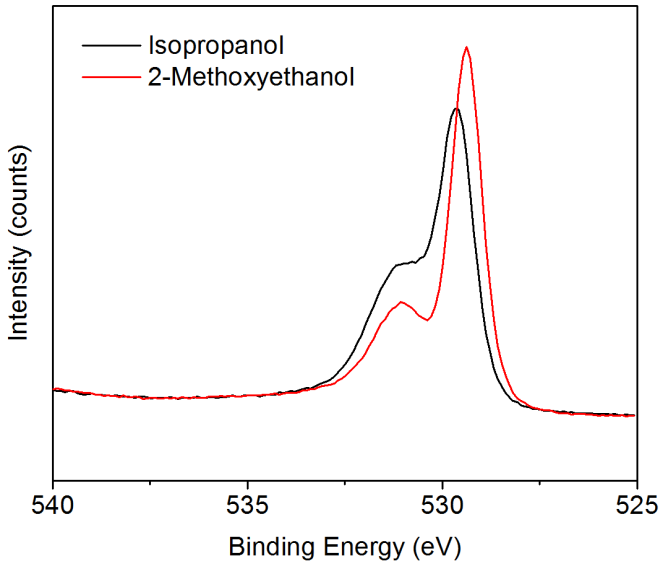

Figure 8.10 O 1s spectra of CuO_x samples processed by different solvents.